

MSC-CA-R-68-1



NATIONAL AERONAUTICS AND SPACE ADMINISTRATION

MSC-CA-R-68-1

RADAR SCATTEROMETER DATA VALIDATION: FINAL REPORT

GPO PRICE \$ _____

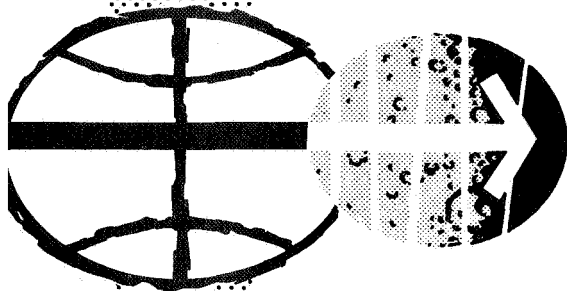
CSFTI PRICE(S) \$ _____

Hard copy (HC) _____

Microfiche (MF) _____

ff 653 July 65

FACILITY FORM 602	N 68-36499	
	(ACCESSION NUMBER)	(THRU)
	159 (PAGES)	1 (CODE)
	TMX 61291 (NASA CR OR TMX OR AD NUMBER)	07 (CATEGORY)



MANNED SPACECRAFT CENTER

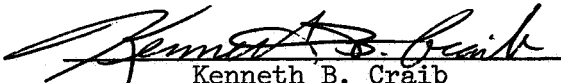
HOUSTON, TEXAS

March 29, 1968

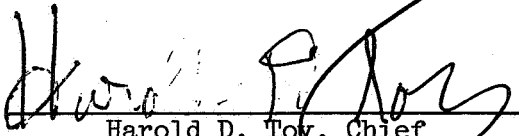
N 6

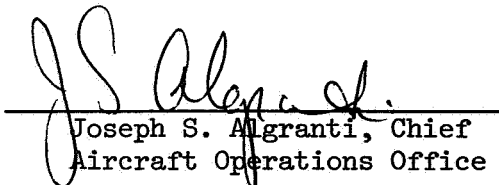
RADAR SCATTEROMETER DATA VALIDATION: FINAL REPORT

PREPARED BY


Kenneth B. Craib
Flight Research Projects Branch

APPROVED BY


Harold D. Toy, Chief
Flight Research Projects Branch


Joseph S. Algranti, Chief
Aircraft Operations Office

NATIONAL AERONAUTICS AND SPACE ADMINISTRATION
MANNED SPACECRAFT CENTER
HOUSTON, TEXAS
March 29, 1968

PRECEDING PAGE BLANK NOT FILMED.

FOREWORD

Data contained in this report were prepared by personnel at the Flight Research Projects Branch of the NASA Manned Spacecraft Center and the Ryan Aeronautical Company to demonstrate the validity of scatterometer information obtained on Earth Resources Survey missions. This report, together with Internal Note No. MSC-CA-R-67-3, completes the radar data review requirements as defined in EX43/M156-66 and Contract NAS 9-6400, Modification 2.

CONTENTS

Section	Page
SUMMARY	1
INTRODUCTION	1
SYMBOLS	3
THEORETICAL DISCUSSION	4
VALIDATION TEST PROCEDURE	11
RESULTS AND DISCUSSION	15
APPENDIX A — REFERENCE DATA FOR VARIOUS TERRAIN TYPES	27
APPENDIX B — SCATTEROMETER DATA SAMPLES	39
REFERENCES	147
BIBLIOGRAPHY	150

TABLES

Table		Page
I	COMPOSITE ROLLOFF FUNCTION FOR OVER-LAND MISSIONS	16
II	COMPOSITE ROLLOFF FUNCTION FOR OVER-WATER MISSIONS (EXCLUDING MISSION 20)	17
III	SCATTEROMETER ANTENNA PATTERN FACTOR	18
IV	ANALYSIS KEY	19

FIGURES

Figure		Page
1	Antenna beam geometry	20
2	The 13.3-GHz radar scatterometer block diagram	21
3	The negative upwind-downwind ratio	22
4	Ratio change as a function of wind velocity (ref. 24)	22
5	The radio-frequency reflectivity analysis functional block diagram	23
6	Flight Research Projects Data Validation Station	
	(a) View one	24
	(b) View two	24
7	Phase-two data validation system (block diagram)	25
8	Time-history recording key	26
A-1	Frequency contrast of 2-inch grass (ref. 5)	28
A-2	Vertical polarization data, K _μ -band (ref. 5)	29
A-3	New Jersey trees (ref. 14)	30

Figure		Page
A-4	Florida mangrove (ref. 14)	31
A-5	The $\sigma_0(\theta)$ curves for various terrains (ref. 14)	
	(a) Heavy vegetation, broken desert, desert sand, and sea	32
	(b) Rocky hills, sand dunes, wooded area, and sea . . .	33
	(c) Grazing land, plowed fields, and wooded swamp . . .	34
	(d) Brushland, rocky hills, and sand dunes	35
A-6	Normal desert terrain (ref. 18)	36
A-7	Desert terrain (AFS WC site)	37
A-8	Lake Michigan, November 14 and 18, 1958 (ref. 25)	38
B-1	Set 1 data samples	
	(a) The $\sigma_0(\theta)$ curve	41
	(b) The PSD curve	42
	(c) Time history, longtime intervals	43
	(d) Time history, short time intervals	44
B-2	Set 2 data samples	
	(a) The $\sigma_0(\theta)$ curve	46
	(b) Flight line	47
	(c) Flight map	48
	(d) The PSD curve	49
	(e) Time history	50
B-3	Set 3 data samples	
	(a) The $\sigma_0(\theta)$ curve	52
	(b) Flight line	53
	(c) Flight map	54
	(d) The PSD curve	55
	(e) Time history	56
B-4	Set 4 data samples	
	(a) The $\sigma_0(\theta)$ curve	58
	(b) Flight line	59

Figure		Page
	(c) Flight map	60
	(d) The PSD curve	61
	(e) Time history	62
B-5	Set 5 data samples	
	(a) The $\sigma_0(\theta)$ curve	64
	(b) Flight line	65
	(c) Flight map	66
	(d) The PSD curve	67
	(e) Time history	68
B-6	Set 6 data samples	
	(a) The $\sigma_0(\theta)$ curve	70
	(b) Flight line	71
	(c) Flight map	72
	(d) The PSD curve	73
	(e) Time history	74
B-7	Set 7 data samples	
	(a) The $\sigma_0(\theta)$ curve	76
	(b) Flight line	77
	(c) Flight map	78
	(d) The PSD curve	79
	(e) Time history	80
B-8	Set 8 data samples	
	(a) The $\sigma_0(\theta)$ curve	82
	(b) Flight line	83
	(c) Flight map	84
	(d) The PSD curve	85
	(e) Time history	86
B-9	Set 9 data samples	
	(a) The $\sigma_0(\theta)$ curve	88
	(b) Flight line	89
	(c) Flight map	90
	(d) The PSD curve	91
	(e) Time history	92

Figure		Page
B-10	Set 10 data samples	
	(a) The $\sigma_0(\theta)$ curve	94
	(b) Flight line	95
	(c) Flight map	96
	(d) The PSD curve	97
	(e) Time history	98
B-11	Set 11 data samples	
	(a) The $\sigma_0(\theta)$ curve	100
	(b) Flight line	101
	(c) Flight map	102
	(d) The PSD curve	103
	(e) Time history	104
B-12	Set 12 data samples	
	(a) The $\sigma_0(\theta)$ curve	106
	(b) Flight line	107
	(c) Flight map	108
	(d) The PSD curve	109
	(e) Time history	110
B-13	Set 13 data samples	
	(a) The $\sigma_0(\theta)$ curve	112
	(b) Flight line	113
	(c) Flight map	114
	(d) The PSD curve	115
	(e) Time history	116
B-14	Set 14 data samples	
	(a) The $\sigma_0(\theta)$ curve	118
	(b) Flight line	119
	(c) Flight map	120
	(d) The PSD curve	121
	(e) Time history	122
B-15	Set 15 data samples	
	(a) The $\sigma_0(\theta)$ curve	124
	(b) Flight line	125

Figure		Page
	(c) Flight map	126
	(d) The PSD curve	127
	(e) Time history	128
B-16	Set 16 data samples	
	(a) The $\sigma_0(\theta)$ curve	130
	(b) Flight line	131
	(c) Flight map	132
	(d) The PSD curve	133
	(e) Time history	134
B-17	Set 17 data samples	
	(a) The $\sigma_0(\theta)$ curve	136
	(b) Flight line	137
	(c) Flight map	138
	(d) The PSD curve	139
	(e) Time history	140
B-18	Set 18 data samples	
	(a) The $\sigma_0(\theta)$ curve	142
	(b) Flight line	143
	(c) Flight map	144
	(d) The PSD curve	145
	(e) Time history	146

RADAR SCATTEROMETER DATA VALIDATION: FINAL REPORT

By Kenneth B. Craib

SUMMARY

After preliminary analysis, 17 magnetic tapes — recorded on missions 21, 23, 32, 35, and 36 — were reviewed to determine the validity of scatterometer data gathered over Earth Resources Program test sites 2, 11, 32, 46, 76, 95, 102, and 104 during April to December of 1966. Sample power-spectral-density curves, time histories, and plots of radar backscattering versus incidence angle were prepared from each data tape. Aerial photographs obtained concurrently with these data and descriptions of the overflown terrains are presented. The techniques and methods used to obtain and to analyze these data are presented and discussed.

INTRODUCTION

The REDOP scatterometer, operated by the Manned Spacecraft Center (MSC) for the Earth Resources Aircraft Program (ERAP), is a continuous-wave (cw) Doppler radar system. The radio-frequency (rf) energy is generated by a 1.5-watt Metcomm MKK-37 klystron oscillator operating at a frequency of 13.3 GHz and radiated by a single-element slotted-array antenna. As shown in figure 1, this antenna generates an extremely broad fan-shaped beam (approximately 120° along the flight path and 3° laterally). The E-vector is oriented in the wide-beam direction to obtain vertical polarization data.

The antenna pattern coverage (radar footprint of the system) may be divided into a series of areas. The size of the areas is determined by the antenna beam width in one direction and by the Doppler resolution along the velocity vector. This resolution can, within limits, be made fine or coarse by selection of spectrum-analyzer filter bandwidths during data reduction. The final reflectivity curves may then present averages, or greatly detailed data, contingent upon the intended application (refs. 1 and 2).

The reflected echo power density is separable as a function of the incidence angle by the Doppler frequency, which is a function of the vehicle velocity and the incidence angle as follows

$$F_d = \frac{2V}{\lambda} \sin \theta \quad (1)$$

where

F_d = Doppler frequency

V = true ground speed

λ = transmitted wavelength

θ = incidence angle, measured from nadir

The reflected signal is received by a second antenna (identical to the first) and is recorded on magnetic tape. Since the required response of the system is 10 Hz to 10 kHz, frequency modulation (FM) recording techniques are employed. With this system, data are received simultaneously from all angles of incidence across the beam. While onboard data processing is feasible, the complete analysis is normally conducted in the laboratory after the flight has been completed.

To aid in this analysis, an audio oscillator, driving a ferrite modulator at a frequency several kHz above maximum ground return, is employed to obtain an absolute signal reference level. This permits calculation of the absolute value of the differential-scattering cross section per unit area σ_0 for any recorded run. An intentional low-frequency rolloff is included in the system amplifier to keep power return within the dynamic range of the tape recorder. This low-frequency rolloff is adjustable and is normally set at 400 Hz for flights over land and at 5 kHz for flights over water, since the power return over water is much greater at lower frequencies (near normal incidence) than at higher frequencies. A block diagram of the 13.3-GHz scatterometer is shown in figure 2.

SYMBOLS

A_i	incidence area
F_d	Doppler frequency
G	antenna gain
$G_0^2 f'(\theta)$	antenna gain and two-way pattern-factor average
h	altitude above terrain
\overline{P}_r	average received power
P_t	transmitted power
p	polarization
$R(D)$	correction factor for composite system rolloff characteristics
R_i	radar range to the i th scatterer
r	surface roughness
W_s	ferrite-modulator signal-channel power output and spectrum-analyzer filter bandwidth coefficient
V	true ground speed
γ	parameter
ΔA	area contributing to a particular return signal
ΔF	Doppler resolution, determined by adjustment of spectrum-analyzer filter bandwidth during data reduction
ϵ	permittivity
η	conductivity
θ	incidence angle

4

λ	wavelength
σ	radar cross section proportional to the area of the terrain contributing to the return
σ_0	differential-scattering cross section per unit area
$\sigma_0(\theta)$	radar backscattering cross section per unit area
σ_i	effective cross section of the i th scatterer
τ	standard deviation in elevation of points on a surface
ϕ	lateral beam-width angle
ψ	depression angle

THEORETICAL DISCUSSION

A radar scatterometer system is designed to measure the radar reflectivity or the differential-scattering cross section per unit area of various surfaces as a function of incidence angle. The differential-scattering cross section is a dimensionless real number, the magnitude of which is a function of the terrain parameters, describing the ability of a particular target or target area to scatter energy in a given direction. This implies that the return energy is received at such a distance that the scattered field can be regarded as an outgoing spherical wave (ref. 3).

The quantity σ_0 varies with incidence angle, wavelength of observation, and polarization for different materials. The relationship between these variables "forms the basis for scatterometry as a tool for the earth sciences" (ref. 4).

The fundamental parameters governing changes in radar return from terrain are as follows (refs. 4, 5, and 6).

1. Wavelength
2. Polarization
3. Incidence angle

4. Surface roughness
5. Electrical conductivity of the terrain
6. Electrical permittivity of the terrain

The first three of these parameters are selectable at the discretion of the investigator. The remaining three parameters may vary with the type and percentage of vegetation cover, water content, and other seasonal effects. Base-line data concerning these quantities are usually acquired by field measurements and are referred to as ground-truth information. The differential-scattering cross section per unit area of a particular target σ_0 may be expressed as

$$\sigma_0 = f(\lambda, p, \theta, r, \eta, \epsilon) \quad (2)$$

where

λ = wavelength
 p = polarization
 θ = incidence angle
 r = surface roughness
 η = conductivity
 ϵ = permittivity

The product of the quantity σ_0 and the area ΔA which contributes to a particular return signal may be expressed as the sum of the individual scattering coefficients, σ_i (ref. 4). This number describes the ability of the i th target element to reradiate toward the receiver as follows:

$$\sum_i \sigma_i = \sigma_0(\Delta A) \quad (3)$$

If the relative phase difference between signals reflected from several small scatters in a particular area is discounted, then

$$\bar{P}_r = \frac{G^2 \lambda^2 P_t}{(4\pi)^3} \sum_i \frac{\sigma_i}{R_i^4} \quad (4)$$

which, when combined with equation (3), yields

$$\sigma_0 = \frac{(4\pi)^3 R_i^4}{G^2 \lambda^2 \Delta A} \left(\frac{\bar{P}_r}{P_t} \right) \quad (5)$$

where

σ_0 = differential-scattering cross section
per unit area

σ_i = effective cross section of the i th
scatterer

R_i = radar range to the i th scatterer

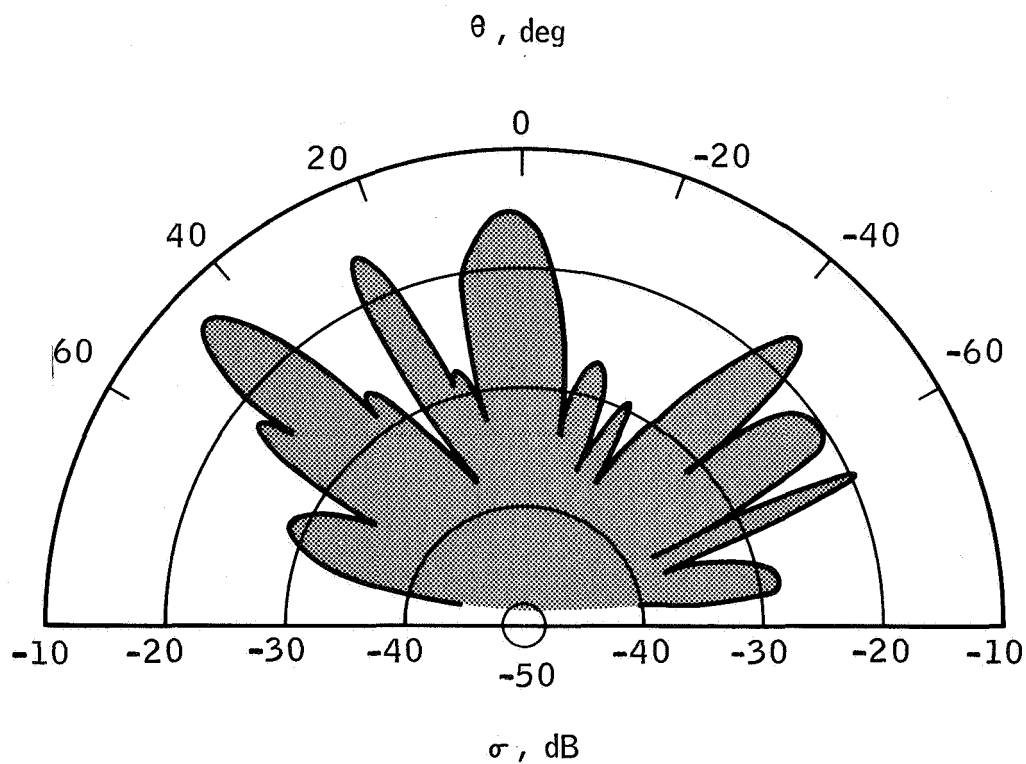
G = antenna gain in the direction of the scatterers

λ = wavelength

\bar{P}_r = average received power

P_t = transmitted power

A typical reradiation pattern for a two-dimensional rough scatterer might appear as shown in the following sketch.



The echo power density of such a scattered field varies with the looking angle. The angular position of the observed maximum and minimum echo power densities is then a function of the surface geometry of the scatterer. The degree to which this surface appears rough or smooth is a function of the wavelength of observation.

If the roughness criterion expressed by Lord Rayleigh is employed as a reference, then a surface is considered rough when

$$\frac{h \cos \theta}{\lambda} < \frac{1}{8} \quad (6)$$

where h is the height of the roughness element, λ is the wavelength, and θ is the incidence angle. A study of σ_0 versus θ curves obtained by using the Davies-Moore-Hayre terrain reflectivity model has also indicated that the transition range from quasi-smooth to rough surface is

$$\frac{\tau}{\lambda} \approx 0.08 - 0.125 \quad (7)$$

where τ represents the standard deviation in the elevation of points on a surface above and below the mean surface (ref. 7).

In most cases, when the rms roughness of a surface is such that $\tau > \lambda/10$, the incident wave scatters. Surfaces may be cataloged by this roughness function along a continuum from surfaces which produce a single backscatter lobe at vertical incidence (specular reflectors) to surfaces which scatter energy equally in all directions (isotropic scatterers). For such a surface, $\tau \gg \lambda$.

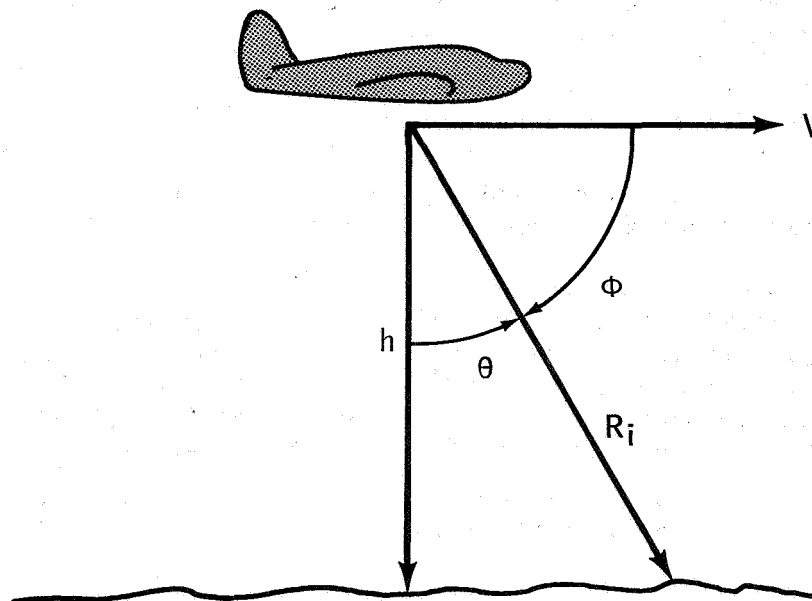
The majority of theories in existence which describe the radar return from complex surfaces require that certain assumptions be made (refs. 7, 8, 9, 10, and 11). However, as pointed out in reference 6, considerable controversy exists concerning which set of assumptions yields an expression for equation (2), which is uniformly valid for natural terrain. However, the lack of a well-defined statistical model, which describes radar terrain return, does not invalidate an empirical determination based on a catalog of experimentally derived signatures for various surface types and conditions.

At the present time, a substantial number of terrain-clutter curves exist for different polarizations, frequencies, angles, et cetera. These curves have been shown to be repeatable within ± 1 dB (refs. 5, 12, 13, and 14). Thus, new data obtained over any area of interest may be compared with previously established values for which an adequate amount of ground-truth information exists. Since the magnitude of the return over land increases proportionally with increases in transmitter frequency, radar data acquired by systems operating in different frequency bands

may be qualitatively and quantitatively compared (refs. 14 and 15). One method to demonstrate the validity of data obtained with a specific scatterometer system would be to compare the output data with such a catalog of reflectivity curves. This approach is used in this report to evaluate the 13.3-GHz data obtained for the Earth Resources Survey Program. Samples of scatterometer data generated by similar systems over various terrain types are included for comparison and to further illustrate the validity of the 13.3-GHz fan-beam data (appendix A).

Radar backscattering information is a relatively new tool in the field of earth science; and, as with any new concept, a complete standardization of terms and definitions has not yet been established. Therefore, a certain amount of care must be exercised when comparing scatterometry data generated by different experimenters.

The angle between the radar beam, or a portion of the beam, and the illuminated terrain is variously referred to as the depression angle, aspect angle, incidence angle, looking angle, et cetera. In this report, all data have been plotted with respect to the angle of incidence θ shown in the following sketch.



In the sketch, R_i is the range to the i th scatterer or area and ψ is the depression angle. Also, in this report, terrain has been characterized by the parameter σ_0 , as defined in equation (5). In some of the reference literature, a parameter γ is introduced and is defined by the equation

$$\sigma = \gamma A_i \quad (8)$$

where A_i is the incidence area and σ is the radar cross section proportional to the area of the terrain contributing to the return. The relationship between γ and σ_0 (ref. 5) is shown as

$$\sigma_0 = \gamma \sin \psi = \gamma \cos \theta \quad (9)$$

All reference data presented in this report for correlation purposes have been replotted as a function of σ_0 and θ by using these relationships.

One desired result of a scatterometer data gathering program, such as that incorporated in the ERAP, is the generation of a family of radar backscatter curves ($\sigma_0(\theta)$) which are characteristic of various terrain surfaces. The information contained in any particular curve will vary with specific conditions and must be carefully correlated with ground-truth data. However, a brief examination of the relative $\sigma_0(\theta)$ values, the slope of the curve, and a general knowledge of the terrain type will usually reveal any significant departure from the data norm.

Scattering theory and experimentally derived data allow several general statements to be made concerning the characteristic curve. For relatively smooth surfaces ($\tau < \lambda/10$), the return will be a function of all the pertinent parameters previously mentioned. For very rough surfaces ($\tau \gg \lambda$), the magnitude of the scattering coefficient becomes independent of the incidence angle and polarization, and the $\sigma_0(\theta)$ curve approaches a straight line. In general, for all homogeneous surfaces, the magnitude of σ_0 varies inversely with θ (refs. 5, 6, and 7).

For smooth surfaces, such as a Beaufort 1 sea, σ_0 decreases rapidly (having its largest value near vertical incidence) as θ increases. Geometrically similar surfaces which possess smaller scattering coefficient values, such as smooth deserts, will develop a σ_0 curve with a similar slope but with a lower absolute magnitude (refs. 4, 5, 7, and 16). For rough surfaces, such as densely forested areas, the σ_0 value near vertical incidence will be significantly less because of the decrease in the specular reflection component, and the average slope of the curve will be similarly decreased (refs. 4, 7, 17, and 18). Also, since the dielectric constant of vegetation and soils varies with the percentage of water content, σ_0 values will tend to be lower for the same terrain at all incidence angles during the spring when the water content is usually highest (ref. 5).

Plots of σ_0 values for ocean surfaces exhibit the previously discussed properties. The smoother sea states yield a steeper slope (near vertical) and a lower average value for σ_0 . However, as several prominent researchers have suggested, the surface ripple or small-scale structure created by the local wind field may greatly alter the scattering properties of the surfaces, and may well be more of a controlling factor in radar return than the actual sea state (refs. 19, 20, 21, 22, and 23). In this event, wind direction relative to radar incidence angle will play an important role.

Experiments have shown that, for $\theta > 50^\circ$, sea return is greater when looking upwind than when looking downwind at the same angle. For the range of incidence angles 10° to 40° , this ratio becomes negative. Furthermore, the magnitude of this effect varies inversely with the wavelength of observation (refs. 21, 24, and 25). Figure 3 illustrates this effect for wavelengths of $\lambda = 1$ cm, $\lambda = 3$ cm, and $\lambda = 5$ cm. Data obtained with the 13.3-GHz scatterometer ($\lambda = 2.26$ cm) will then reflect changes in wind direction as well as small-scale surface roughness. As seen in figure 4, the minimum value of the negative upwind-downwind ratio shifts toward larger values of θ as the wind velocity increases. The general shape of the ratio curve remains unchanged.

VALIDATION TEST PROCEDURE

A typical rf reflectivity analysis program will follow the functional plan shown in figure 5. The effort reported in this paper was conducted in a similar series of steps. The Flight Research Projects Branch Data Validation Station in phase-two configuration is shown in

figures 6 and 7, and a block diagram of the equipment used is presented in figure 8. Dual instrumentation was used whenever practical to insure data accuracy. Equipment checkout and calibration support at the unit level were provided by the Standards and Calibration Section of the Instrumentation and Electronic Systems Division at MSC. In addition, alinement, calibration, and signal-level checks were performed daily to maintain quality and continuity and to provide a continuous record of block systems performance.

In the phase-two validation effort, sample power-spectral-density (PSD) curves were prepared from each of the several data tapes under consideration. The existence, level, and frequency stability of the calibration reference signal were reverified from these curves, and the presence and extent of interference noise were determined. The shape of the PSD plot provided additional information concerning data validity. Time-history samples were then recorded for each of the several frequencies of interest over a selected area, and from these data, the characteristic reflectivity curves were plotted.

The Operational Applications Office of the MSC Photographic Technology Laboratory provided copies of aerial photographs taken over the various areas during radar data acquisition. These photographs were examined to further determine the validity of the $\sigma_0(\theta)$ curves.

Although this office was unable to obtain complete information concerning ground-truth conditions existing during the several missions, descriptions of the general test-site terrain were provided by the Test and Operations Office, Science and Applications Directorate at MSC. Additional information concerning specific areas was obtained with the assistance of the Remote Sensing Evaluation and Coordination Staff (RESECS), U.S. Geological Survey, Washington, D.C.

As a final check, the $\sigma_0(\theta)$ data generated during this effort were compared with previous values obtained by several experimenters for a variety of terrains and with predicted values from scattering theory. These reference curves (together with the photographic data, flight maps, PSD curves, time histories, and $\sigma_0(\theta)$ plots) are presented in appendix B.

The PSD data shown in this report represent plots of the REDOP scatterometer analog-decibel output versus frequency from 0.1 to 22 kHz. These data were prepared by sweeping a Quan-Tech Model 303 wave analyzer through the spectral range with a selected 100-Hz filter bandwidth. Time-history frequency signal-level samples (30 sec) were recorded for each of the corresponding incidence angles. Specific Doppler frequencies were determined from equation (1). For a 13.3-GHz transmitter frequency, the constant $2/\lambda$ equals 45.646 hertz per knot (ground speed). In the

analysis, incidence angles of 2.5° , 5° , 15° , 25° , 35° , 40° , 45° , 55° , and 60° were examined. As in previous efforts at MSC, areas of homogeneous terrain were selected, and sign-sense detection was not employed. The resulting data points are, therefore, an average of the fore and aft beam angular return.

For each area of interest, one sample of each of the nine discrete frequencies was prepared. A sample of the calibration frequency and adjacent threshold levels was included on the same plot to provide a reference level and an indication of system-base band noise.

To simplify the plotting process, the $\sigma_0(\theta)$ equation format presently used in the ERAP digital-computer scatterometer data-analysis program was employed as follows

$$\sigma_0(\theta) = \frac{2(4\pi)^3 h^2 V W_s R(D)}{P_t \lambda^3 G_0^2 f'(\theta)} \quad (10)$$

where

$\sigma_0(\theta)$ = radar backscattering cross section
per unit area

h = altitude above terrain

V = true ground speed

P_t = transmitted power

λ = wavelength

W_s = ferrite-modulator signal-channel power
output and spectrum-analyzer filter
bandwidth coefficient

$R(D)$ = correction factor for composite system
rolloff characteristics

$G_0^2 f'(\theta)$ = antenna gain and two-way pattern-factor
average

By converting to dB form, $\log_{10} \frac{2(4\pi)^3}{P_t \lambda^3} = 69.5 \text{ dB}$

therefore

$$\sigma_0(\theta) = 69.5 \text{ dB} + 20 \log_{10} h + 10 \log_{10} V + W_s + R(D) - G_0^2 f'(\theta) \quad (11)$$

Values for h and V are determined from the aircraft log, the photo panel film, and the mission tapes. The second and third terms of equation (11) are then computed. After the Doppler frequency F_d is determined from equation (1), the composite rolloff function $R(D)$ may be found in tables I and II. The antenna pattern factor $G_0^2 f'(\theta)$ is determined from table III for the angle of interest.

When indepth data reduction is performed, it is desirable to view the same size ground resolution cell at each of the selected angles. This requires that separate or adjustable band-pass filters be used. Since the current effort was to establish only the relative validity of specific scatterometer data, a fixed 100-Hz (-3 dB at ± 50 Hz) filter was used for all values of θ . The spectrum-analyzer filter bandwidth coefficient W_s then becomes -20 dB, which yields a constant power reference value of -147.7 dB. The time periods selected for analysis were chosen for minimum variation in ground speed and altitude; and, therefore, average values of these parameters were used. Similarly, correction factors for aircraft attitude and attitude rate were not required.

Data bank magnetic tape accession numbers, mission and flight numbers, $\sigma_0(\theta)$ sample times, and other reference information defining the data reviewed are presented in table IV. Also, computed $\sigma_0(\theta)$ curves, PSD plots, aerial correlation photographs, and flight maps are presented as a part of this document, together with several previously published characteristic curves, for reference purposes. To facilitate interpretation of the radar return as a function of the incidence angle, time-history signal samples for each of the angles of interest at a particular point in time are presented. These samples may be related to the specific angle by means of the recording key shown in figure 9. Vertical displacement on the time-history charts is a function of relative signal level. Horizontal displacement is arbitrary and was selected to provide optimum signal separation.

RESULTS AND DISCUSSION

Although the data validation effort was limited, by request, to five specific missions, it is felt that the basic objectives of the program have been realized. Reference aircraft and ground parameters required for scattered return analysis have been shown to be available, the presence of suitable calibration signals and correlation photography has been verified, and the reducibility of the data collected during these missions has been demonstrated. The validity of the data has been shown by comparison with data published by other investigators and by internal consistency. The $\sigma_0(\theta)$ curves generated for the Yellowstone National Park area on mission 32 are almost identical. Differences, where they exist, may easily be correlated with small variations in terrain along the ground track. Curves developed for the Weslaco, Texas, and Garden City, Kansas, areas illuminate differences in crop type and growth stage while maintaining a characteristic shape.

Data shown for the Asheville Basin overflights confirm previous statements concerning altitude limitations with the 13.3-GHz scatterometer in its present configuration. An altitude of 10 000 feet should be considered maximum for reliable data with this system; an altitude of 5000 feet appears to be nominal. The data presented for mission 21, flight 5, at 1415 P.s.t. over Pisgah Crater illustrate data perturbations caused by electromagnetic interference. In the sample shown, the presence of the camera pulses (28 V dc intervalometer pulses to the cartographic cameras) makes interpretation somewhat difficult. However, the requirements of the user will determine the degree to which this interference affects data validity. If data points can be selected along the flight path, then analysis may be performed in the time-variant windows between camera firings.

TABLE I.- COMPOSITE ROLLOFF FUNCTION FOR OVER-LAND MISSIONS

Doppler frequency, Hz	Rolloff R(D), dB
10	30.8
20	24.3
30	21.3
40	18.3
50	16.8
60	15.3
70	13.8
80	13.3
90	12.9
100	11.3
200	5.8
300	2.8
400	1.8
500	.8
600	.3
700	-.1
800	-.4
900	-.5
1 000	-.8
2 000	-1.0
3 000	-1.0
4 000	-.9
5 000	-.9
6 000	-.7
7 000	-.4
8 000	-.3
9 000	-.1
10 000	.0

TABLE II.- COMPOSITE ROLLOFF FUNCTION FOR OVER-WATER MISSIONS

(EXCLUDING MISSION 20)

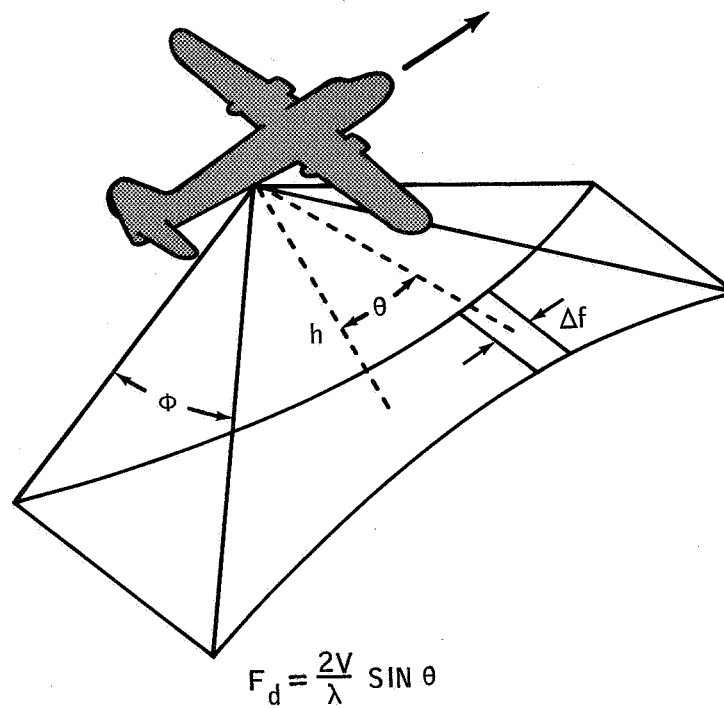
Doppler frequency, Hz	Rolloff R(D), dB
100	22.9
150	21.1
200	20.0
250	18.9
300	17.6
400	15.8
500	14.3
600	13.1
700	12.0
850	10.3
1 000	9.0
1 250	7.5
1 500	6.3
2 000	4.3
2 500	3.2
3 000	2.1
4 000	1.0
5 000	.3
7 000	-.1
10 000	.0

TABLE III.- SCATTEROMETER ANTENNA PATTERN FACTOR

θ , deg	Fore, dB		Aft, dB	
	Beam width, dB rad	$G_0^2 f'(\theta)$	Beam width, dB rad	$G_0^2 f'(\theta)$
2.5	-13.6	24.8	-13.8	24.0
5	-13.7	24.8	-13.9	23.2
15	-13.8	24.0	-13.8	25.6
25	-13.7	25.3	-13.7	25.4
35	-13.7	23.6	-13.6	23.1
40	-13.8	21.5	-13.6	23.7
45	-13.7	21.9	-13.7	23.4
55	-13.6	19.8	-13.7	17.8
60	-13.7	15.6	-13.6	14.7

TABLE IV.- ANALYSIS KEY

Data bank accession number	Mission/flight	Line/run	Site	Date	σ_0 sample time					
					Start			Stop		
					Hours	Minutes	Seconds	Hours	Minutes	Seconds
75-0005	21/5	1/2	2	4/5/66	14	15	34	14	15	38
75-0006	21/5	1/3	2	4/5/66	15	03	38	15	04	08
75-0017	23/1	1/2	46	5/7/66	11	03	37	11	04	07
75-0018	23/1	1/2	46	5/7/66	11	48	15	11	48	45
75-0019	23/1	1/3	46	5/7/66	12	39	08	12	39	38
75-0020	23/1	1/4	46	5/7/66	13	09	45	13	10	15
75-0079	32/1	4/1	76	9/19/66	14	30	08	14	30	23
75-0080	32/1	3/1	76	9/19/66	14	52	55	14	53	10
75-0081	32/2	5/1	11	9/20/66	11	05	20	11	05	50
75-0082	32/2	7/1	11	9/20/66	11	51	20	11	51	30
75-0083	32/2	7/1	11	9/20/66	12	03	35	12	04	00
75-0172	35/1	1/1	32	12/5/66	13	04	30	13	04	40
75-0173	35/1	12/1	32	12/5/66	12	52	35	12	52	55
75-0175	36/1	1/1	102	12/6/66	13	08	25	13	08	55
75-0178	36/2	3/3	95	12/7/66	9	22	25	9	22	35
75-0182	36/4	1/1	95	12/8/66	8	48	00	8	48	05
75-0183	36/4	4/2	95	12/8/66	9	11	30	9	11	40
Functional check flight (FCF)	--	--	Mata- gorda Bay	2/3/67	11	50	30	11	50	40



Where: F_d = Doppler frequency
 V = True ground speed
 λ = Wavelength
 θ = Incidence angle,
 measured from nadir

ϕ = Lateral beam width angle
 h = Altitude above terrain
 Δf = Doppler resolution,
 determined by adjustment
 of spectrum-analyzer filter
 bandwidth during data reduction

Figure 1.- Antenna beam geometry.

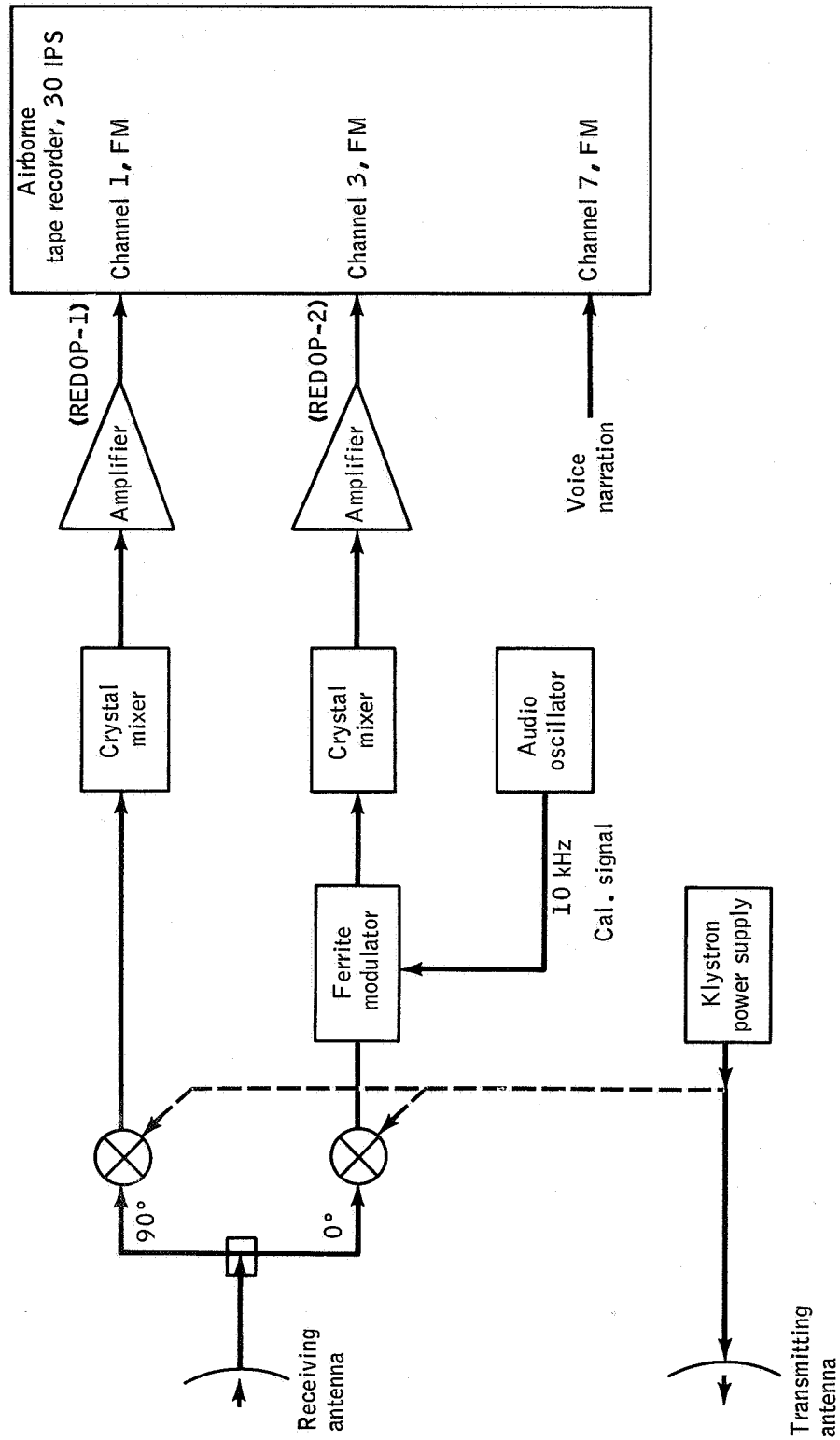


Figure 2.- The 13.3-GHz radar scatterometer block diagram.

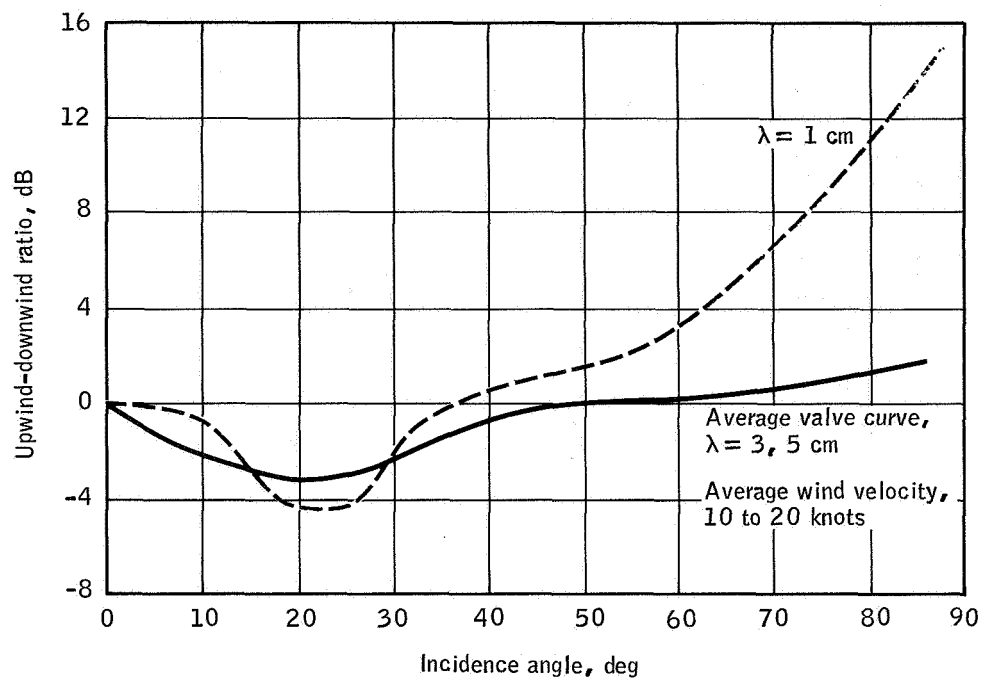


Figure 3.- The negative upwind-downwind ratio.

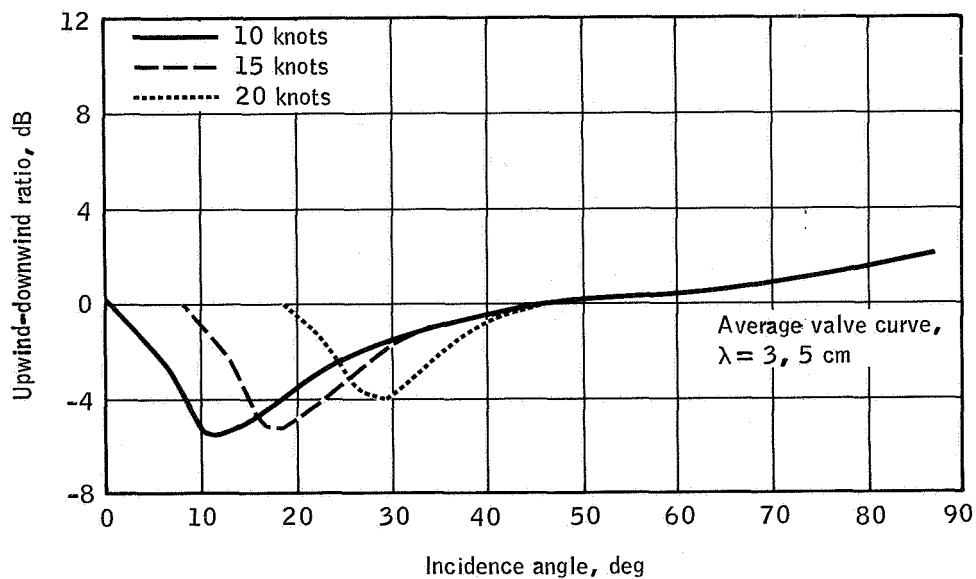


Figure 4.- Ratio change as a function of wind velocity (ref. 24).

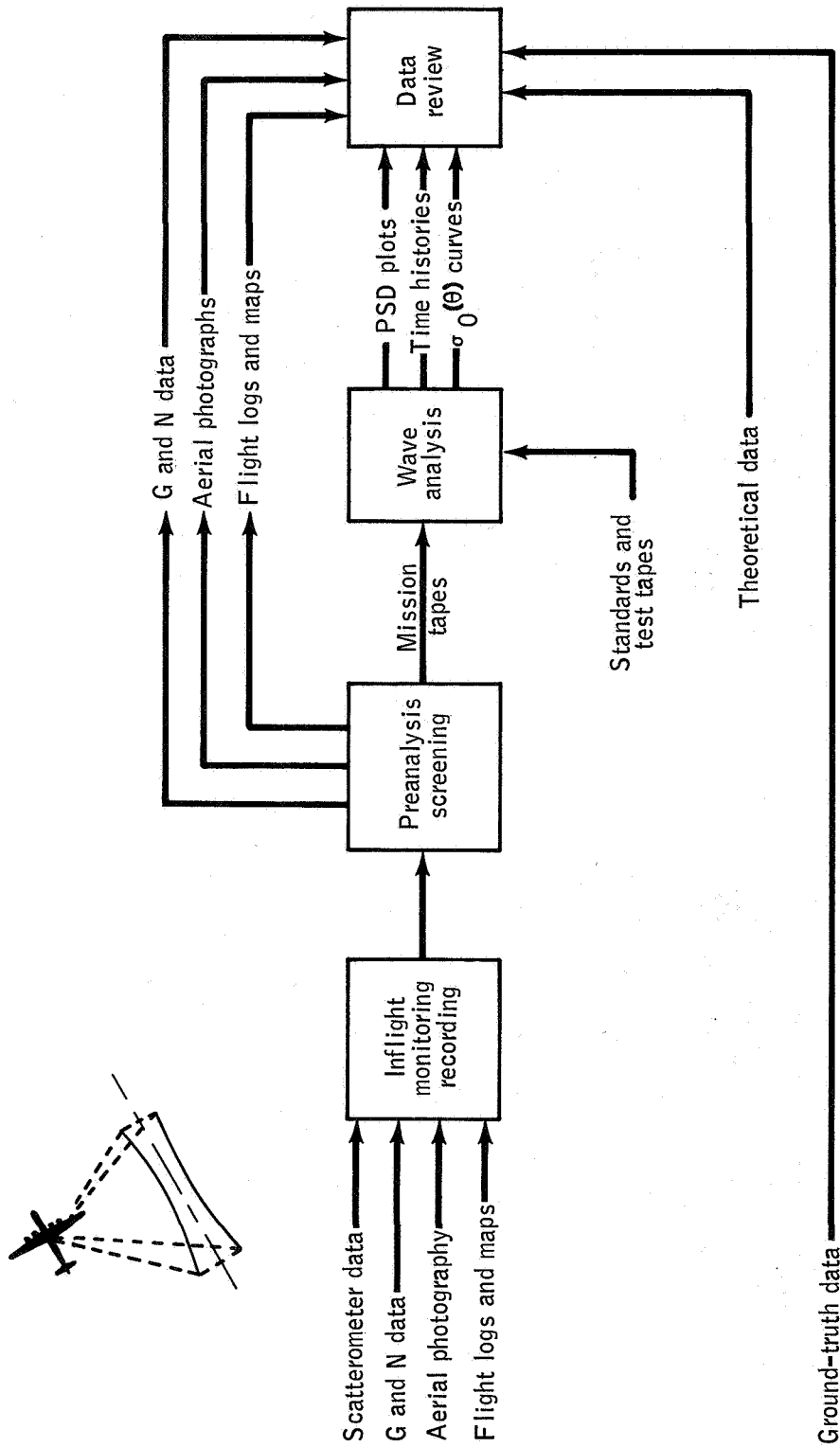
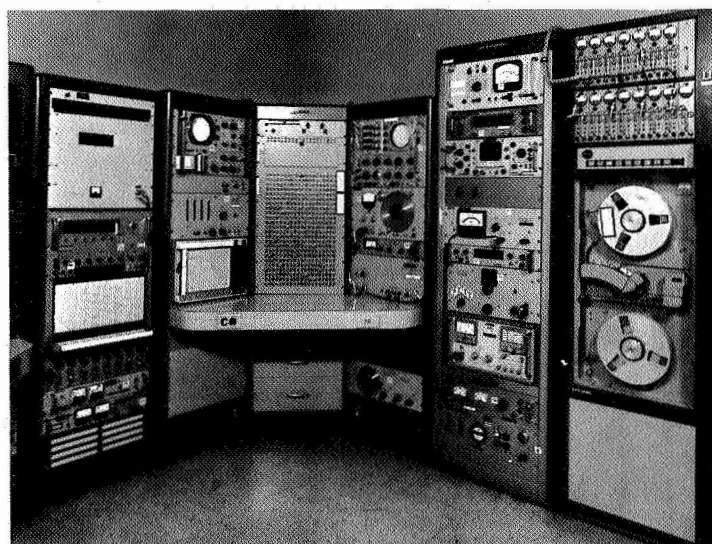


Figure 5.- The radio-frequency reflectivity analysis functional block diagram.



(a) View one.



(b) View two.

Figure 6.- Flight Research Projects Data Validation Station.

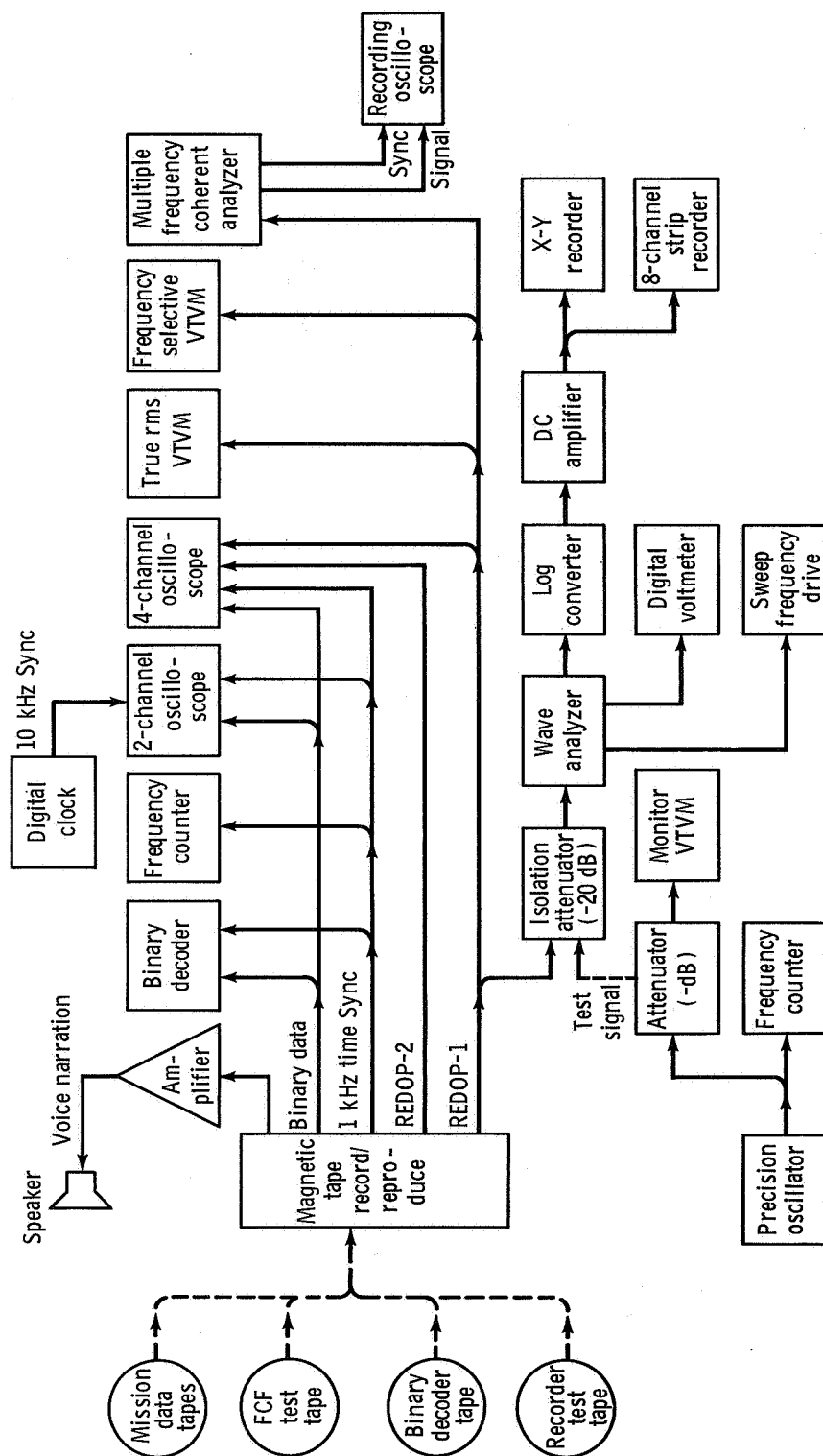


Figure 7.- Phase-two data validation system (block diagram).

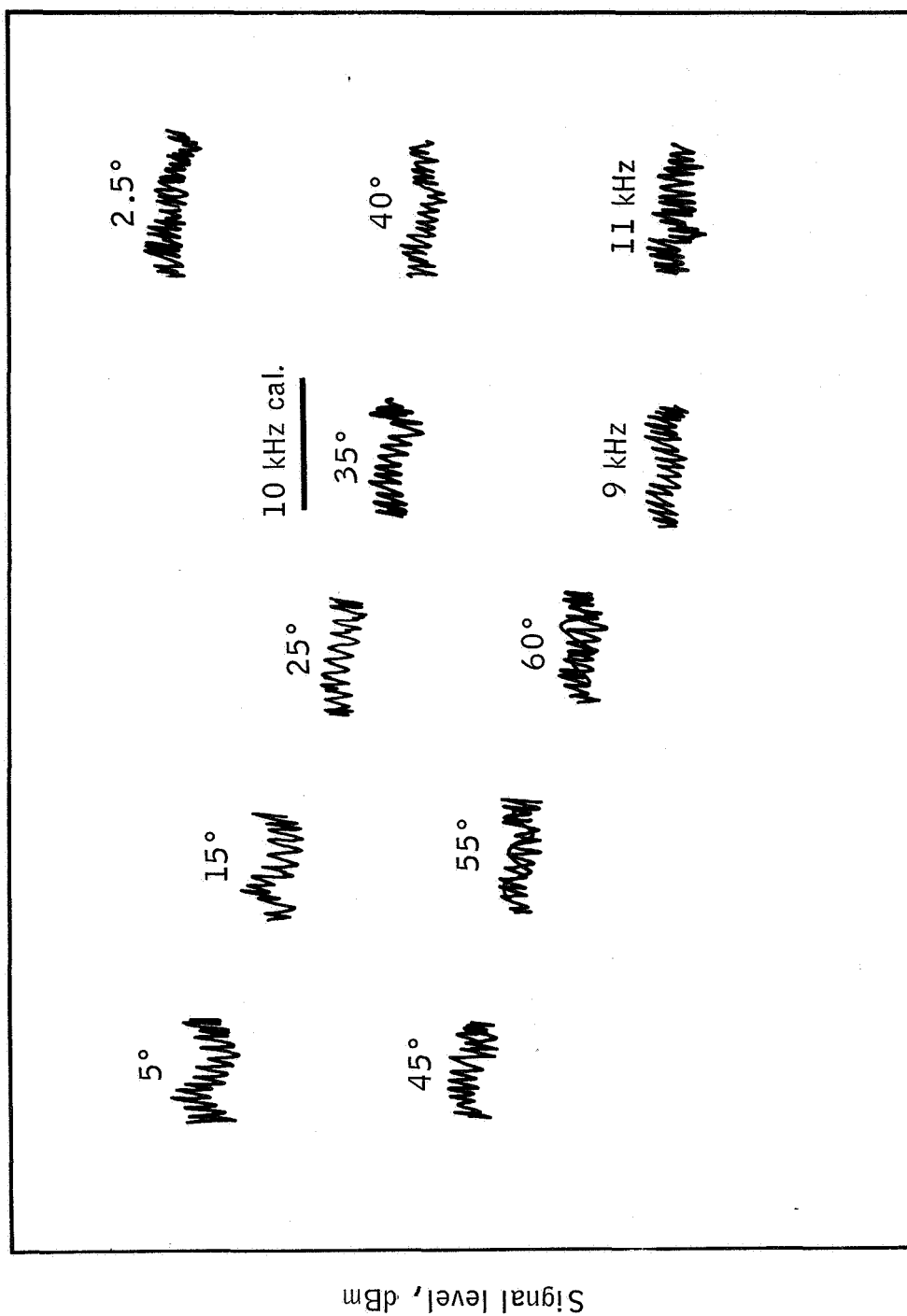


Figure 8.- Time-history recording key.

APPENDIX A

REFERENCE DATA FOR VARIOUS TERRAIN TYPES

This appendix contains samples of scatterometer data gathered over various terrain types which are included for comparison and to further illustrate the validity of the 13.3-GHz fan-beam data.

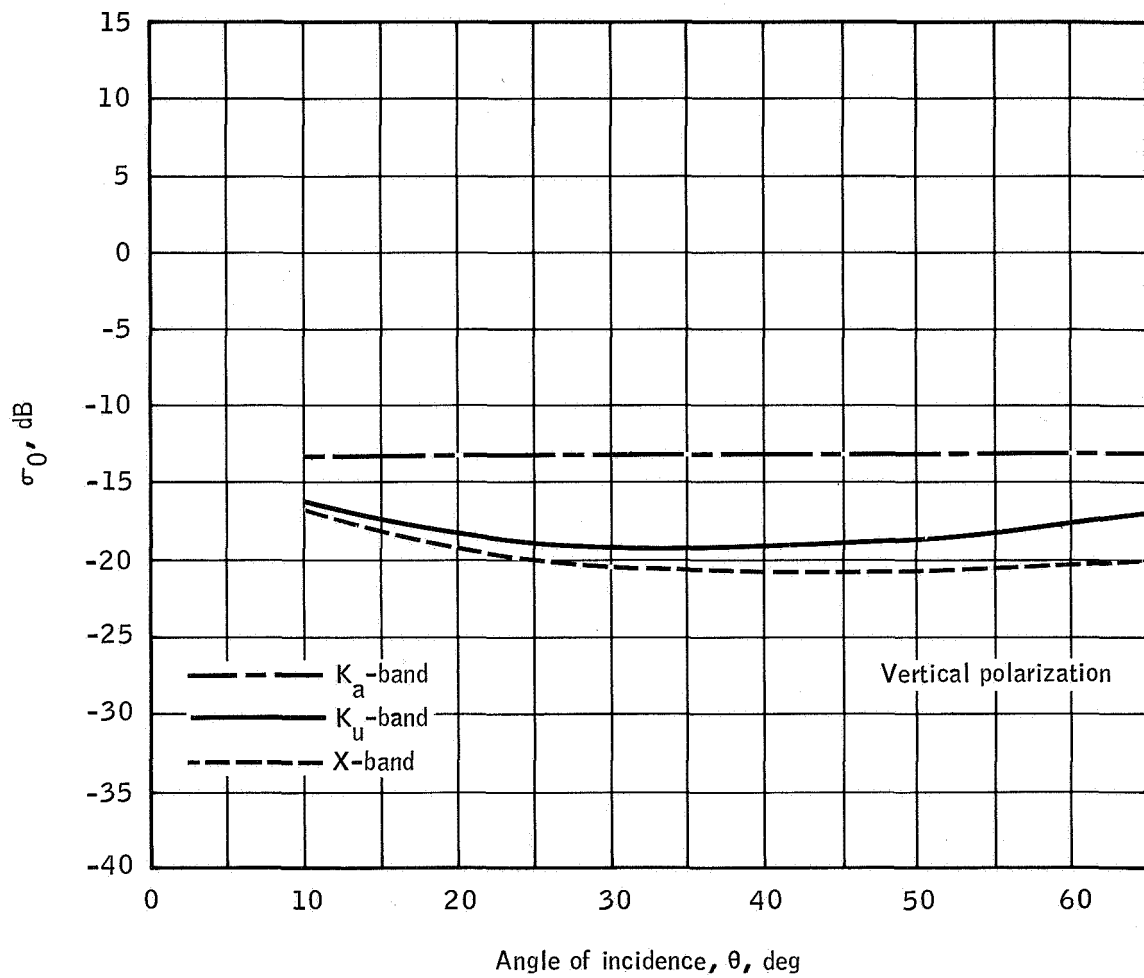


Figure A-1.- Frequency contrast of 2-inch grass (ref. 5).

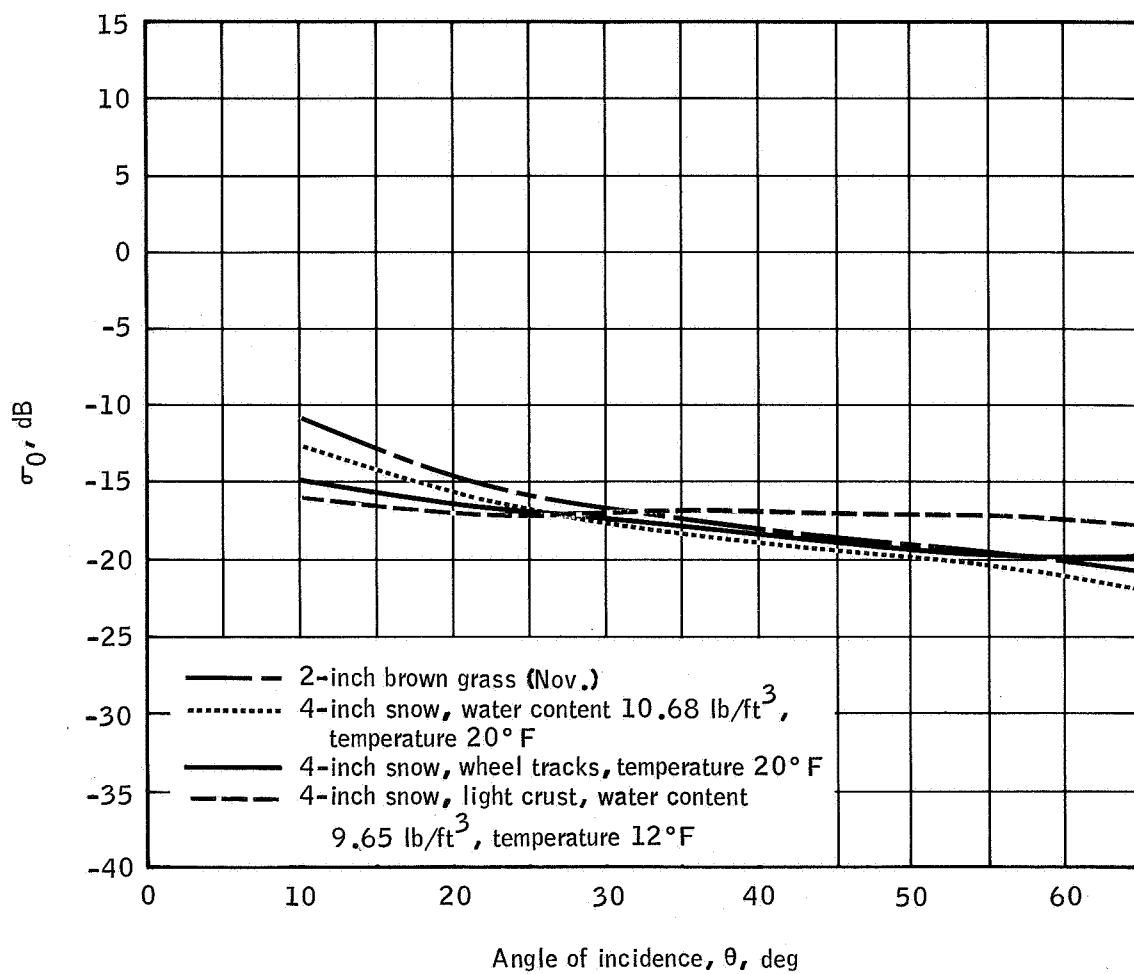


Figure A-2.- Vertical polarization data, K_u -band (ref. 5).

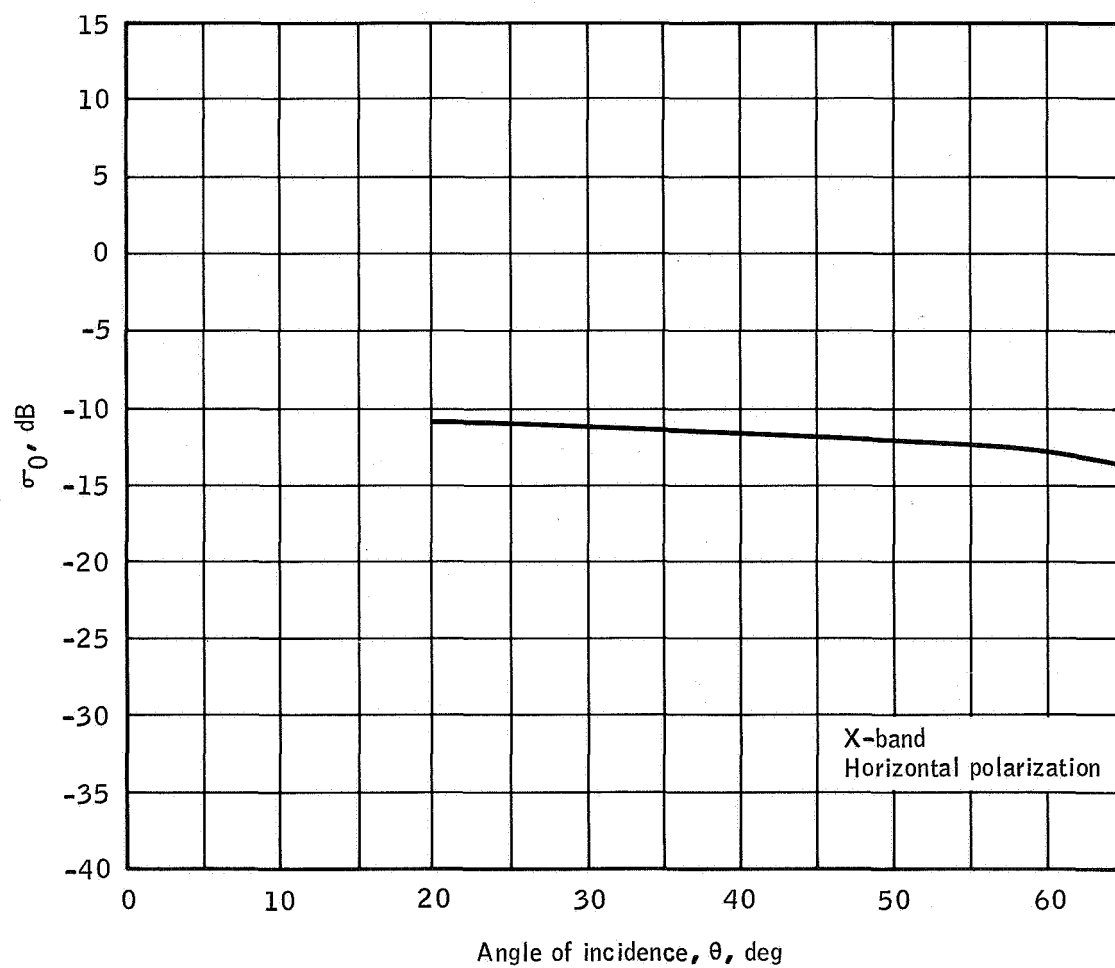


Figure A-3.- New Jersey trees (ref. 14).

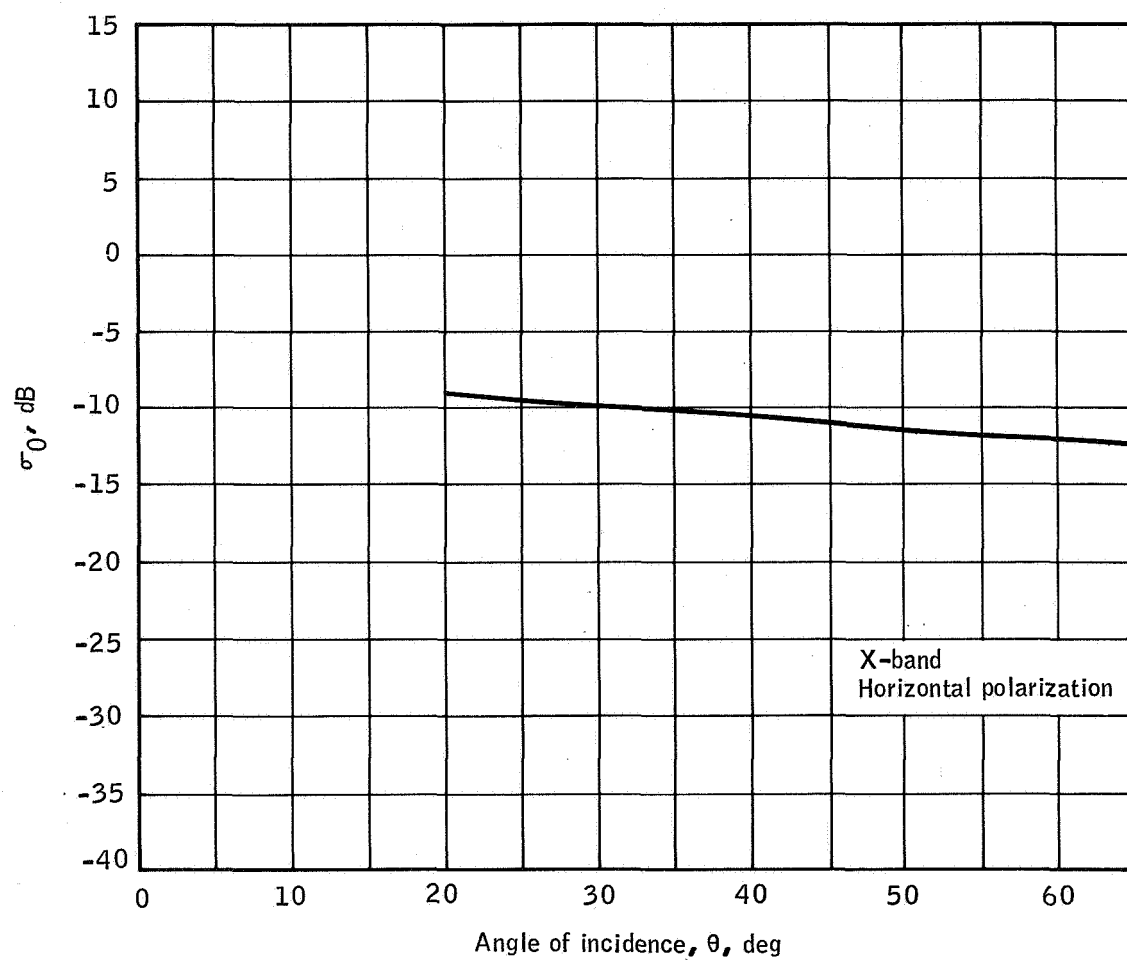
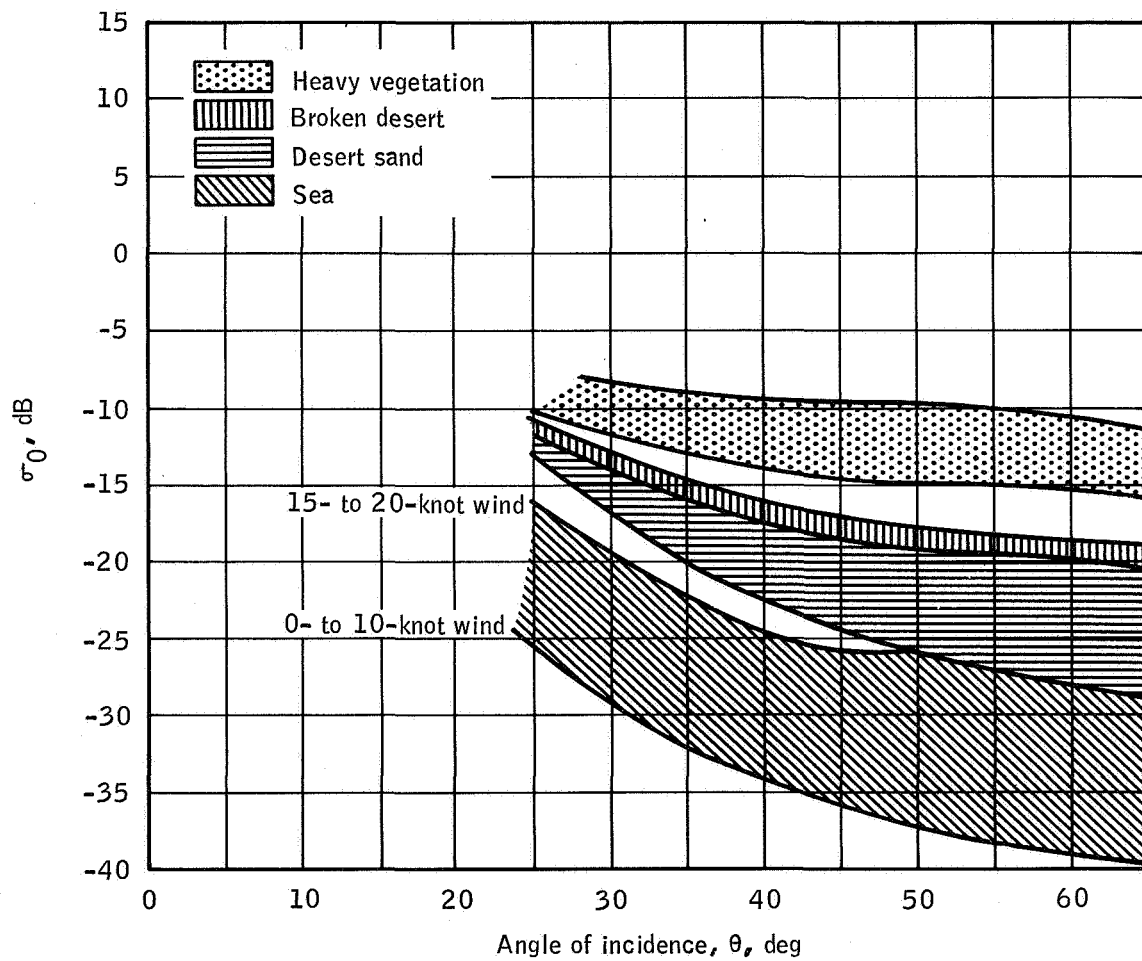
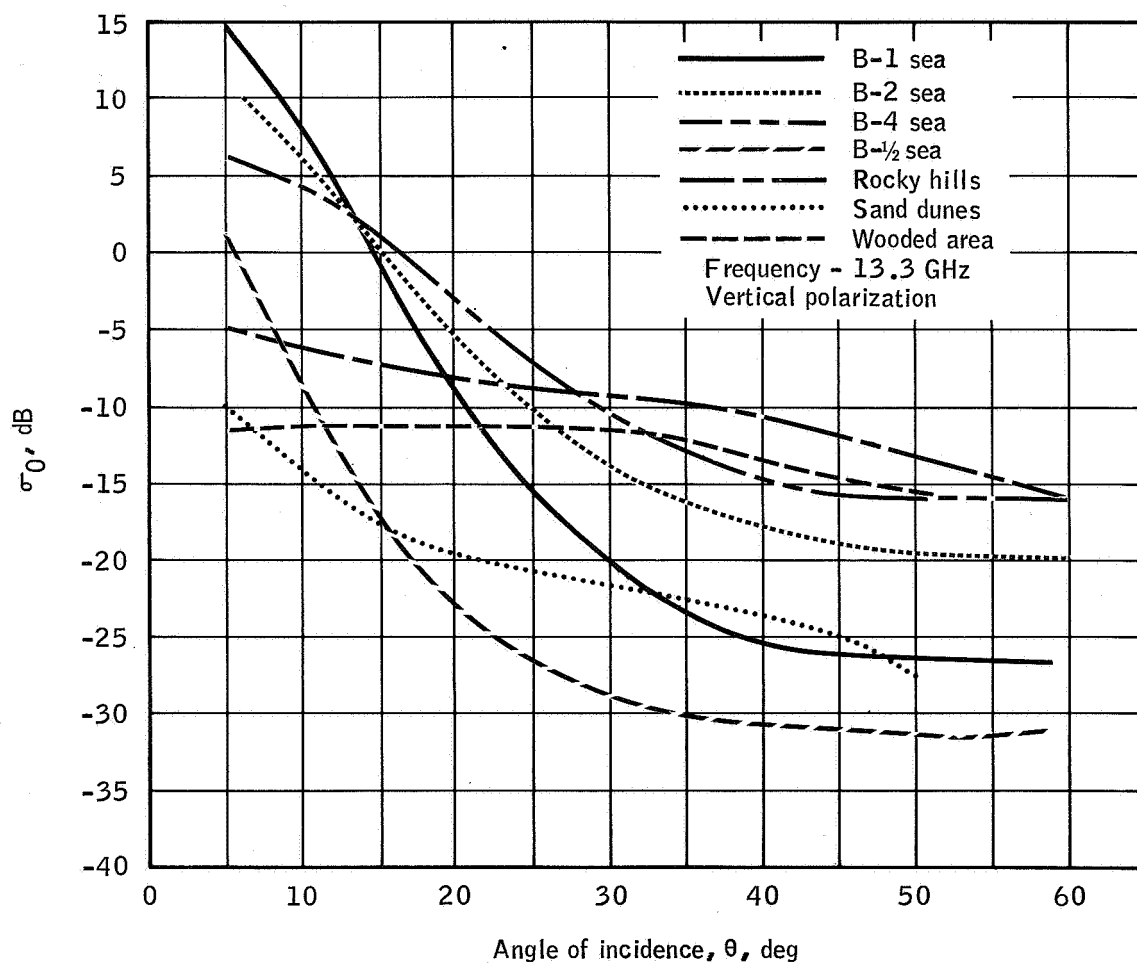


Figure A-4.- Florida mangrove (ref. 14).



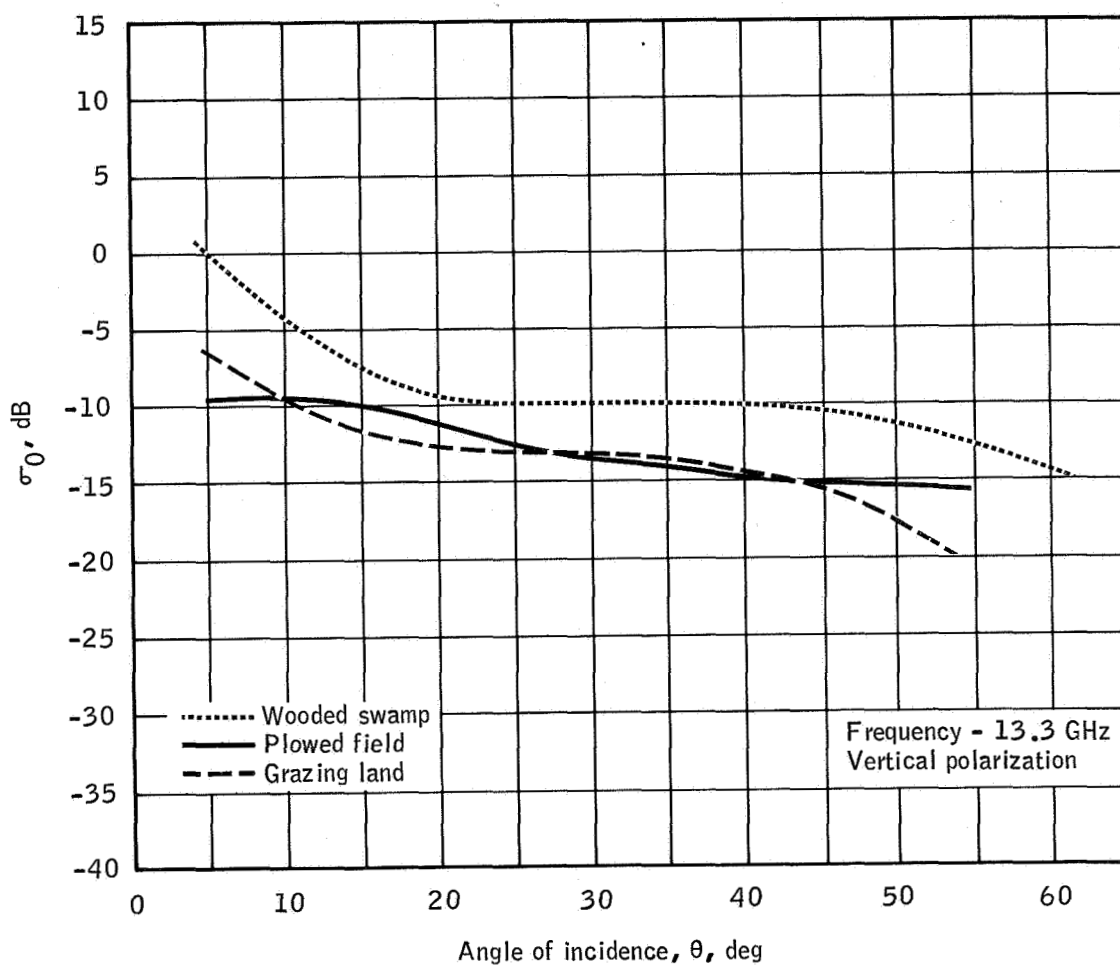
(a) Heavy vegetation, broken desert, desert sand, and sea.

Figure A-5.- The $\sigma_0(\theta)$ curves for various terrains (ref. 14).



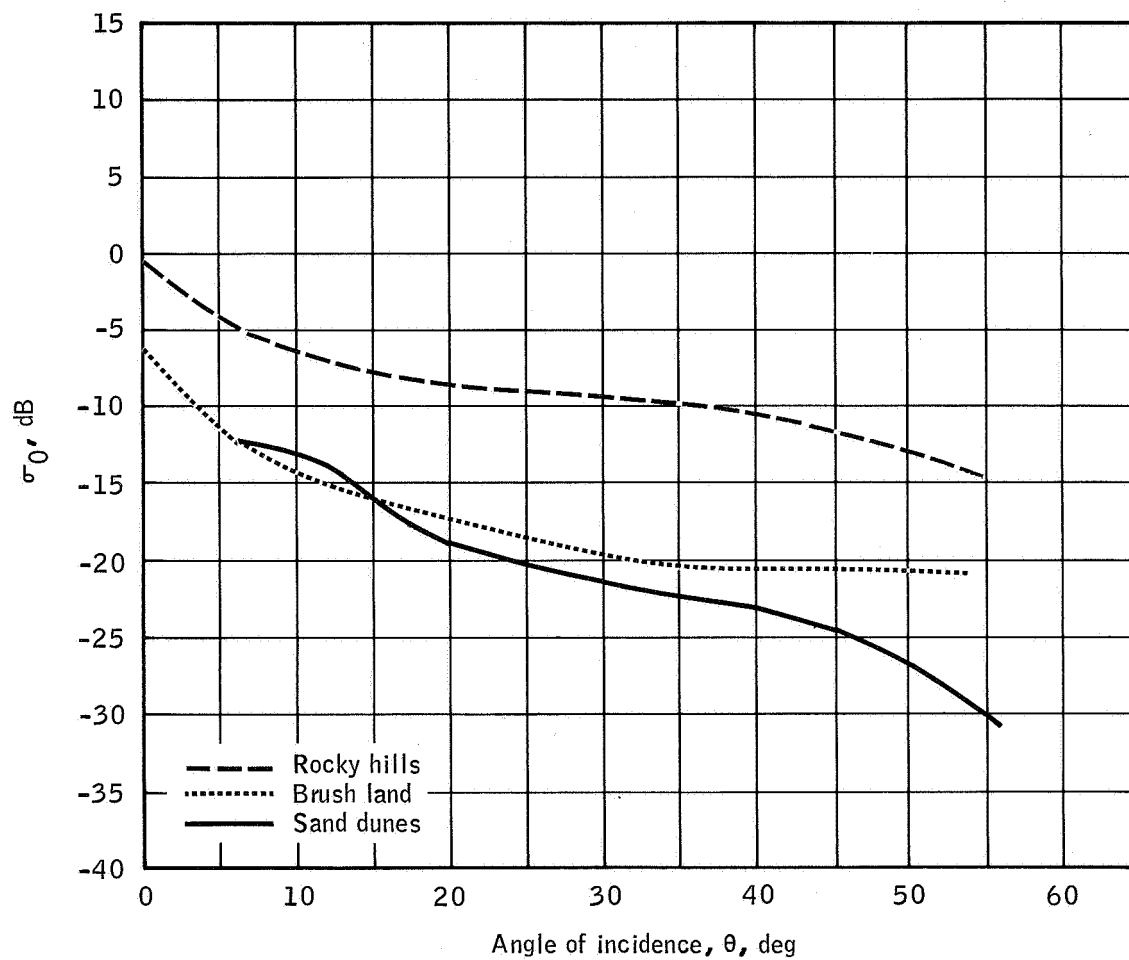
(b) Rocky hills, sand dunes, wooded area, and sea.

Figure A-5.- Continued (ref. 17).



(c) Grazing land, plowed fields, and wooded swamp.

Figure A-5.- Continued (ref. 17).



(d) Brushland, rocky hills, and sand dunes.

Figure A-5.- Concluded (ref. 17).

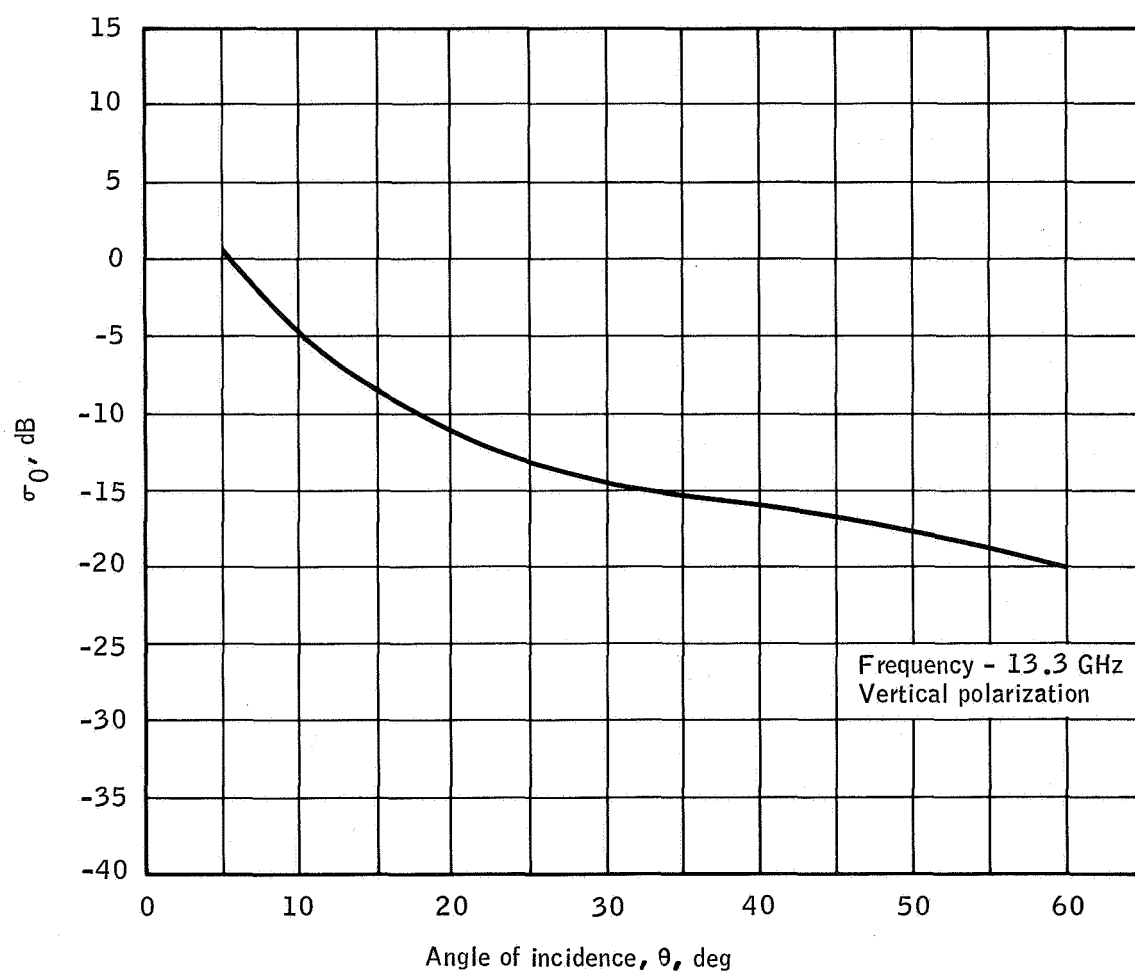


Figure A-6.- Normal desert terrain (ref. 18).

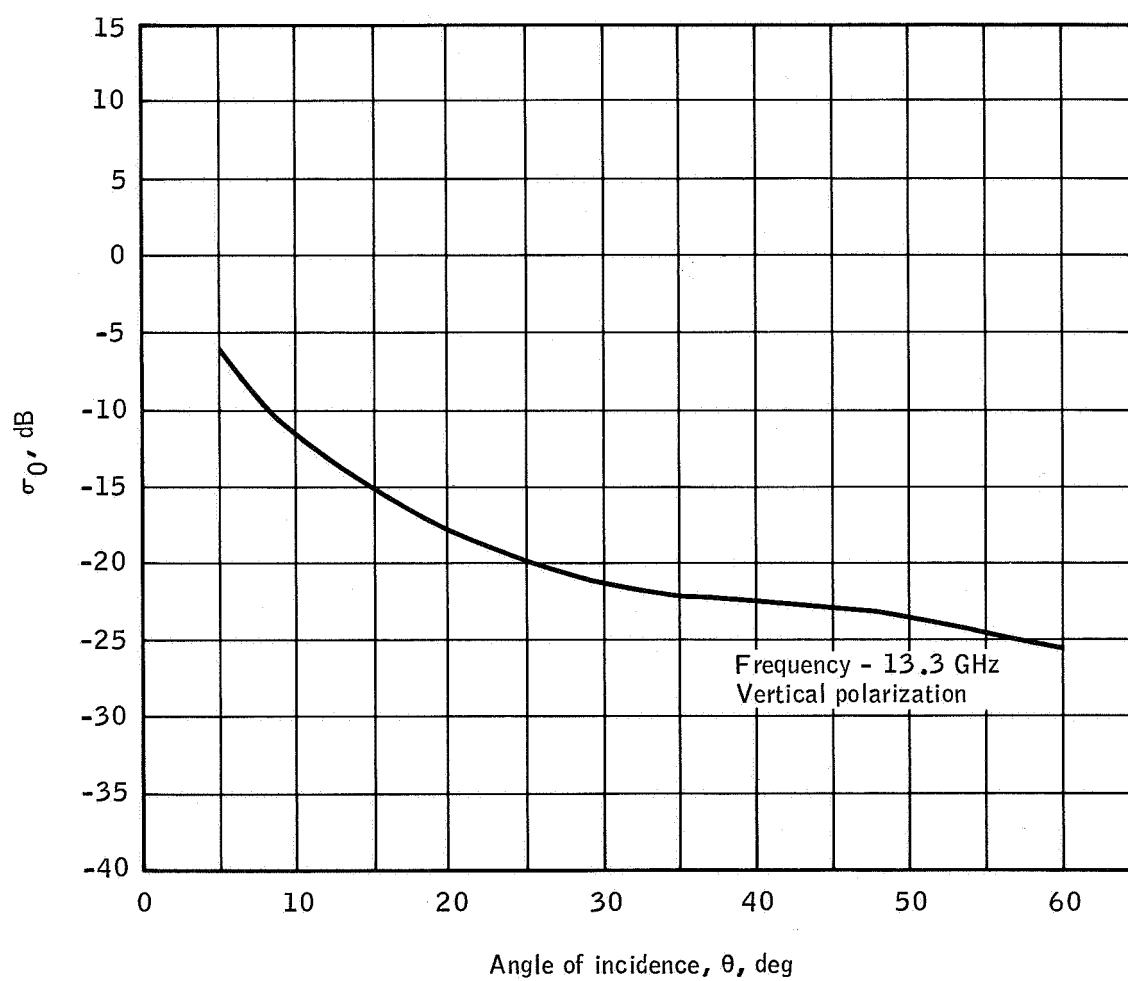


Figure A-7.- Desert terrain (AFS WC site).

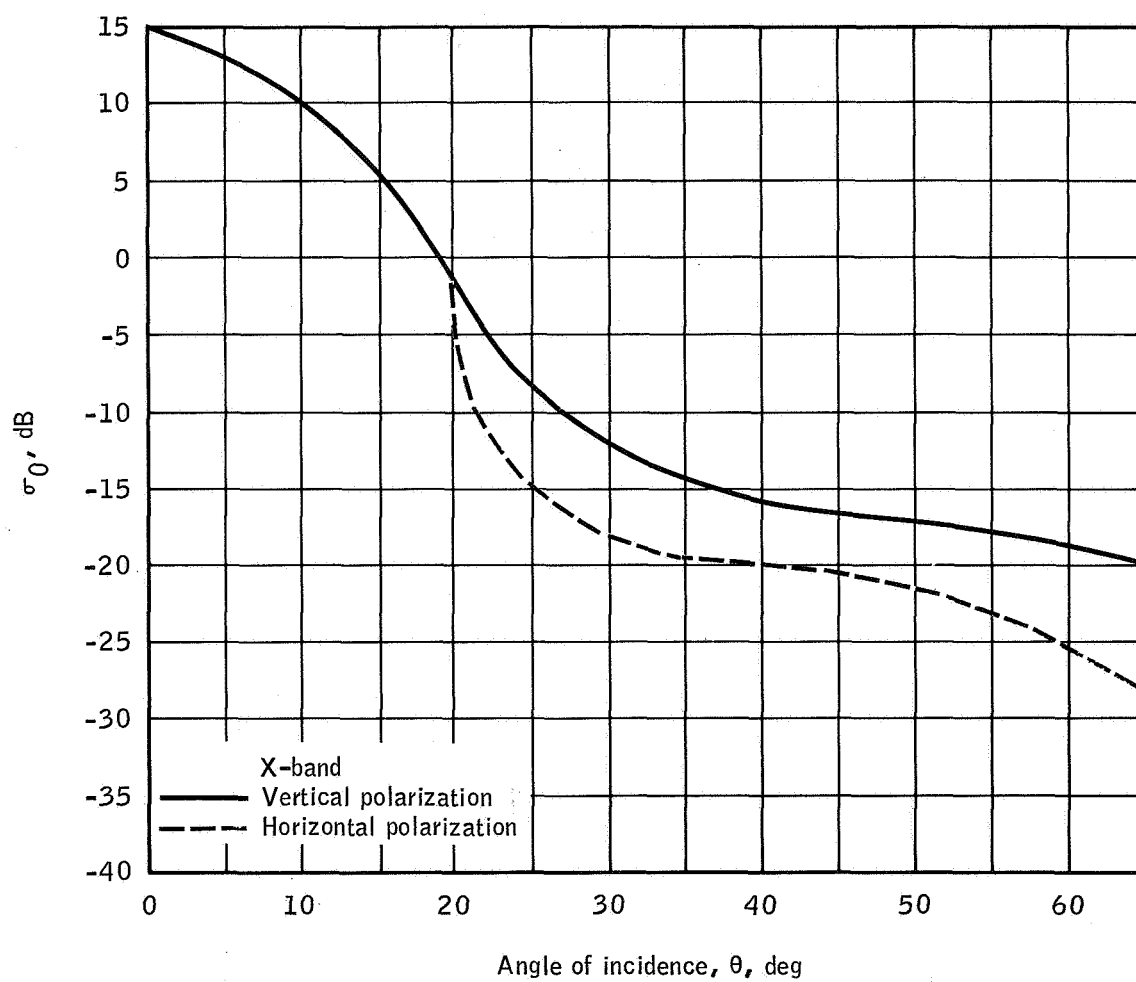


Figure A-8.- Lake Michigan, November 14 and 18, 1958 (ref. 25).

APPENDIX B

SCATTEROMETER DATA SAMPLES

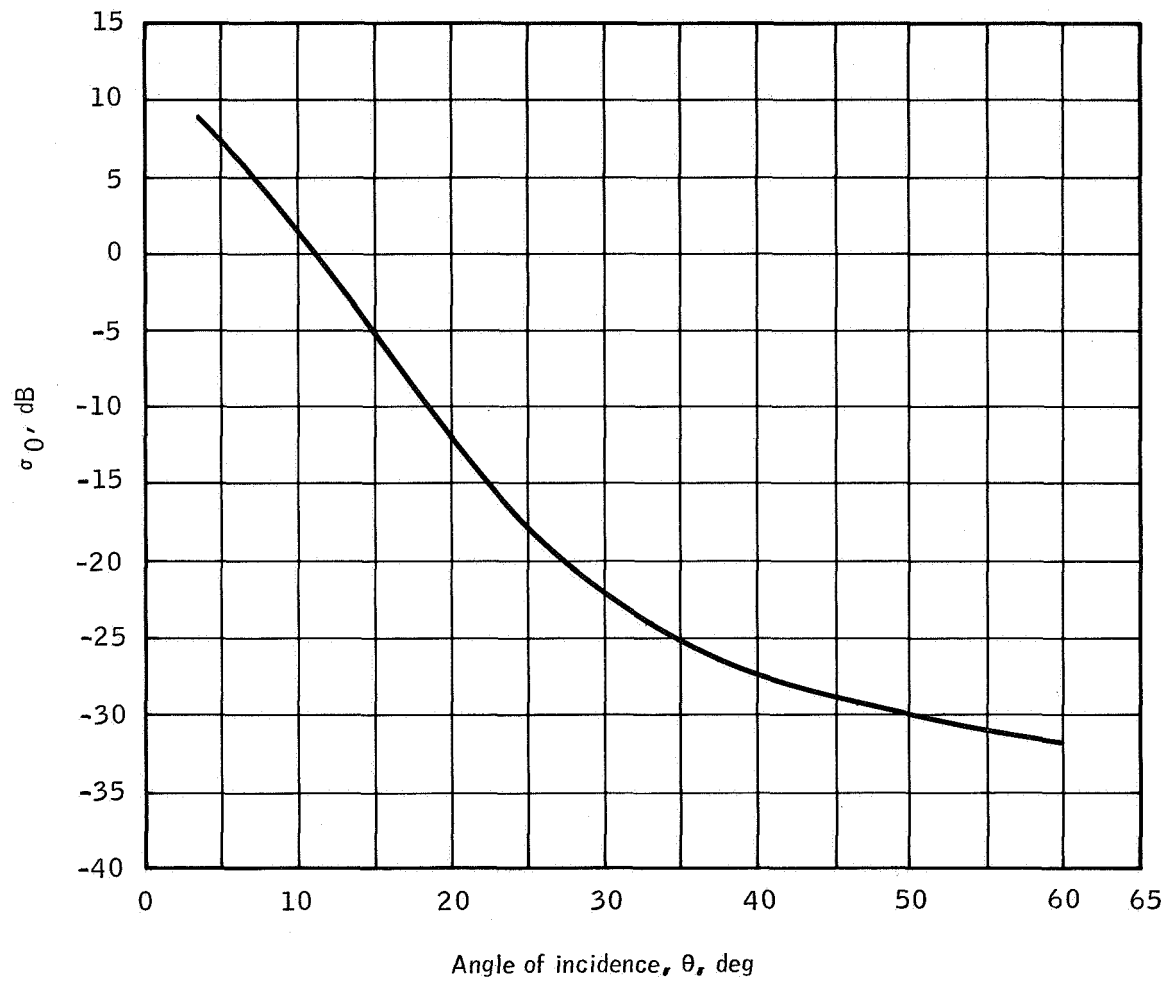
The data contained in this appendix include aerial photographs, flight maps, sample power-spectral-density curves, time histories, and plots of radar backscattering versus incidence angle.

SET 1 — FUNCTIONAL CHECK FLIGHT DATA

Site: Matagorda Bay, Texas
Beaufort 1 sea state
Altitude: 3000 feet
Time: 1150 c.s.t.

These data were taken from the NASA 926 aircraft over Matagorda Bay, Texas, during a systems checkout flight and have served as a comparison base line for scatterometer data quality. At approximately 1151:45, the aircraft passed over a causeway crossing the bay. This is evident in time-history data samples, particularly around the 5-kHz frequency level.

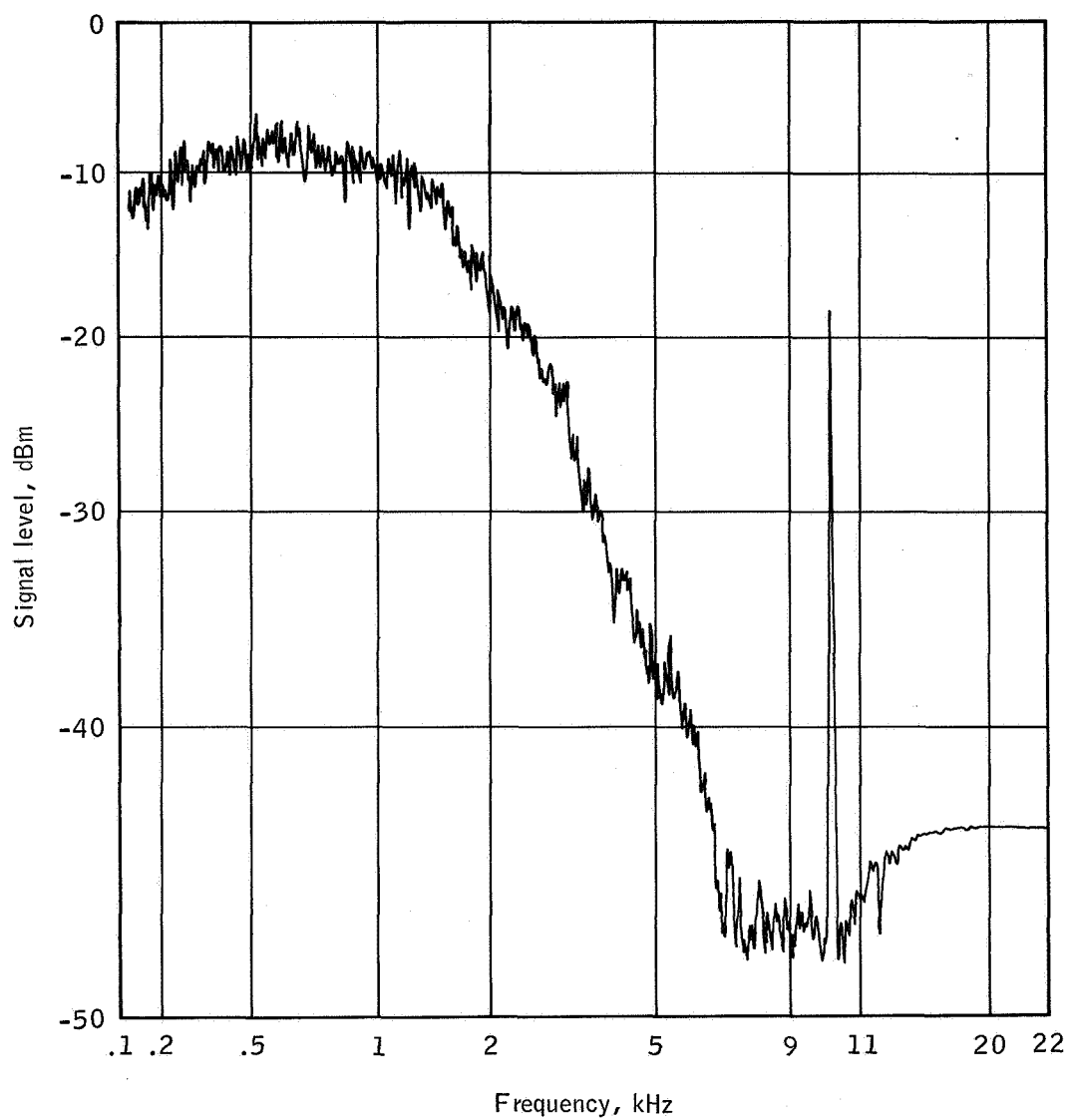
The shape of the resultant $\sigma_0(\theta)$ curve follows previously published data for Beaufort 1 (B-1) sea condition (ref. 15), although the absolute signal levels for these data are consistently 5 dB lower than the signal levels for a B-1 sea condition. This would indicate a water condition somewhat smoother than B-1 but not as smooth as B-1/2.



	σ_0 sample time		
Site, Matagorda Bay	Hours / minutes / seconds		
Tape Functional check flight	<u>11</u>	<u>50</u>	<u>30</u>
Through	<u>11</u>	<u>50</u>	<u>40</u>

(a) The $\sigma_0(\theta)$ curve.

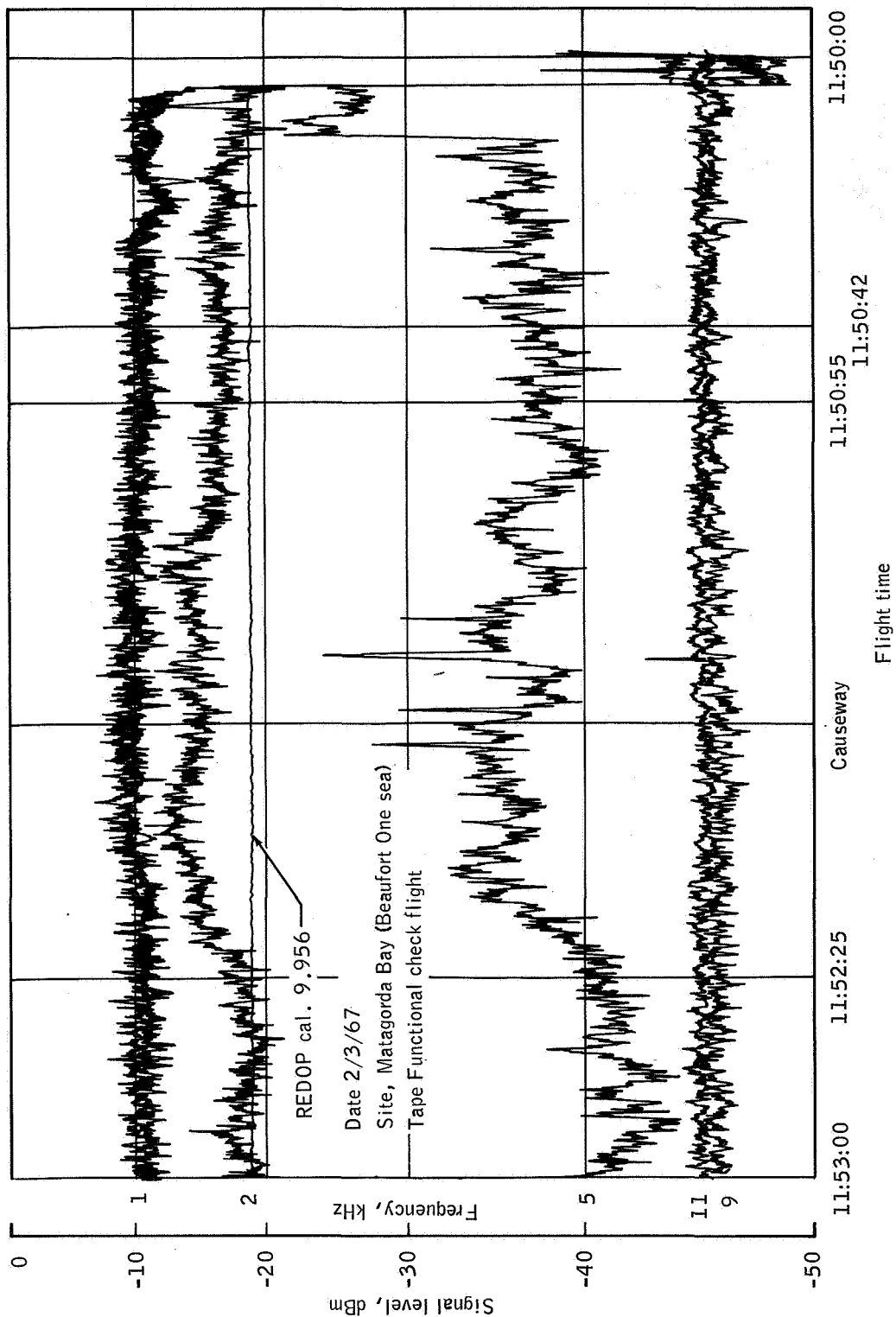
Figure B-1.- Set 1 data samples.



Date 2/3/67
Site, Matagorda Bay
Tape Functional check flight

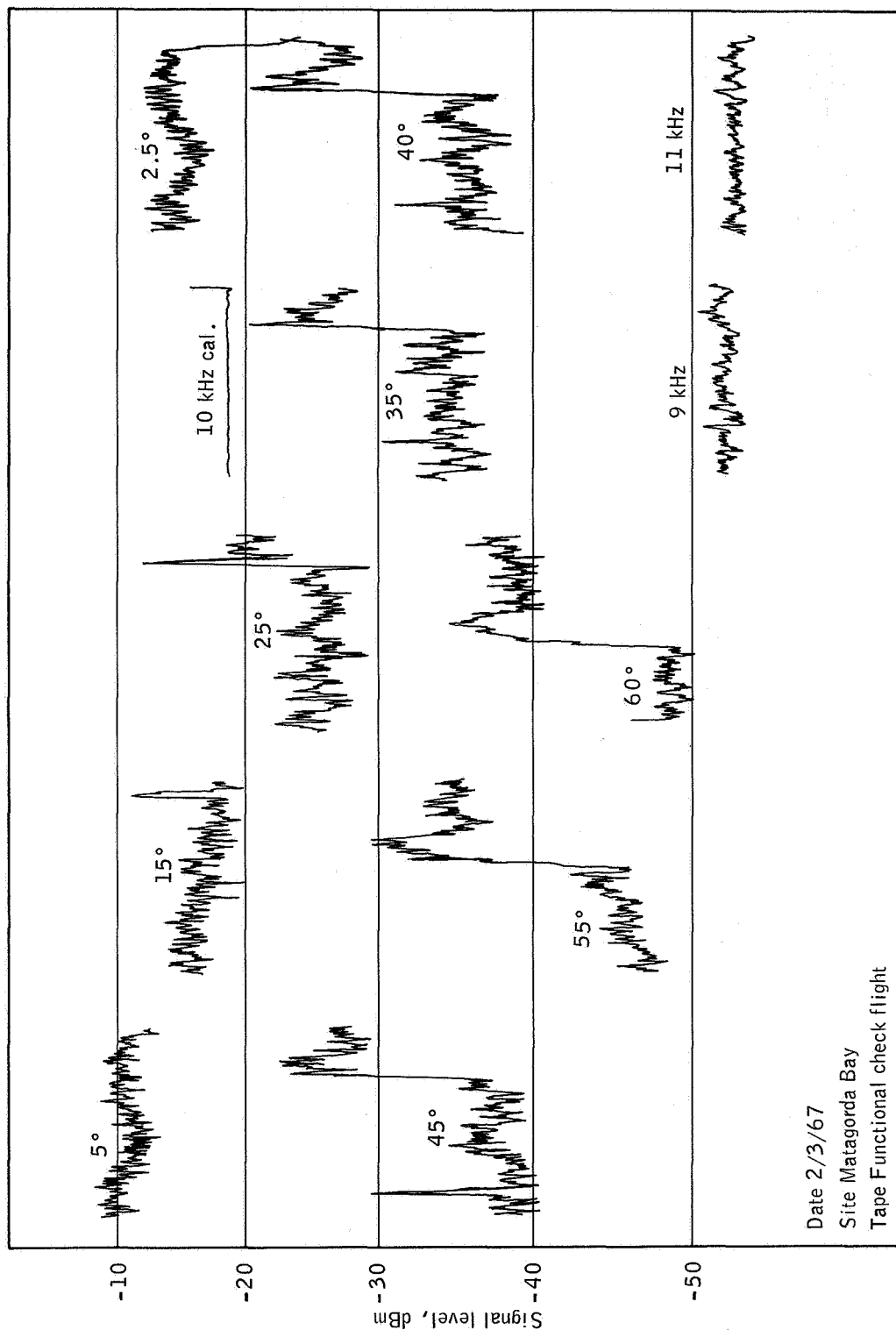
(b) The PSD curve.

Figure B-1.- Continued.



(c) Time history, longtime intervals.

Figure B-1.- Continued.



(d) Time history, short time intervals.

Figure B-1.- Concluded.

SET 2 — MISSION DATA

Mission/flight/line/run

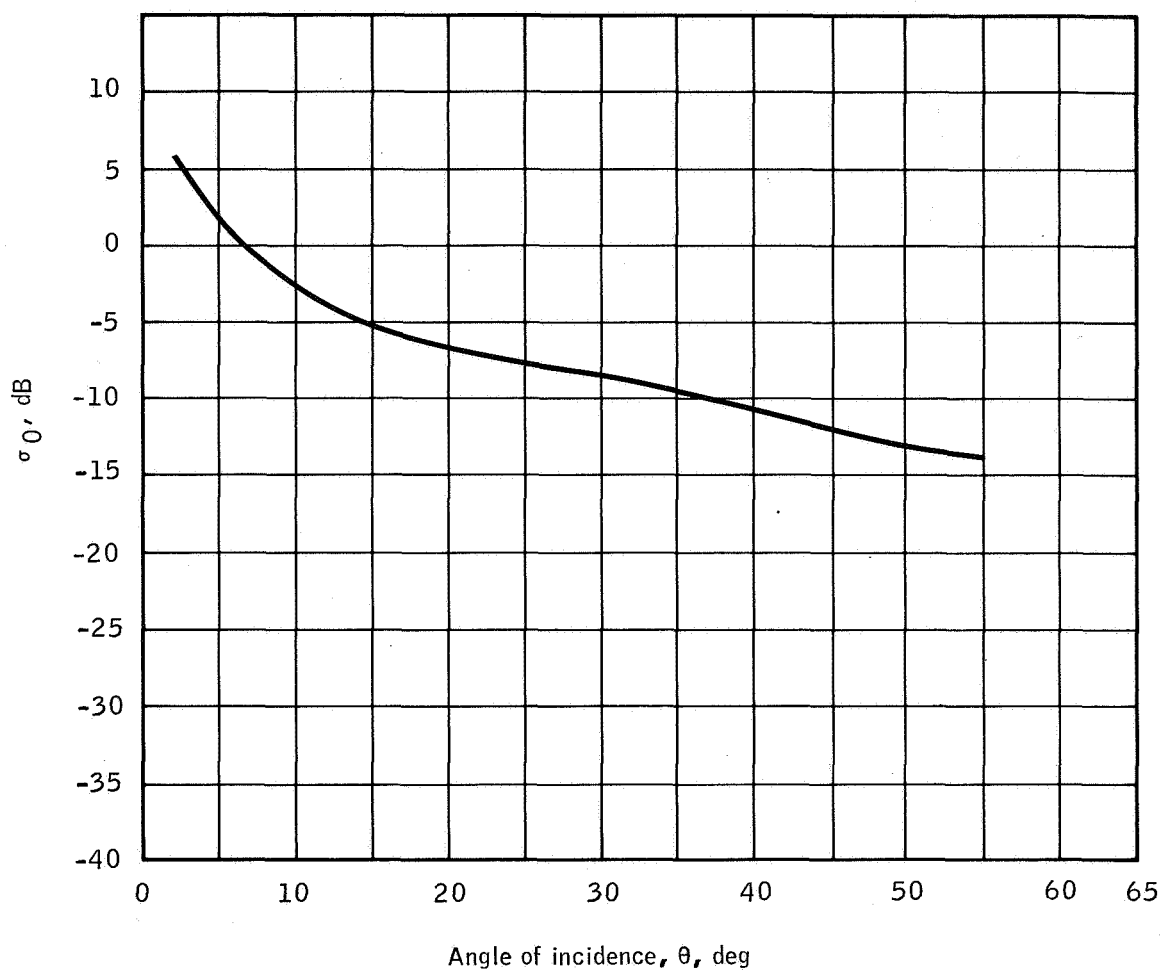
21 5 1 2

Site 2, Pisgah Crater, California
Altitude: 3000 feet
Time: 1415 P.s.t.
Infrared color film

These data samples were taken over the desert area northwest of the Pisgah cone which is shown on the accompanying flight map. The vegetation cover is approximately 5 percent; the surface macrorelief is from 3 to 5 feet in height. The area is very dry and has an annual rainfall of less than 6 inches.

The $\sigma_0(\theta)$ curve shown in this section averages from 5 to 7 dB higher than the reference curves for a "normal desert" (ref. 18). An examination of the PSD and the time-history plots shows the presence of two interference "spikes," the occurrence of which is time dependent. The PSD plot can be correlated with the initial triggering pulse to the RC-8 cartographic camera. The time-history plot appears to be the return film-transported pulse.

The principal effect of these pulses on the scatterometer data is to decrease the apparent level of the calibration signal by approximately 7 dB. If this is taken into account, the $\sigma_0(\theta)$ curve may be replotted to yield a normal signature for this type of desert terrain.



Site 2, Pisgah Crater

Tape 75 - 0005

Mission / flight / line / run
21 5 1 2

σ_0 sample time

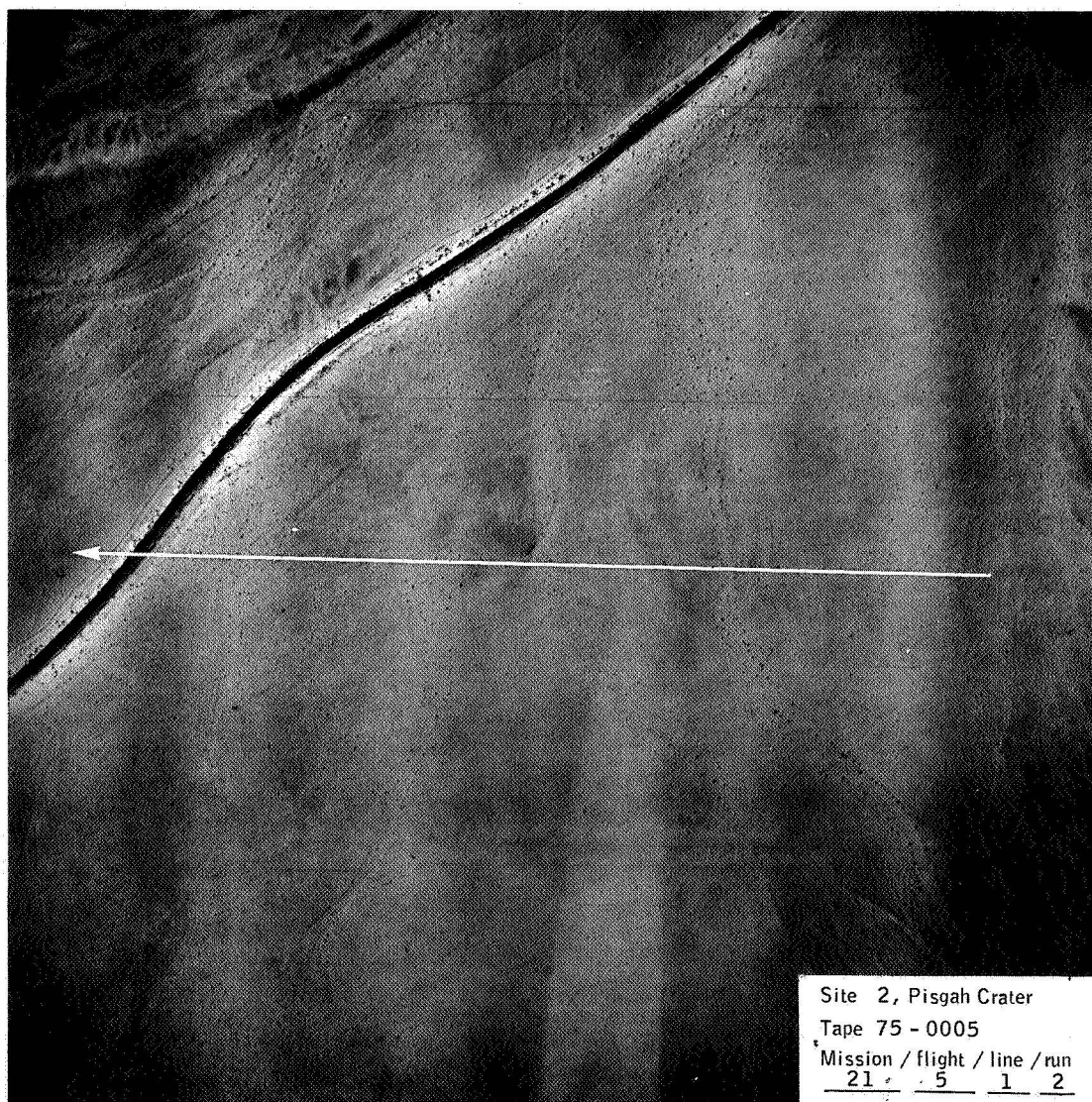
Hours / minutes / seconds

14 15 34

Through 14 15 38

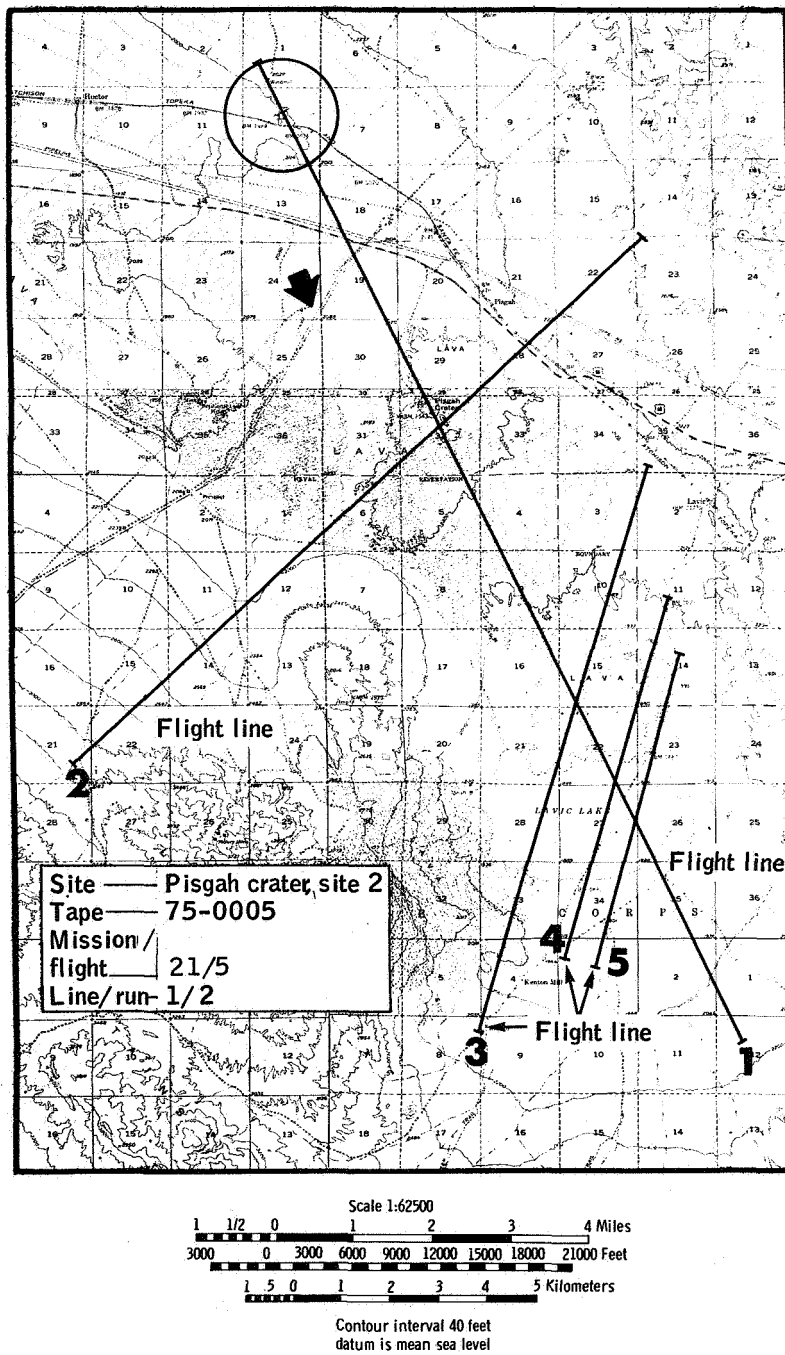
(a) The $\sigma_0(\theta)$ curve.

Figure B-2.- Set 2 data samples.



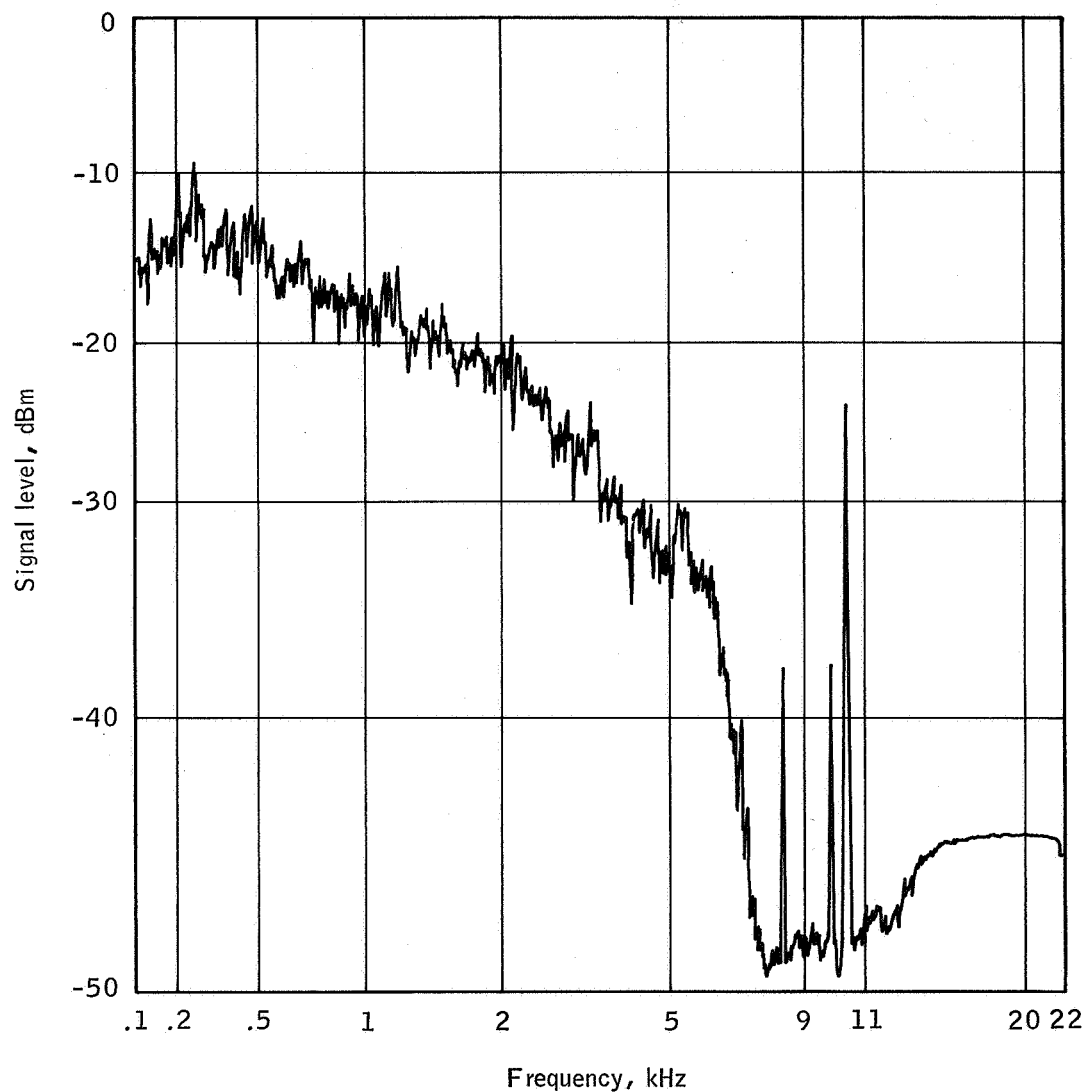
(b) Flight line.

Figure B-2.- Continued.



(c) Flight map.

Figure B-2.— Continued.



Site 2, Pisgah Crater

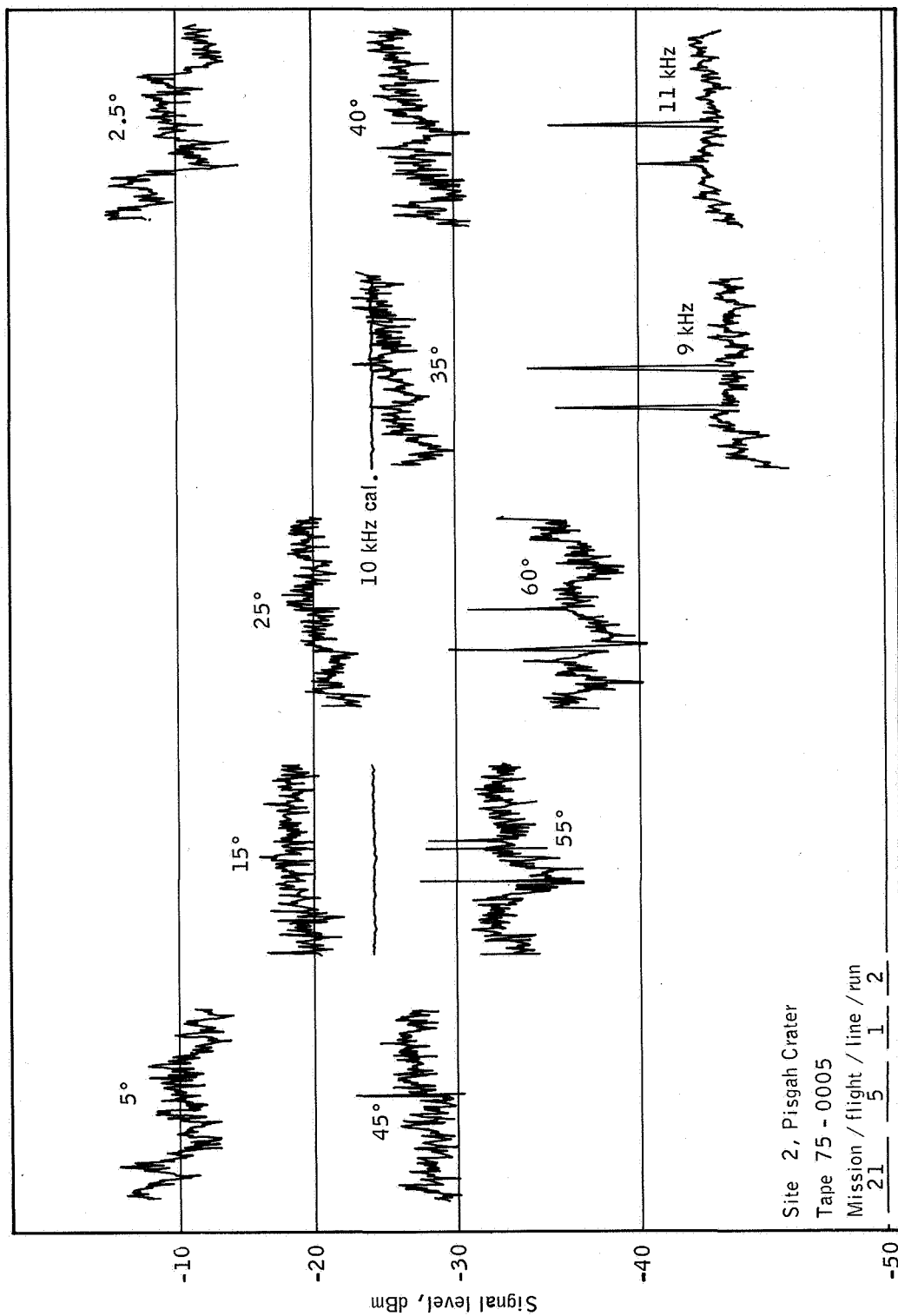
Tape 75 - 0005

Mission / flight / line / run

21 5 1 2

(d) The PSD curve.

Figure B-2.- Continued.



(e) Time history.

Figure B-2.- Concluded.

SET 3 — MISSION DATA

Mission/flight/line/run

21 5 1 3

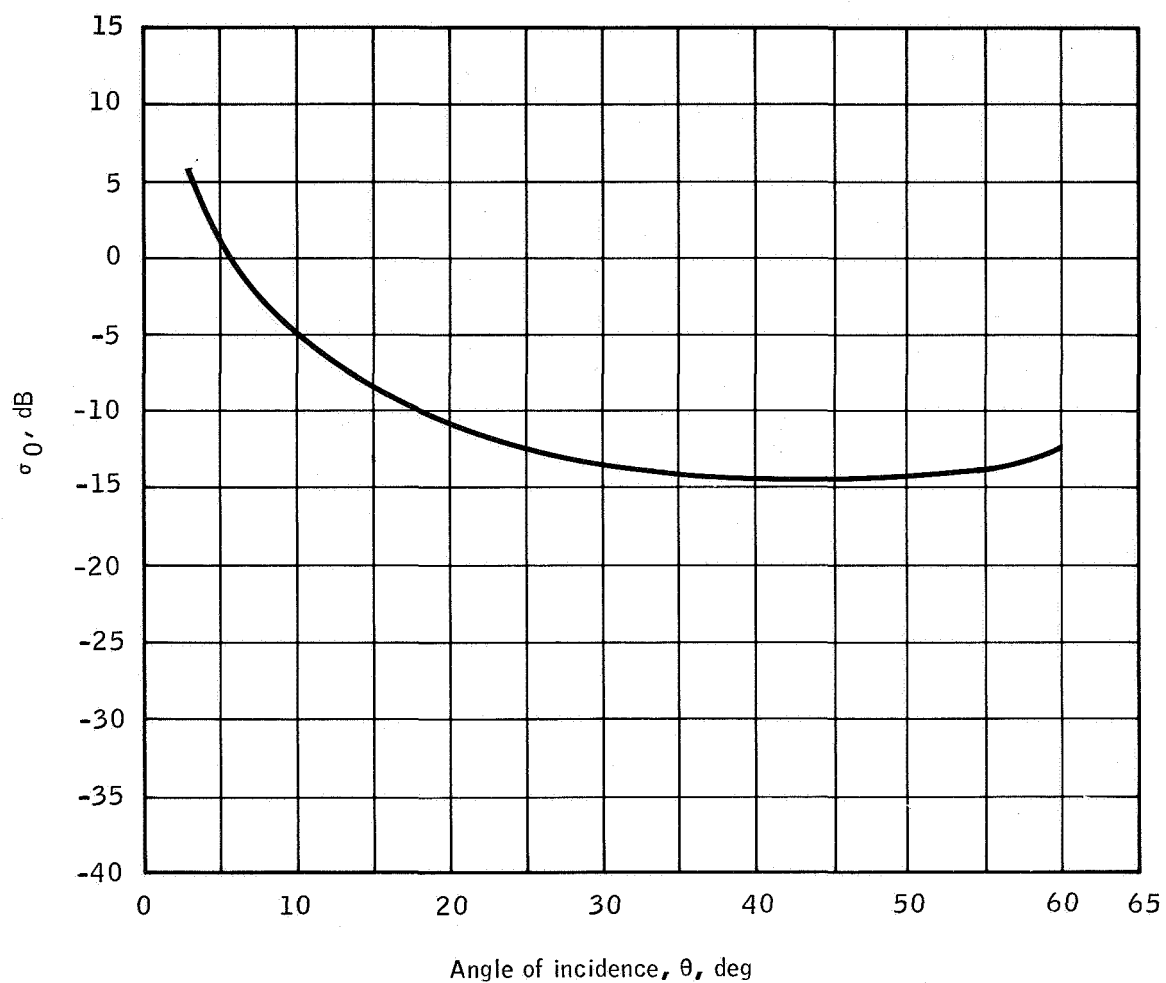
Site 2, Pisgah Crater, California

Altitude: 4000 feet

Time: 1504 P.s.t.

Plus-X film

The $\sigma_0(\theta)$ data shown in this section are characteristic of the terrain near the northern end of line 1 and, in the 0° to 40° range, compare favorably with reference curves (refs. 14, 15, and 17). The increased signal level in the region of 45° to 60° is a function of the rougher terrain as seen by the scatterometer at these angles (shown in the accompanying photograph).



Site 2, Pisgah Crater

Tape 75 - {0006 }

Mission / flight / line / run

21 5 1 3

σ_0 sample time

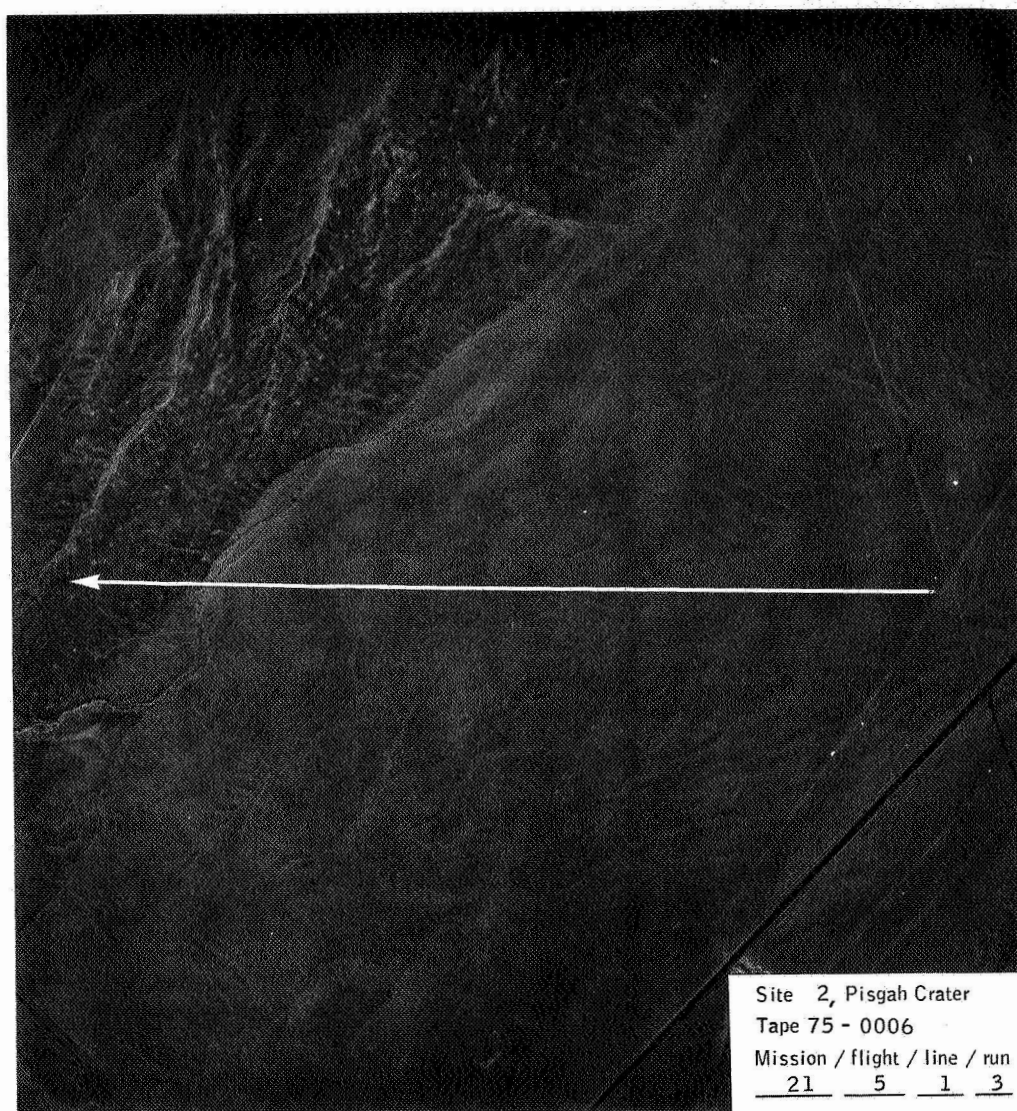
Hours / minutes / seconds

15 03 38

Through 15 04 08

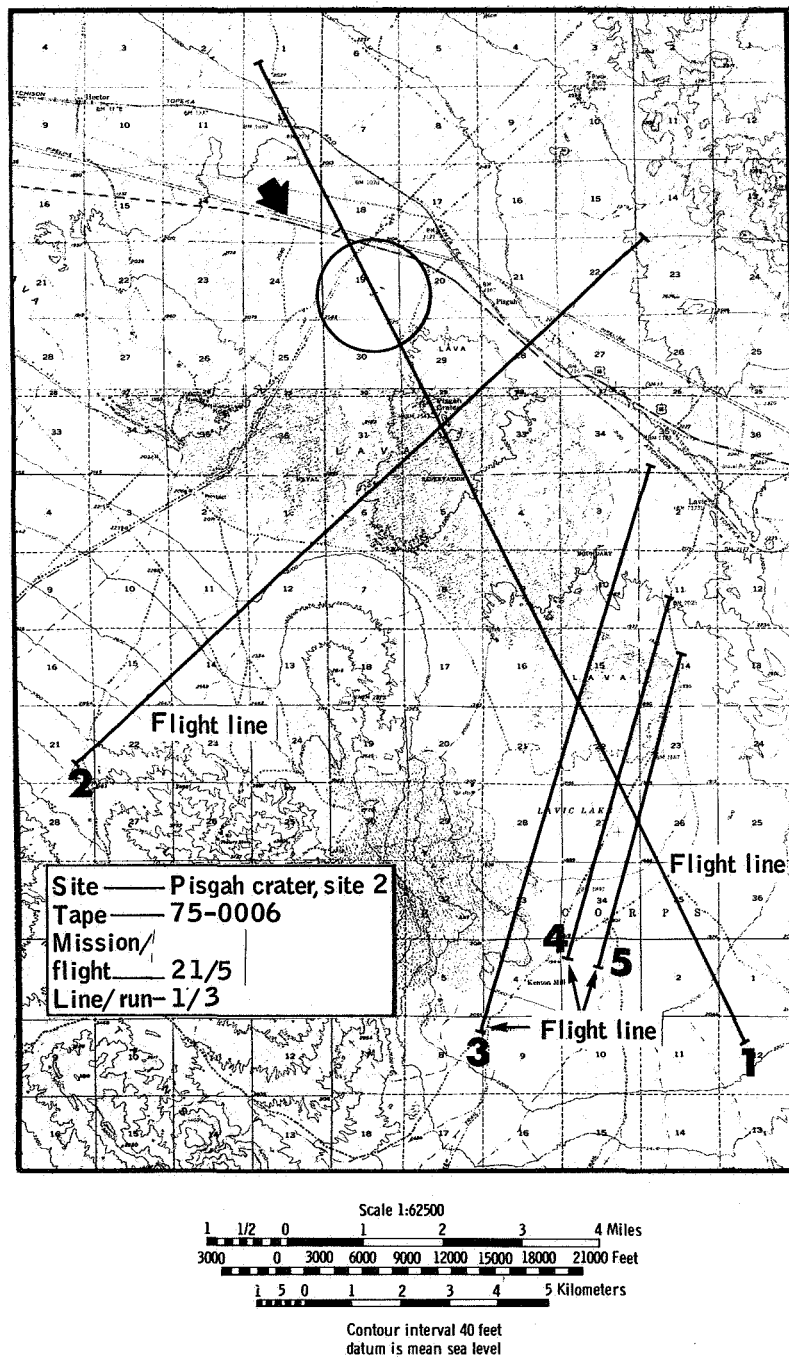
(a) The $\sigma_0(\theta)$ curve.

Figure B-3.- Set 3 data samples.



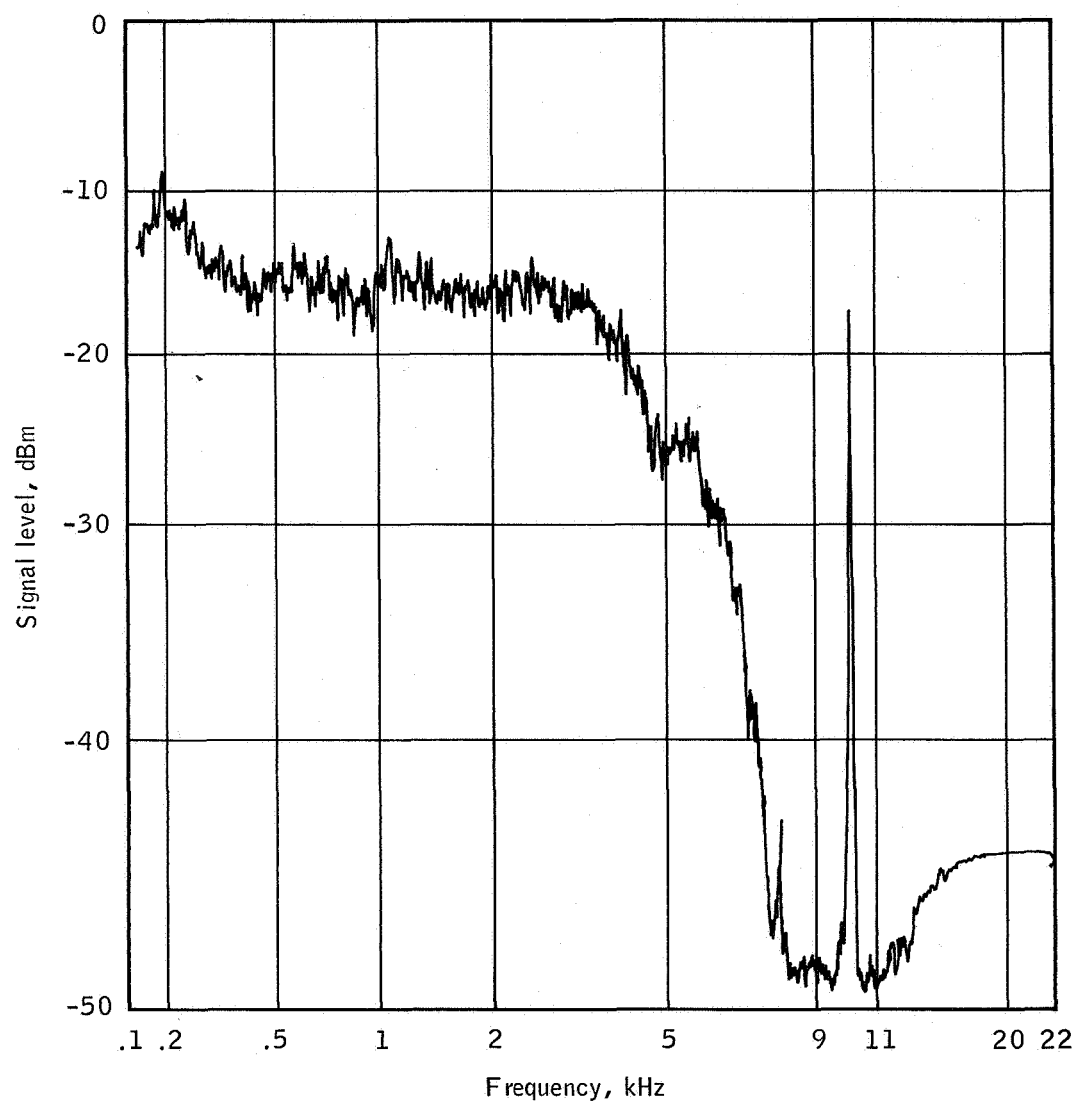
(b) Flight line.

Figure B-3.- Continued.



(c) Flight map.

Figure B-3.- Continued.



Site 2, Pisgah Crater

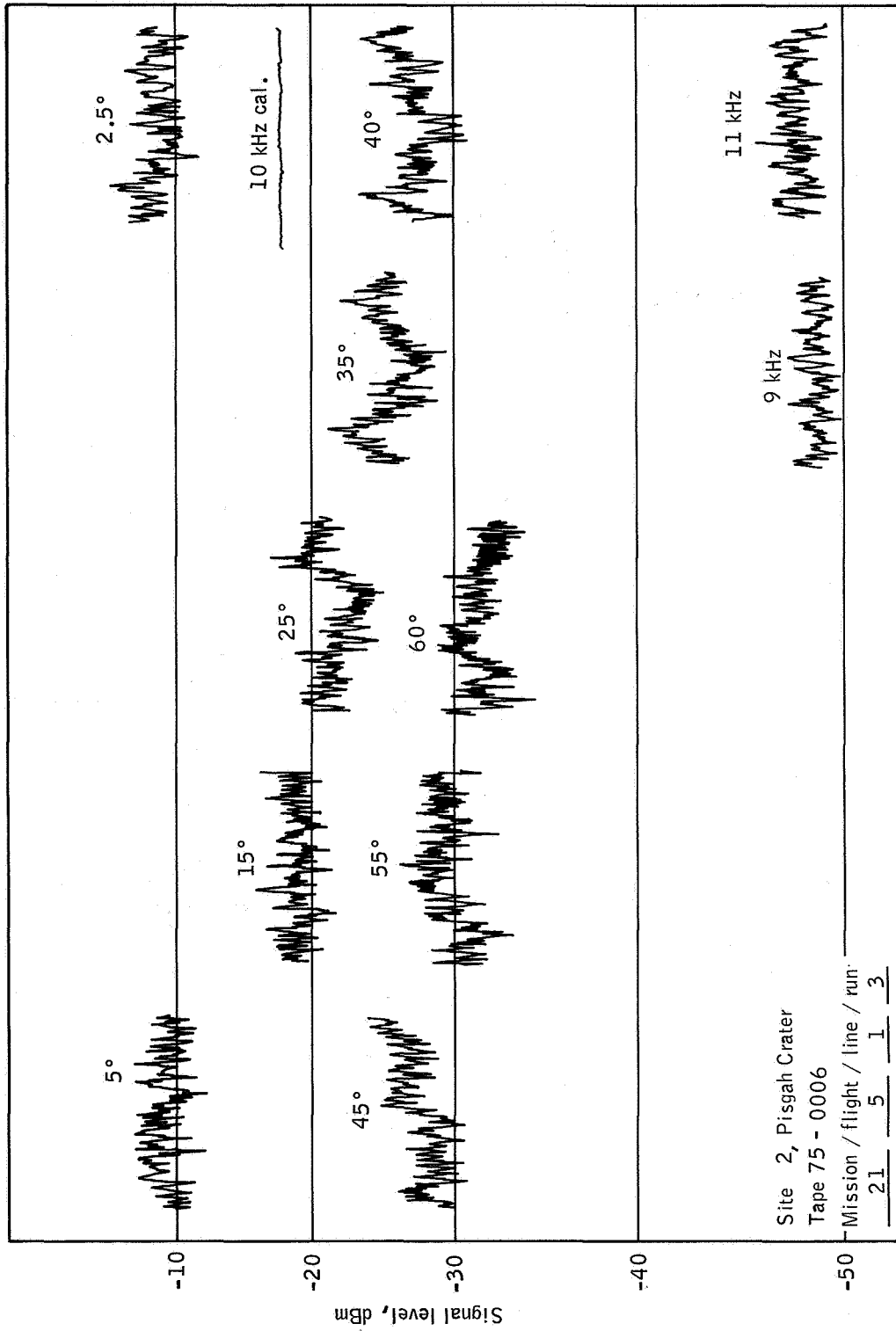
Tape 75 - 0006

Mission / flight / line / run

21 5 1 3

(d) The PSD curve.

Figure B-3.- Continued.



(e) Time history.

Figure B-3.- Concluded.

SET 4 — MISSION DATA

Mission/flight/line/run
23 1 1 1

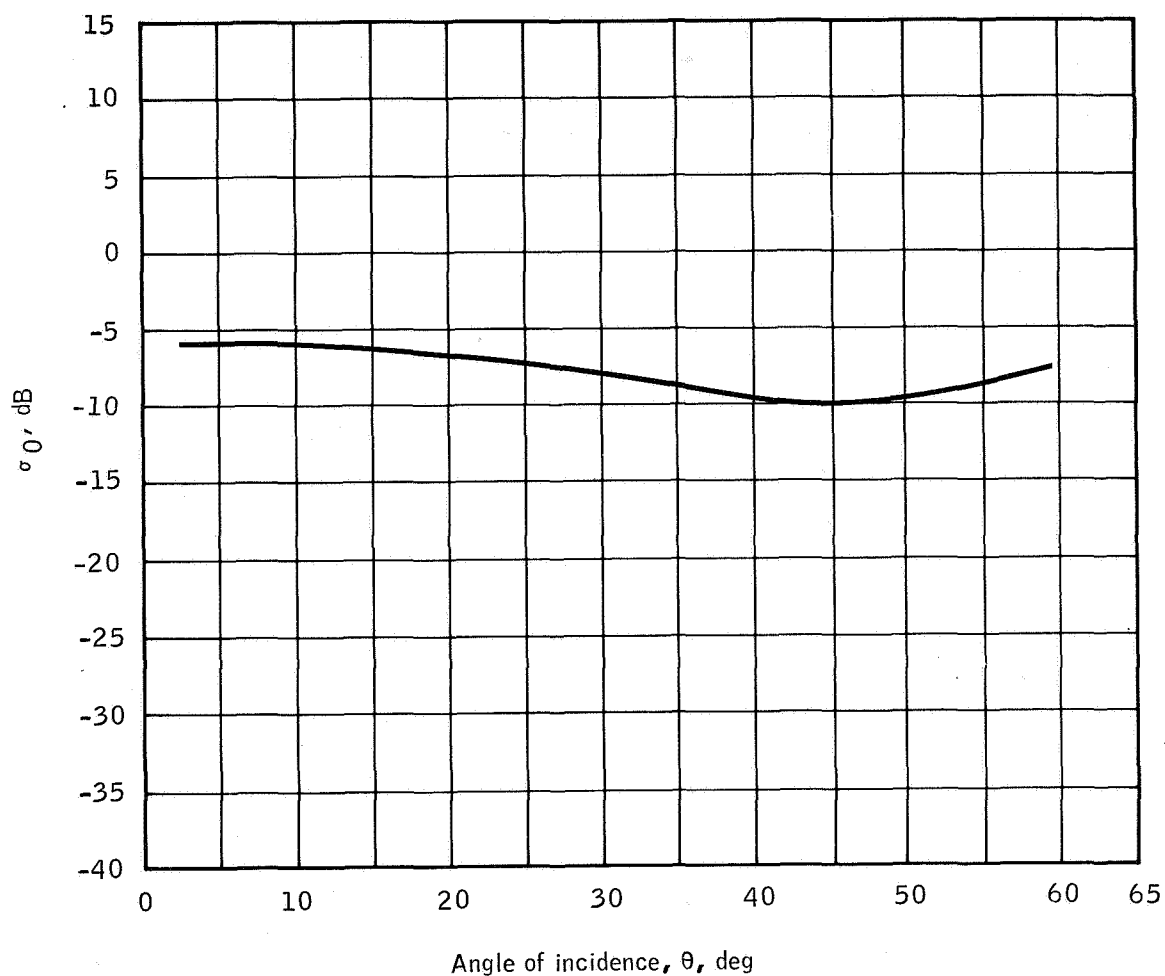
Site 46, Asheville Basin, North Carolina

Altitude: 4200 feet

Time: 1104 e.s.t.

Ektachrome color film

These data samples were taken over forested terrain with considerable variance in tree height along the radar-illuminated path. The $\sigma_0(\theta)$ curve for this area is somewhat irregular; however, the average value compares well with reference curves (refs. 14 and 15) and is approximately 2 dB lower than that reported for the New Jersey woods in reference 13 and 4 dB higher than the curve for the New Jersey trees in reference 14.



Site 46, Asheville Basin
 Tape 75 - 0017
 Mission / flight / line / run
23 1 1 1

σ_0 sample time
 Hours / minutes / seconds
11 03 37
 Through 11 04 07

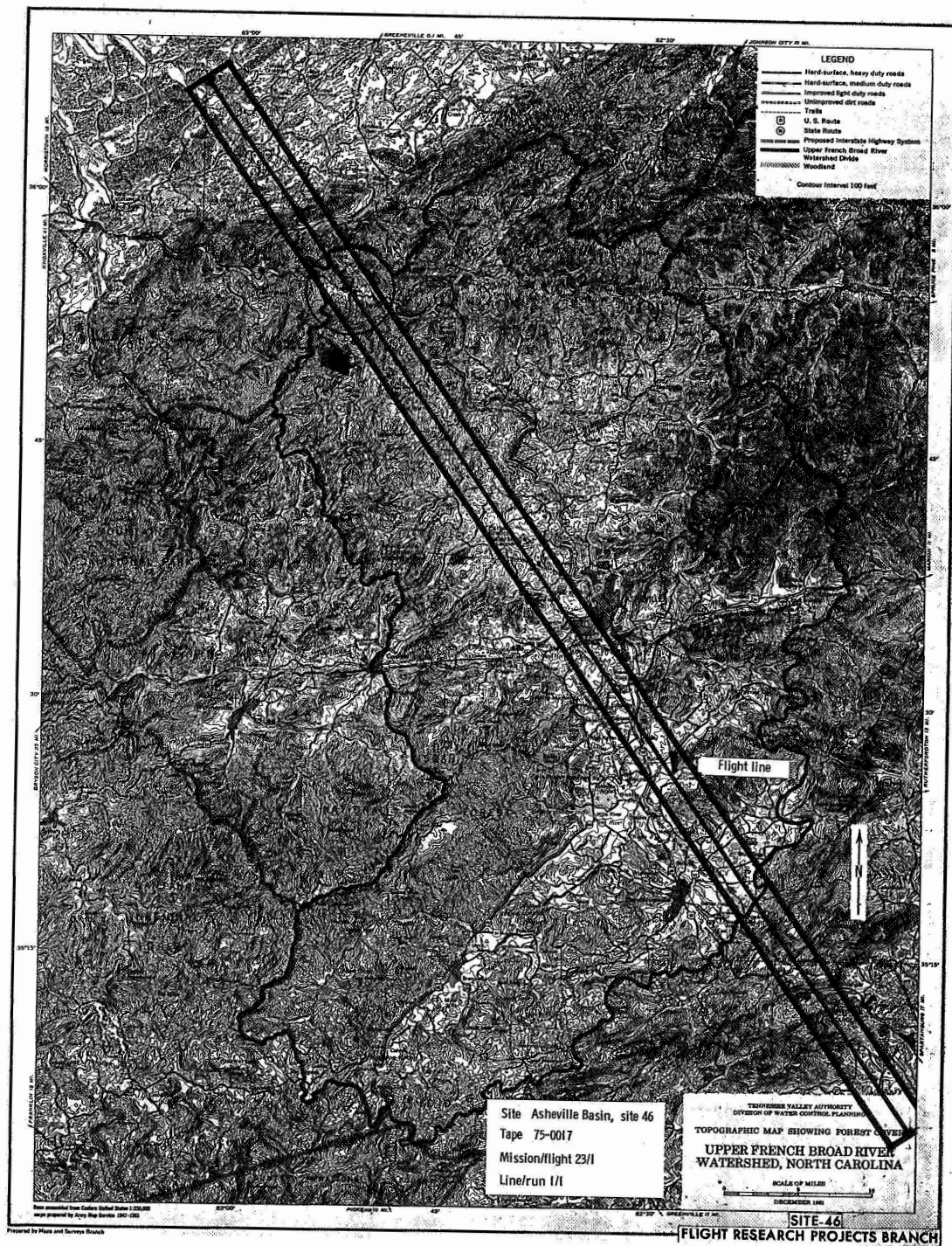
(a) The $\sigma_0(\theta)$ curve.

Figure B-4.- Set 4 data samples.



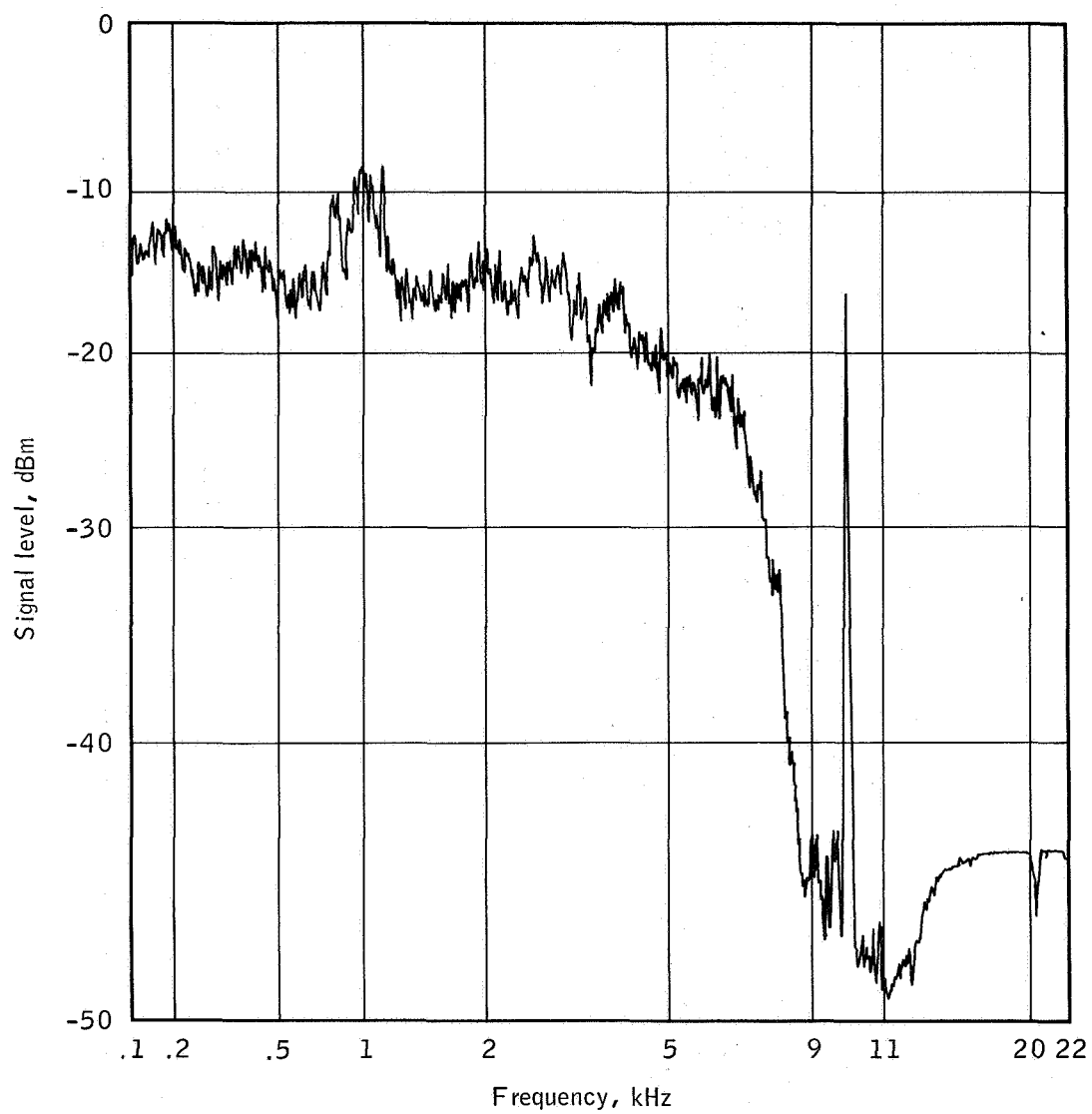
(b) Flight line.

Figure B-4.- Continued.



(c) Flight map.

Figure B-4.- Continued.



Site 46, Asheville Basin

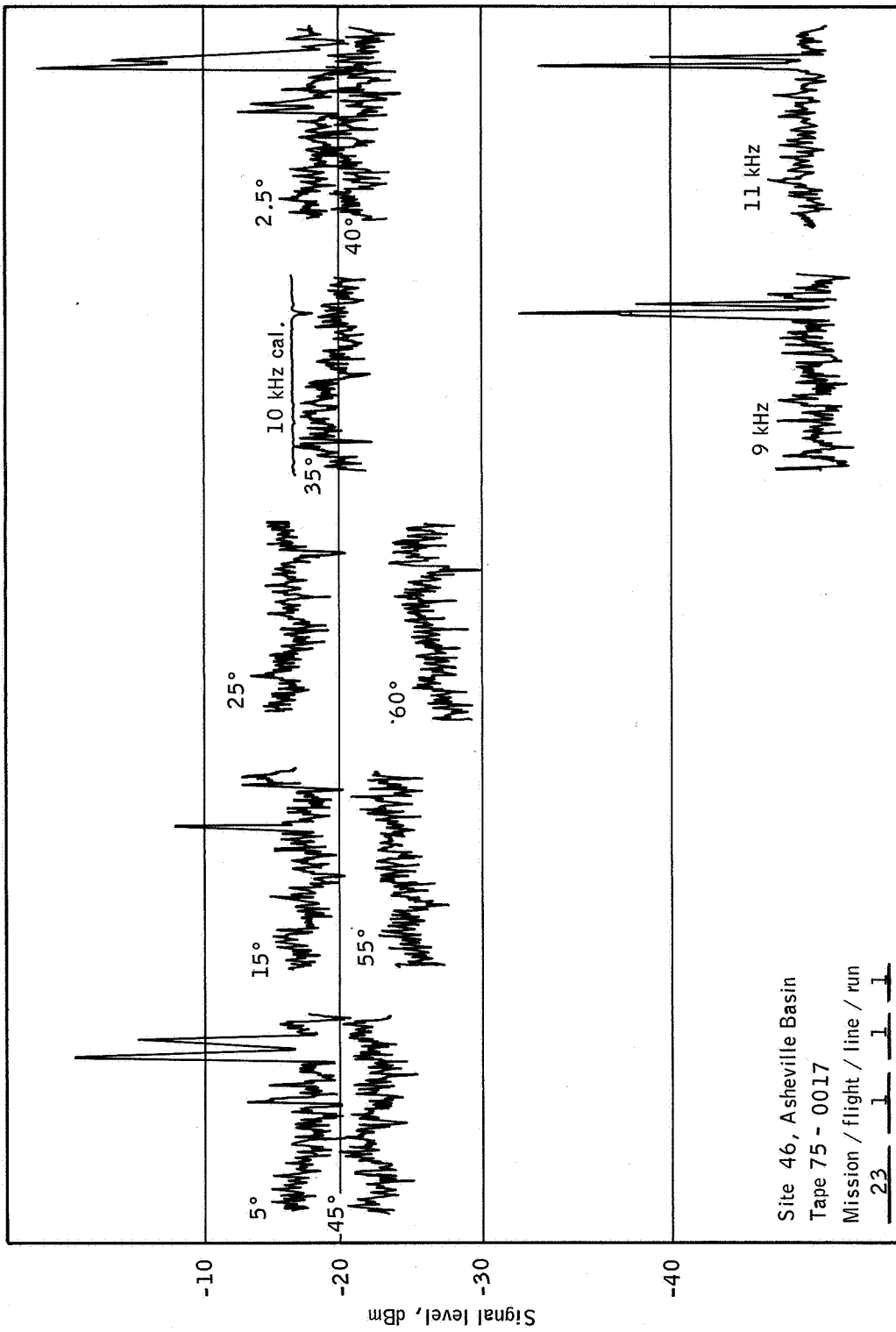
Tape 75 - 0017

Mission / flight / line / run

23 1 1 1

(d) The PSD curve.

Figure B-4.- Continued.



(e) Time history.

Figure B-4.- Concluded.

SET 5 — MISSION DATA

Mission/flight/line/run

23 1 1 2

Site 46, Asheville Basin, North Carolina

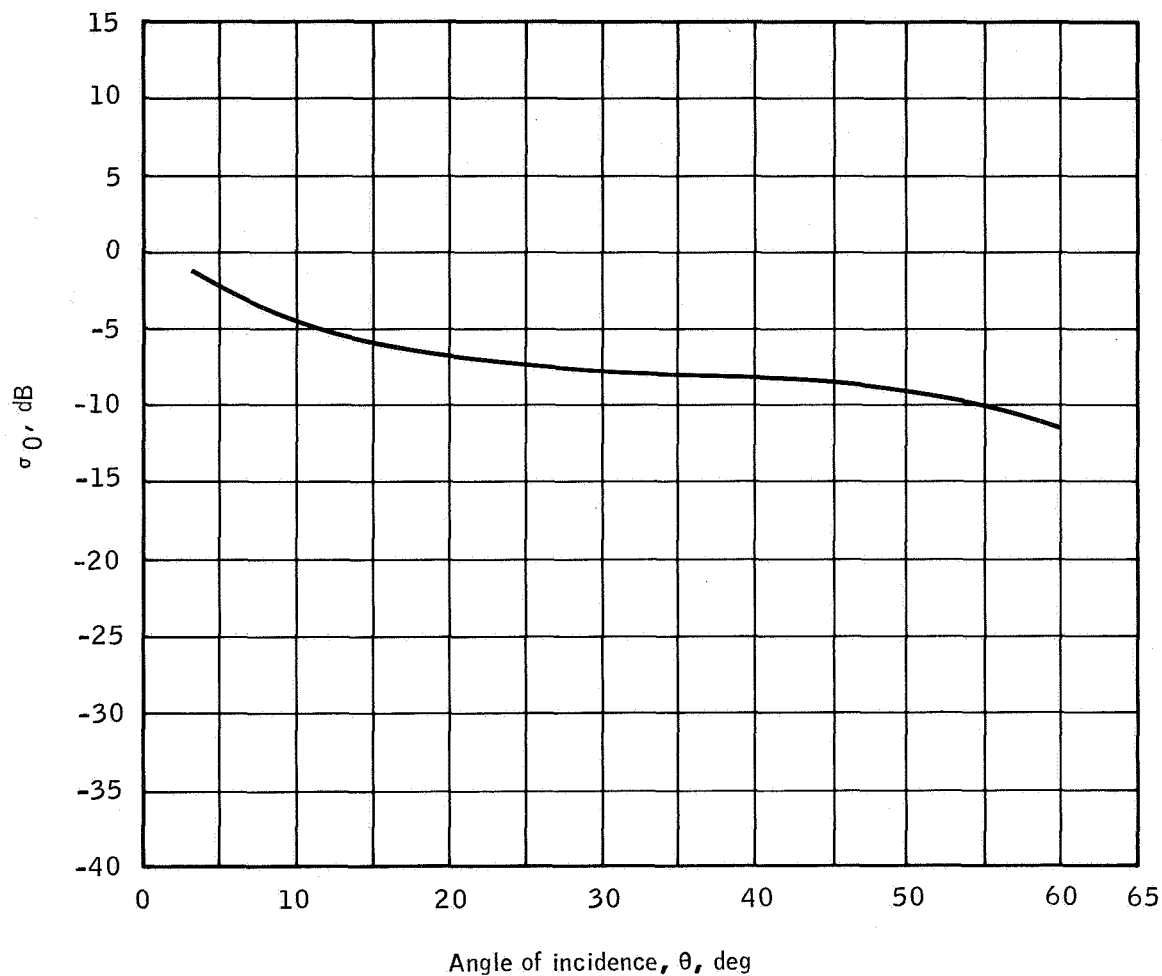
Altitude: 4200 feet

Time: 1148 e.s.t.

Infrared color film

These data samples were taken over a partially forested area along the southeastern end of line 1. The $\sigma_0(\theta)$ curve shown follows

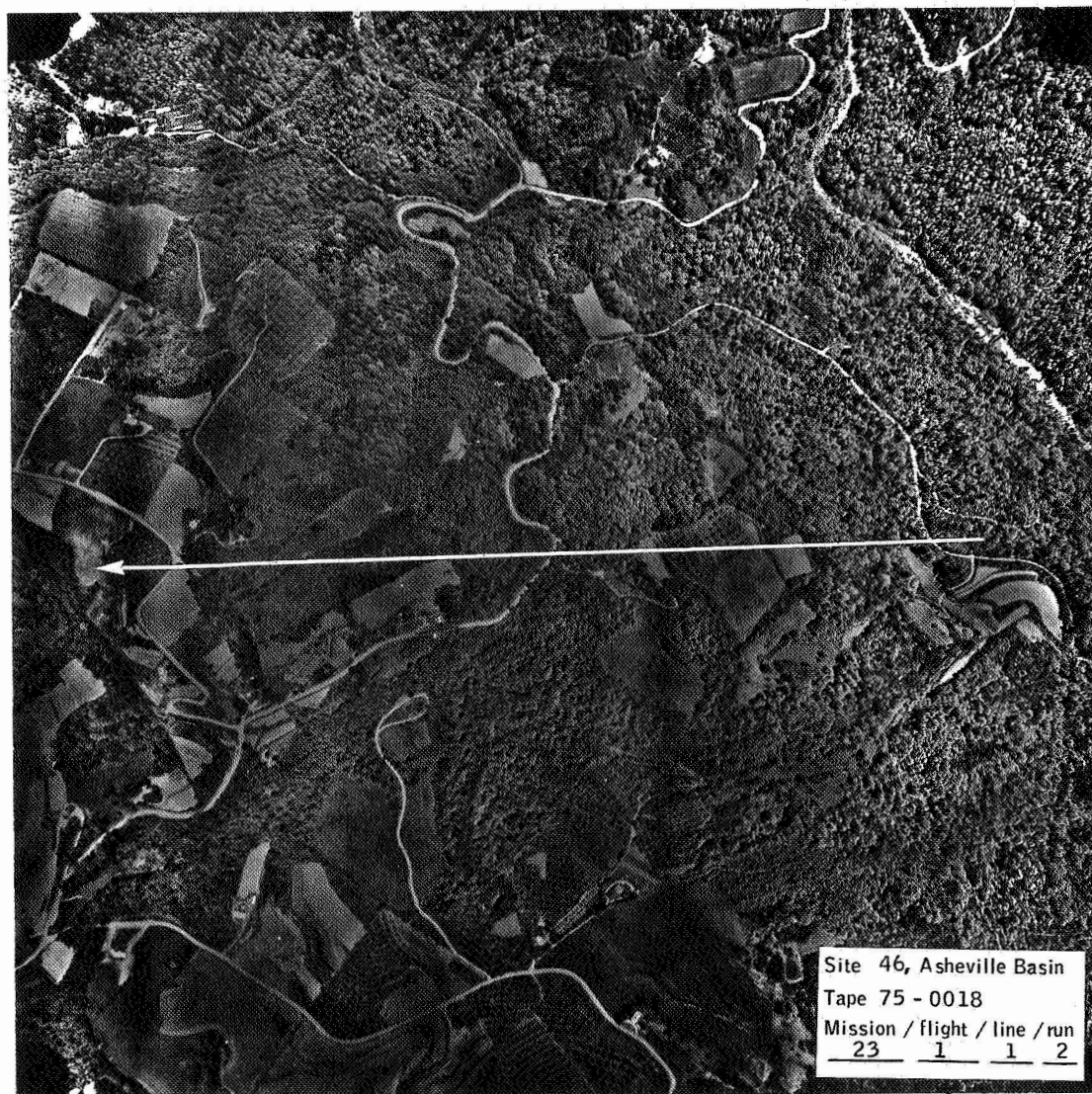
Newbry's heavy-vegetation curve (ref. 14), is approximately 2 dB higher than the rocky-hills data presented in reference 17, and is 5 dB higher than the curve for the New Jersey trees in reference 14.



Site 46, Asheville Basin σ_0 sample time
 Tape 75 - 0018 Hours / minutes / seconds
 Mission / flight / line / run 11 48 15
23 1 1 2 Through 11 48 45

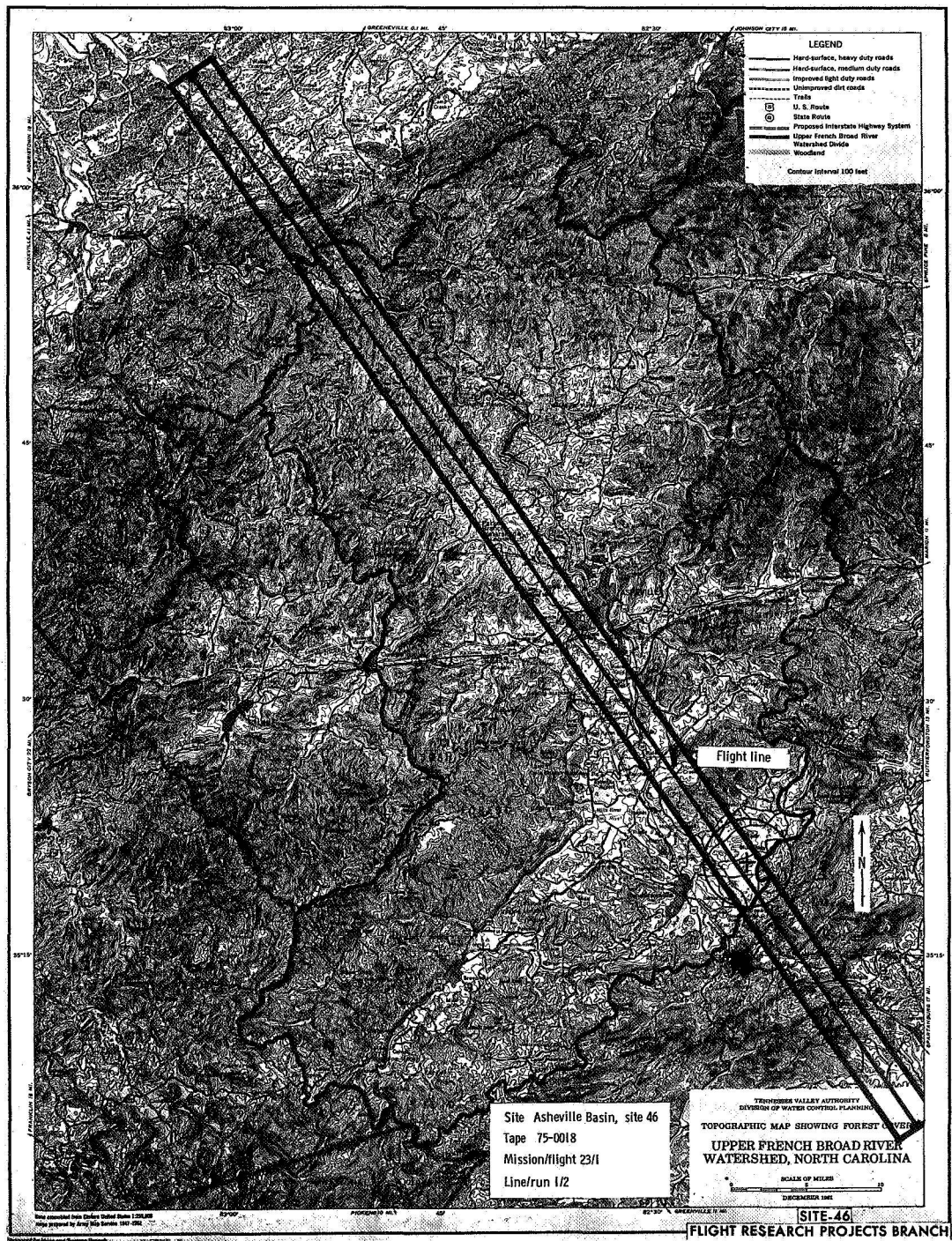
(a) The $\sigma_0(\theta)$ curve.

Figure B-5.- Set 5 data samples.



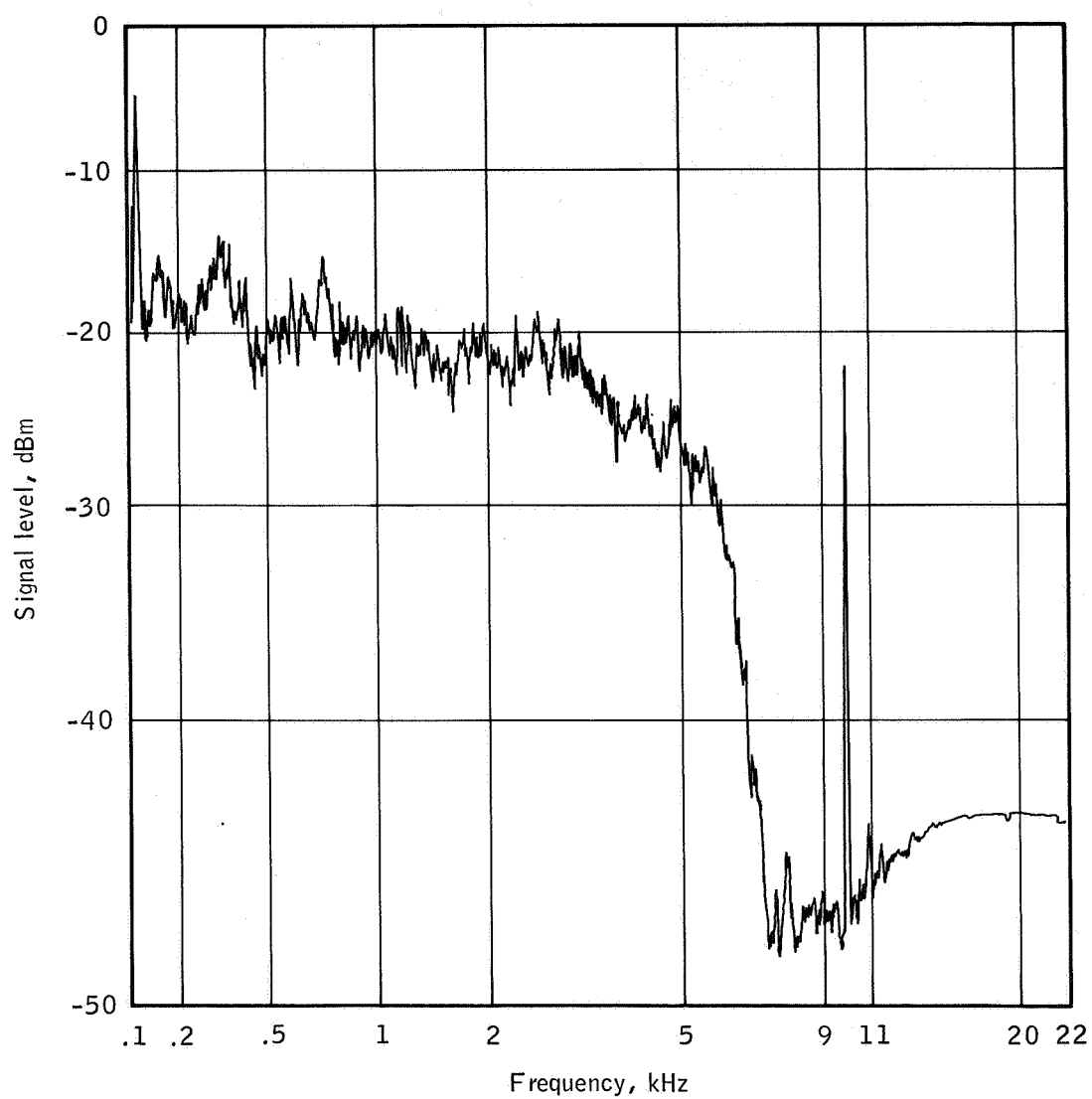
(b) Flight line.

Figure B-5.- Continued.



(c) Flight map.

Figure B-5.- Continued.



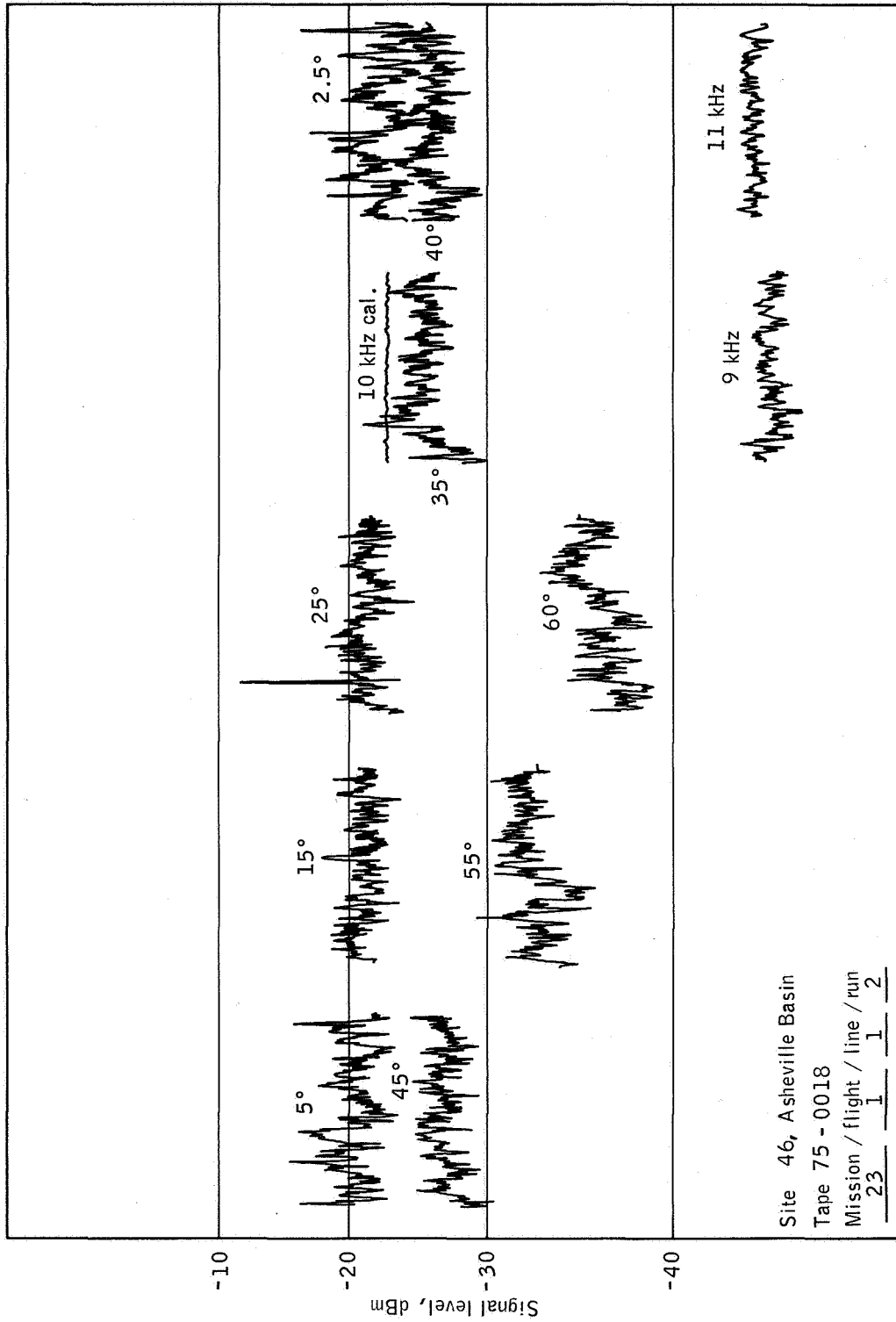
Site 46, Asheville Basin

Tape 75 - 0018

Mission / flight / line / run
23 1 1 2

(d) The PSD curve.

Figure B-5.- Continued.



(e) Time history.

Figure B-5.- Concluded.

SET 6 — MISSION DATA

Mission/flight/line/run

23 1 1 3

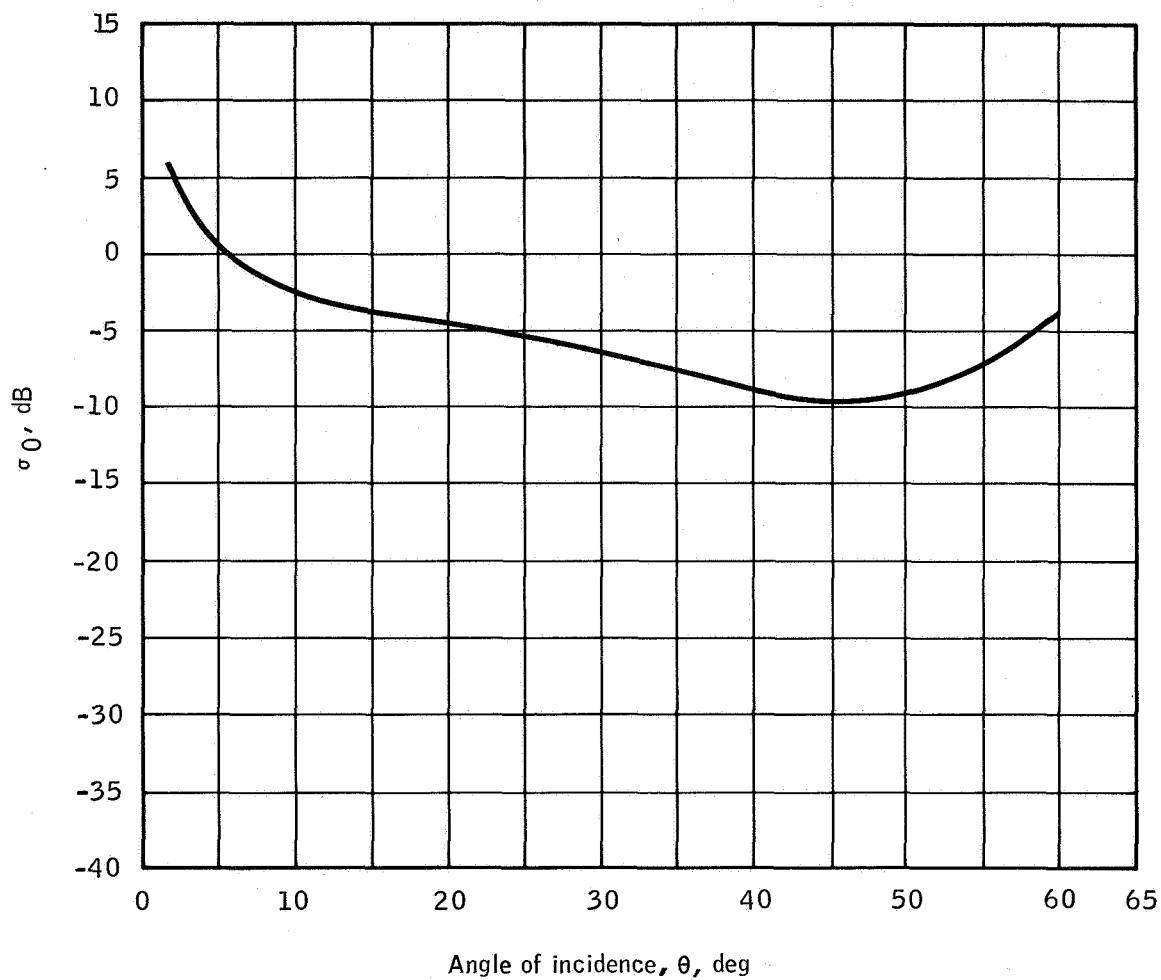
Site 46, Asheville Basin, North Carolina

Altitude: 15 000 feet

Time: 1239 e.s.t.

Infrared color film

Surface elevation varies considerably along this section of partially forested, partially cultivated terrain. The slope of the $\sigma_0(\theta)$ curve in the region of 10° to 45° is similar to the grazing-land curve in reference 17, although signal levels are approximately 7 dB higher; but this is believed to be only a "chance fit." Normally, data obtained from this altitude would not be considered reliable.



Site 46, Asheville Basin

σ_0 sample time

Tape 75 - 0019

Hours / minutes / seconds

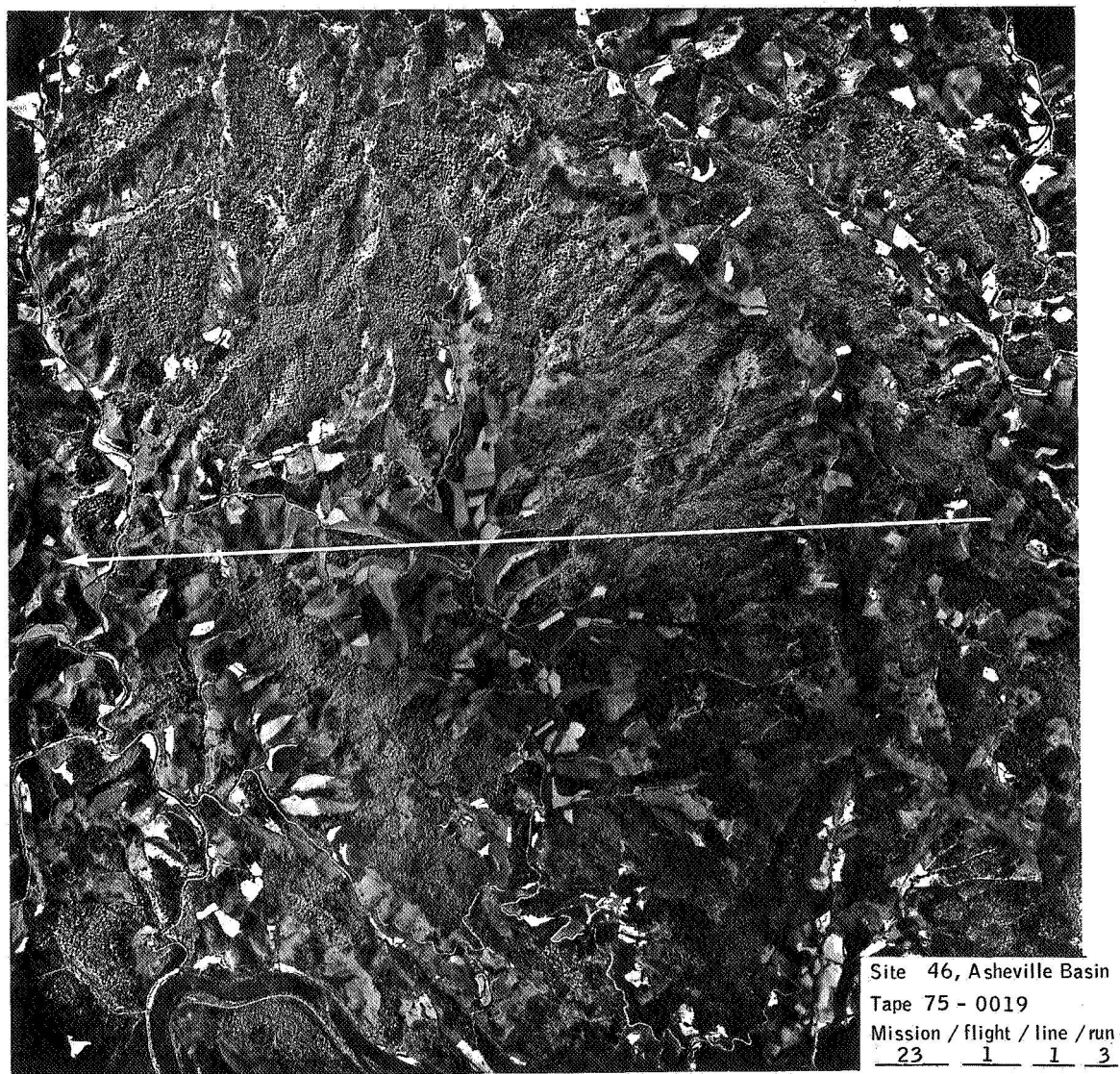
Mission / flight / line / run

23 1 1 3

Through 12 39 38

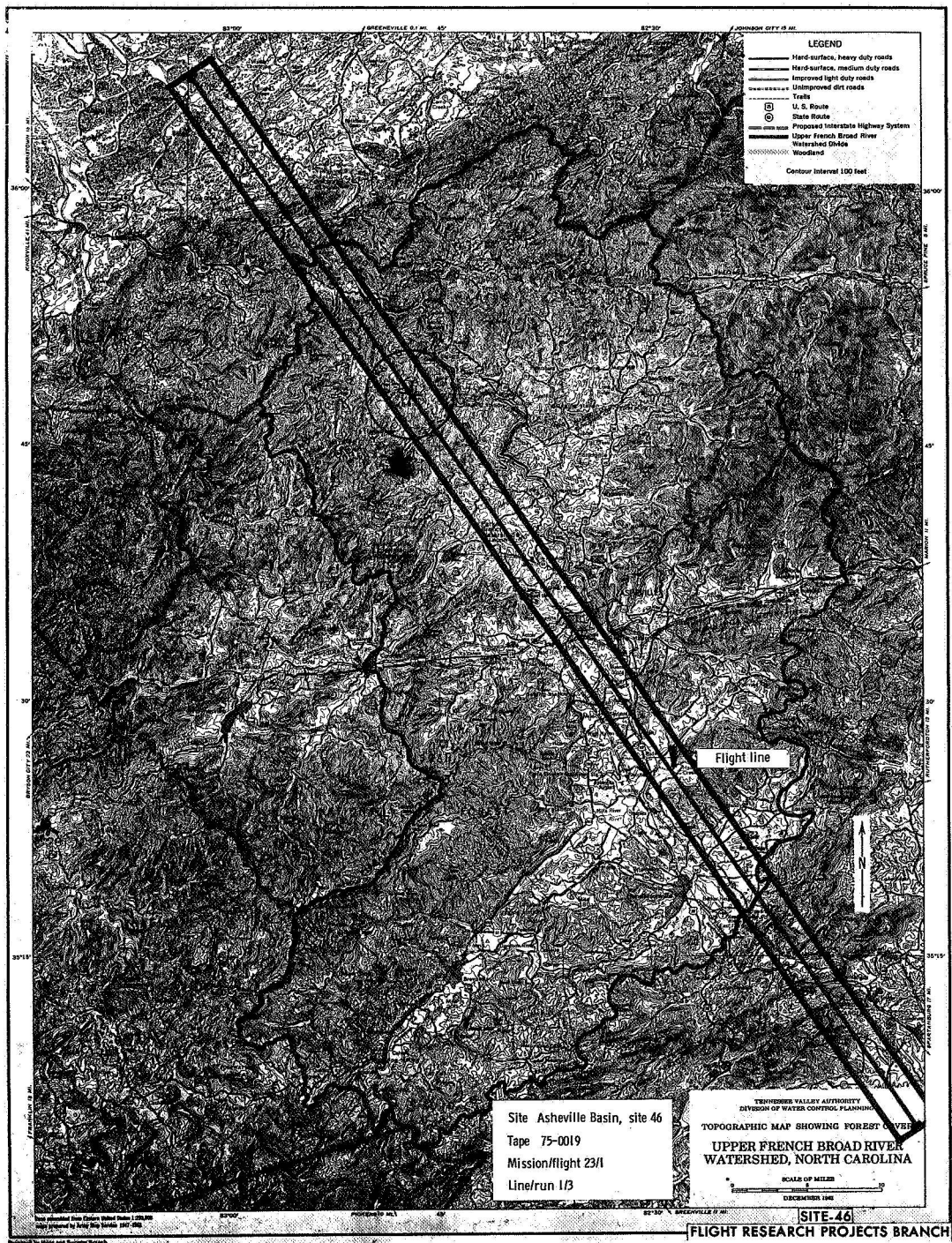
(a) The $\sigma_0(\theta)$ curve.

Figure B-6.- Set 6 data samples.



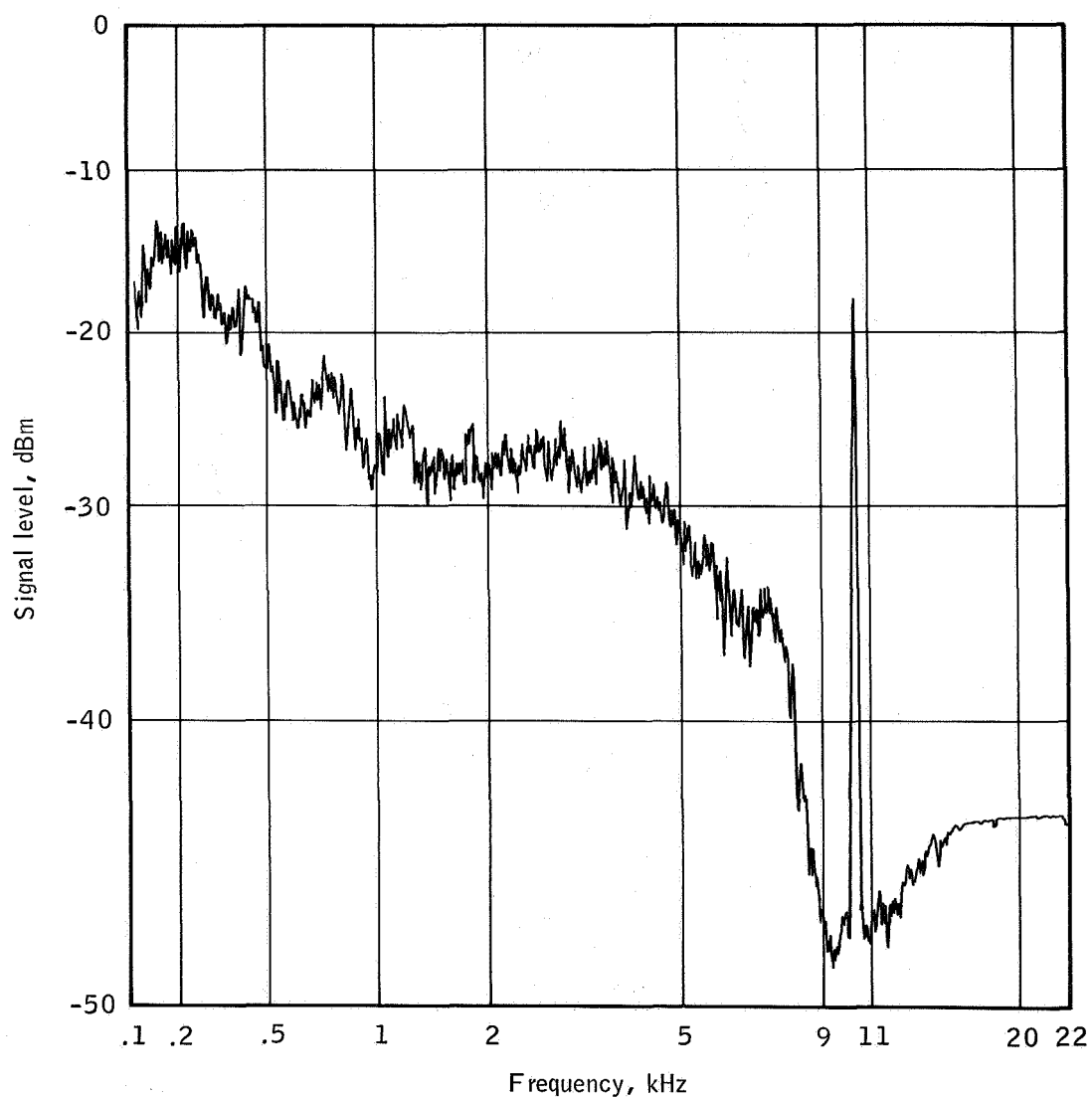
(b) Flight line.

Figure B-6.- Continued.



(c) Flight map.

Figure B-6.- Continued.



Site 46, Asheville Basin

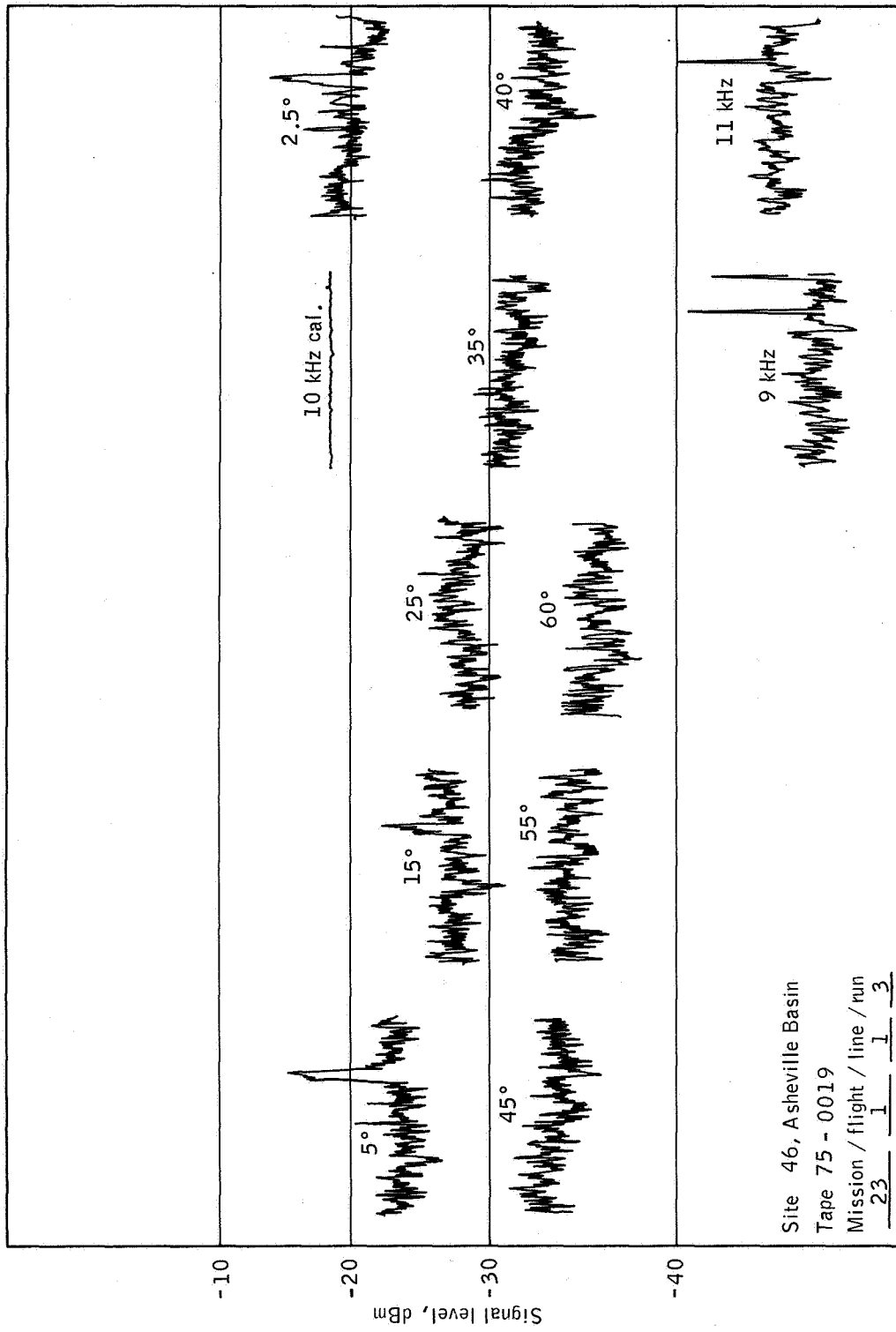
Tape 75 - 0019

Mission / flight / line / run

23 1 1 3

(d) The PSD curve.

Figure B-6.- Continued.



(e) Time history.

Figure B-6.- Concluded.

SET 7 — MISSION DATA

Mission/flight/line/run

23 1 1 4

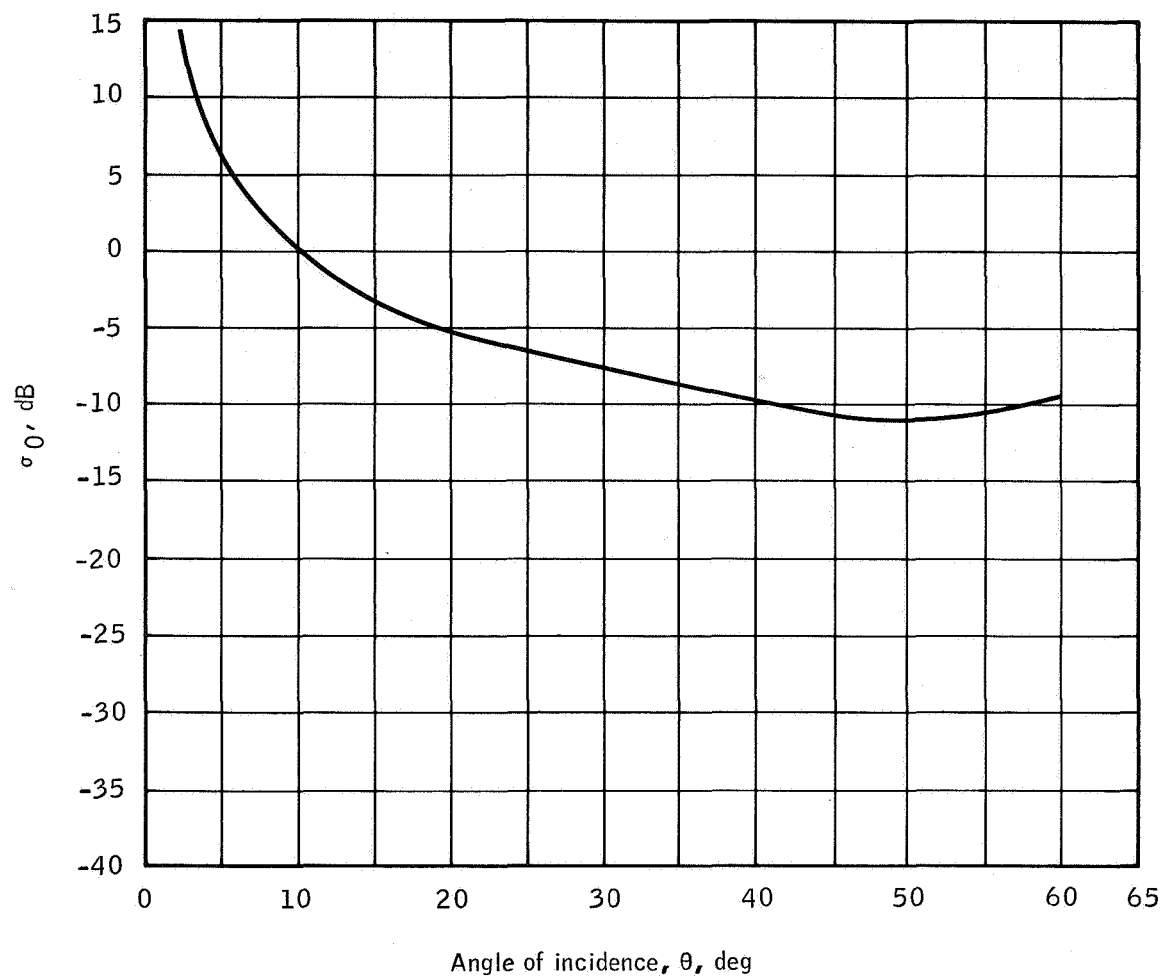
Site 46, Asheville Basin, North Carolina

Altitude: 15 000 feet

Time: 1310 e.s.t.

Ektachrome color film

These samples were taken over a suburban area near Asheville. The resultant $\sigma_0(\theta)$ curve does not appear to match any reference data and is considered unreliable because of the altitude.



Site 46 , Asheville Basin

Tape 75 - 0020

Mission / flight / line / run
23 1 1 4

σ_0 sample time

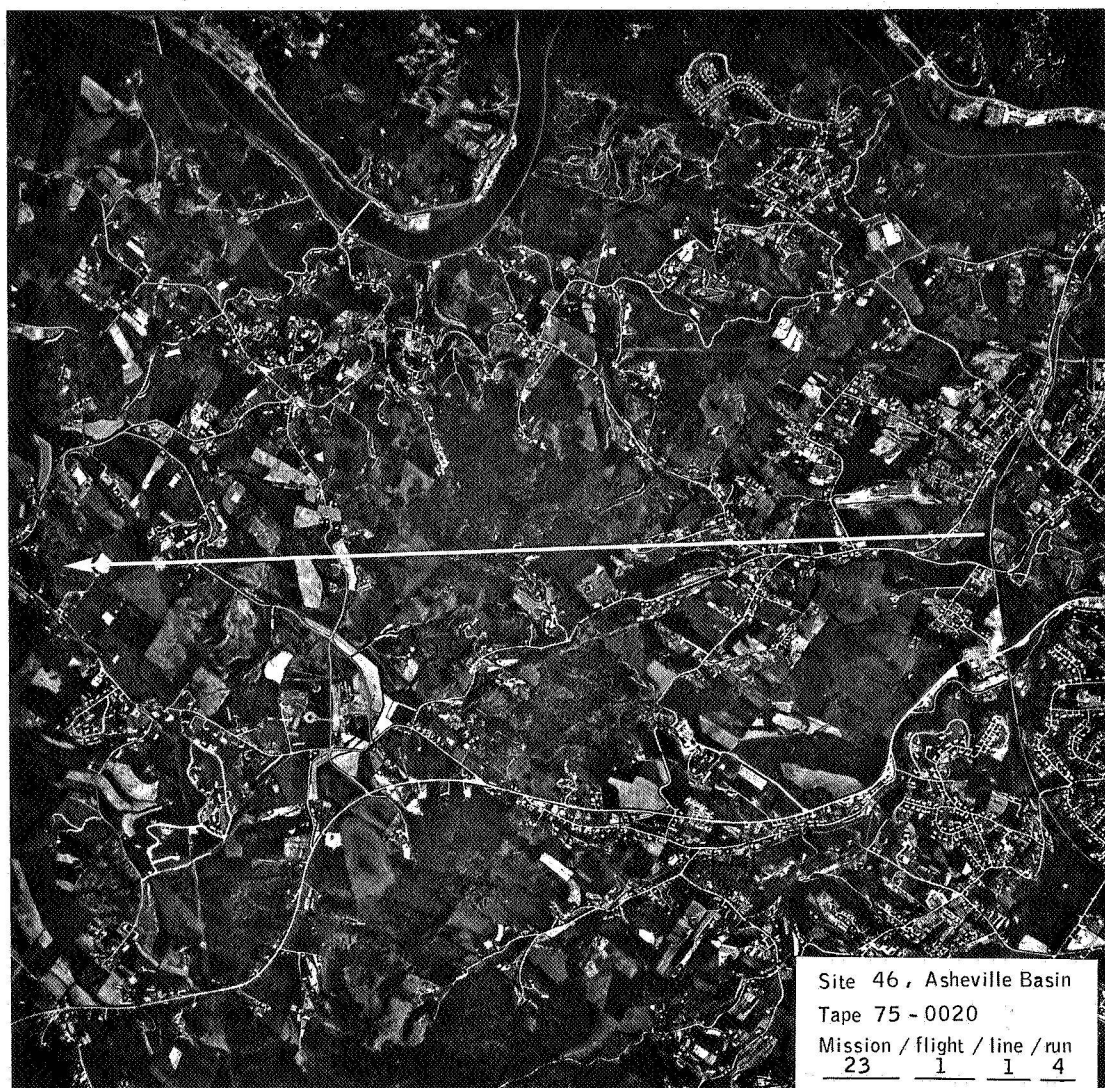
Hours / minutes / seconds

13 09 45

Through 13 10 15

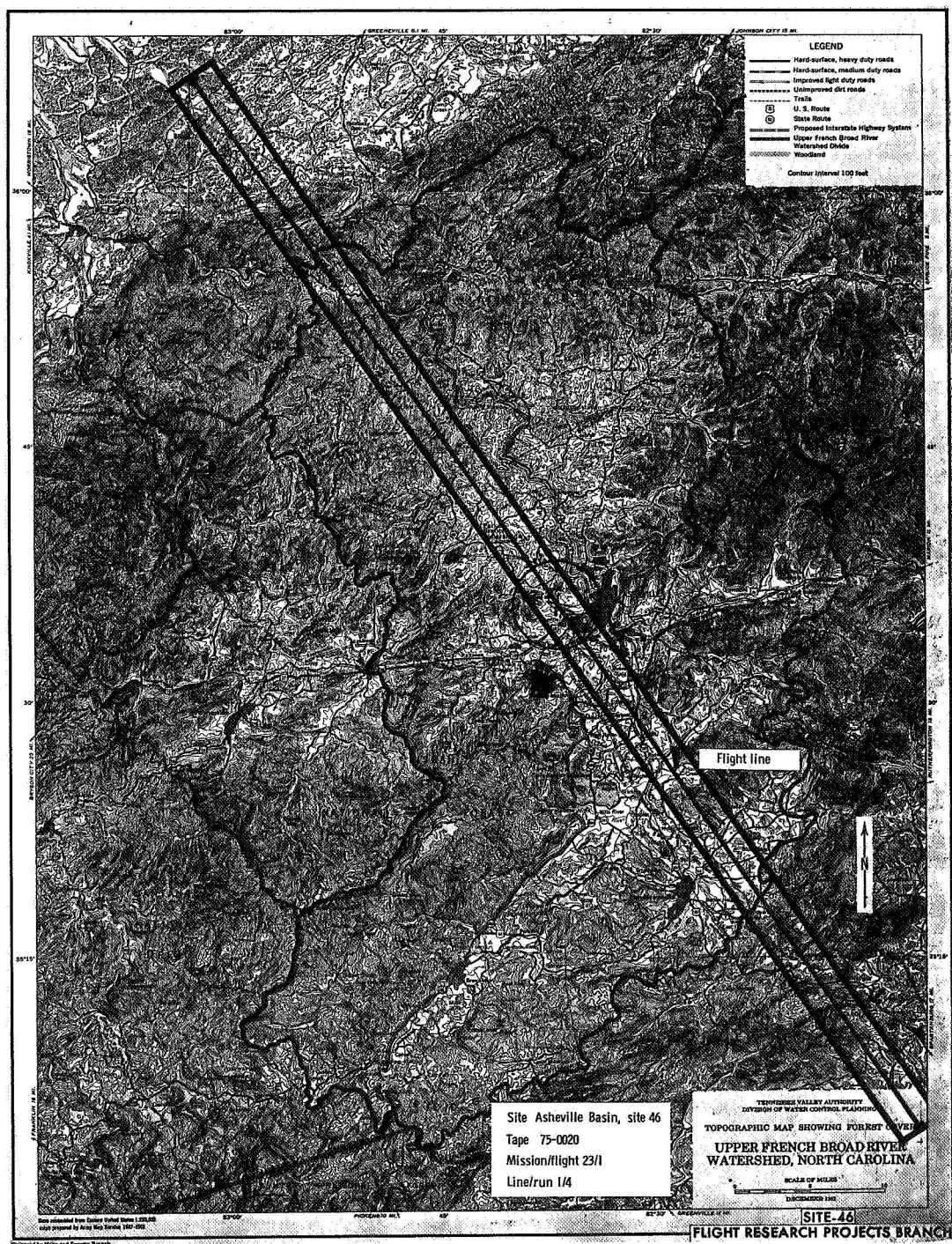
(a) The $\sigma_0(\theta)$ curve.

Figure B-7.- Set 7 data samples.



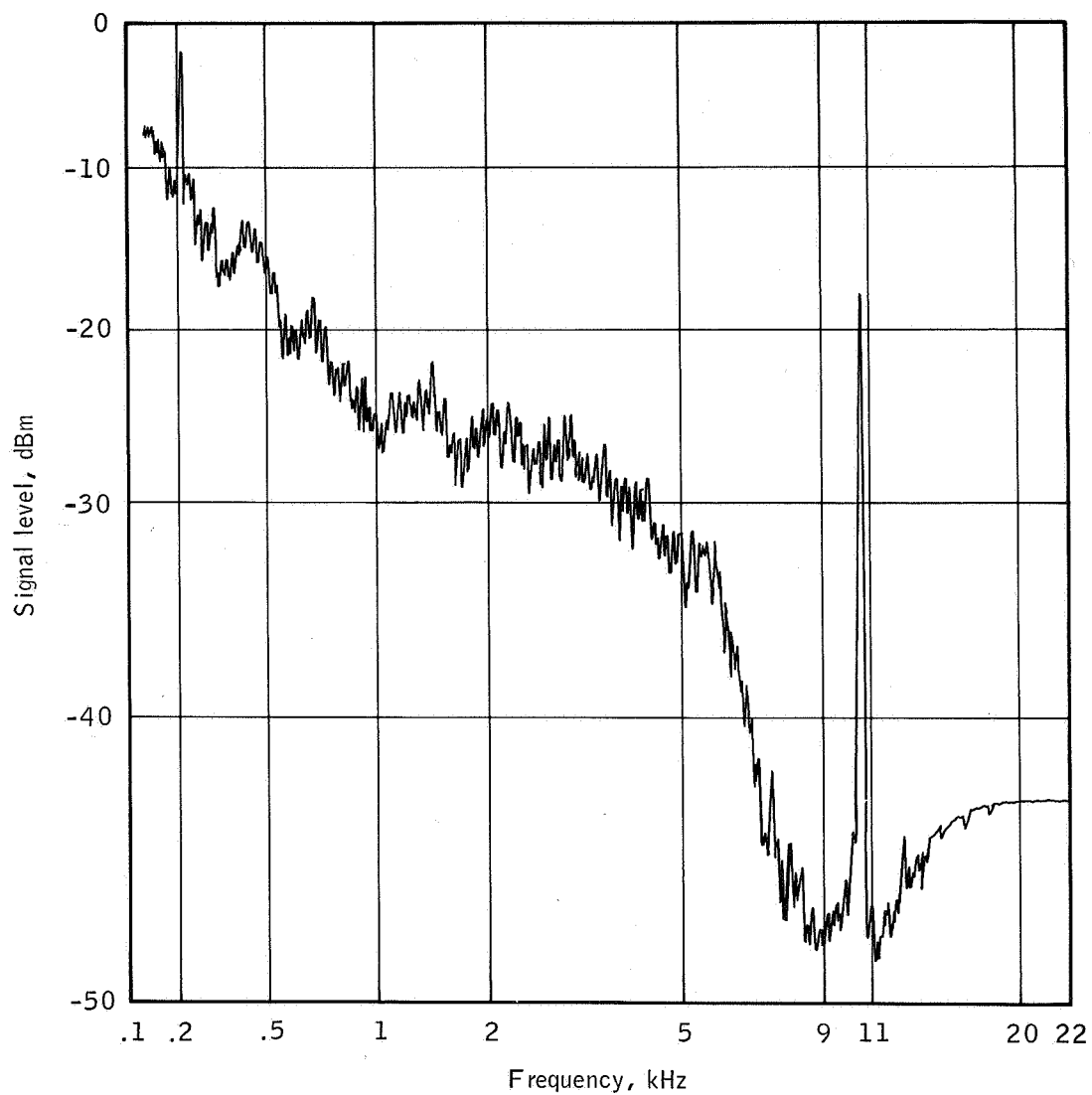
(b) Flight line.

Figure B-7.- Continued.



(c) Flight map.

Figure B-7.- Continued.



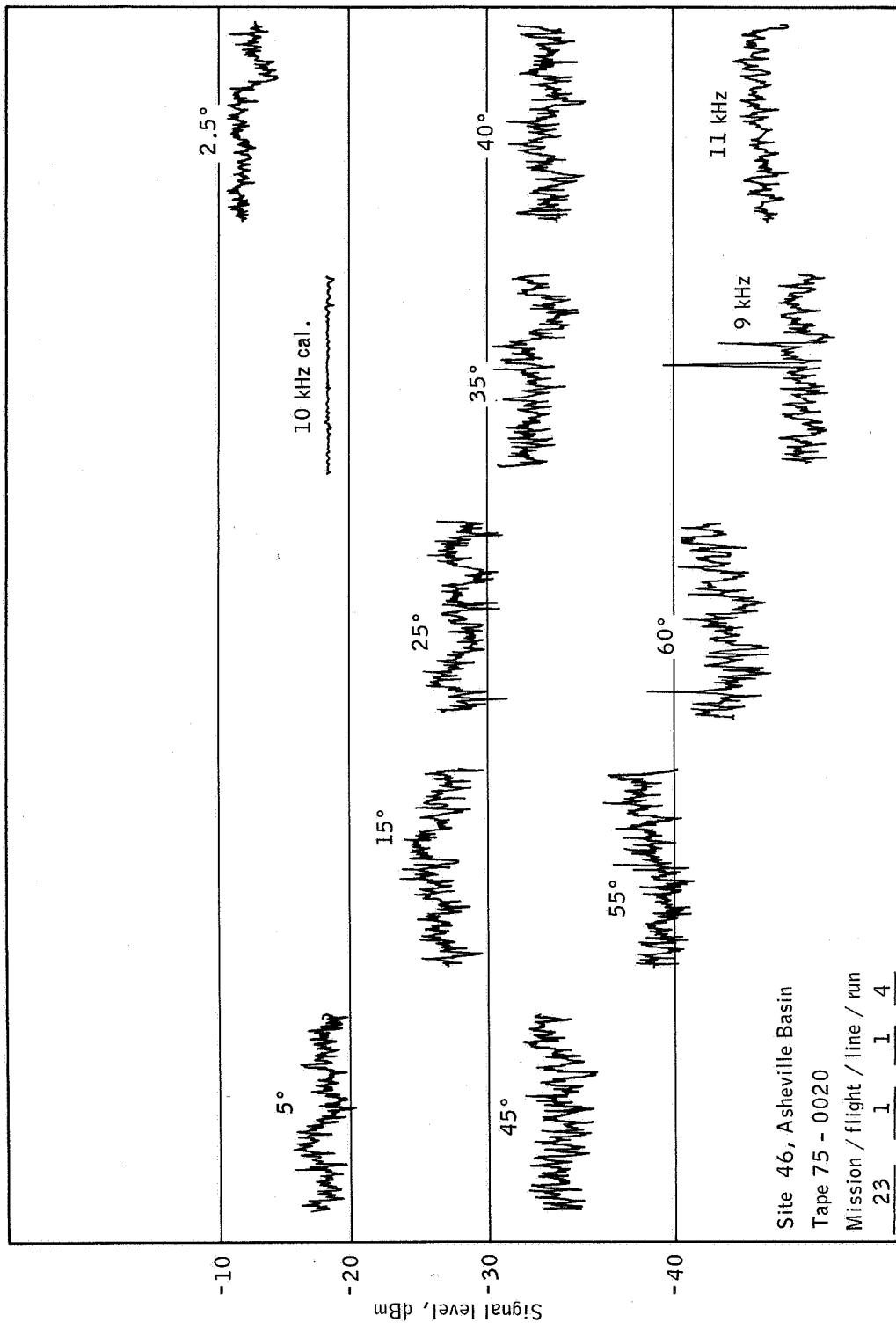
Site 46 , Asheville Basin

Tape 75 - 0020

Mission / flight / line / run
<u>23</u> <u>1</u> <u>1</u> <u>4</u>

(d) The PSD curve.

Figure B-7.- Continued.



(e) Time history.

Figure B-7.- Concluded.

SET 8 — MISSION DATA

Mission/flight/line/run

32 1 4 1

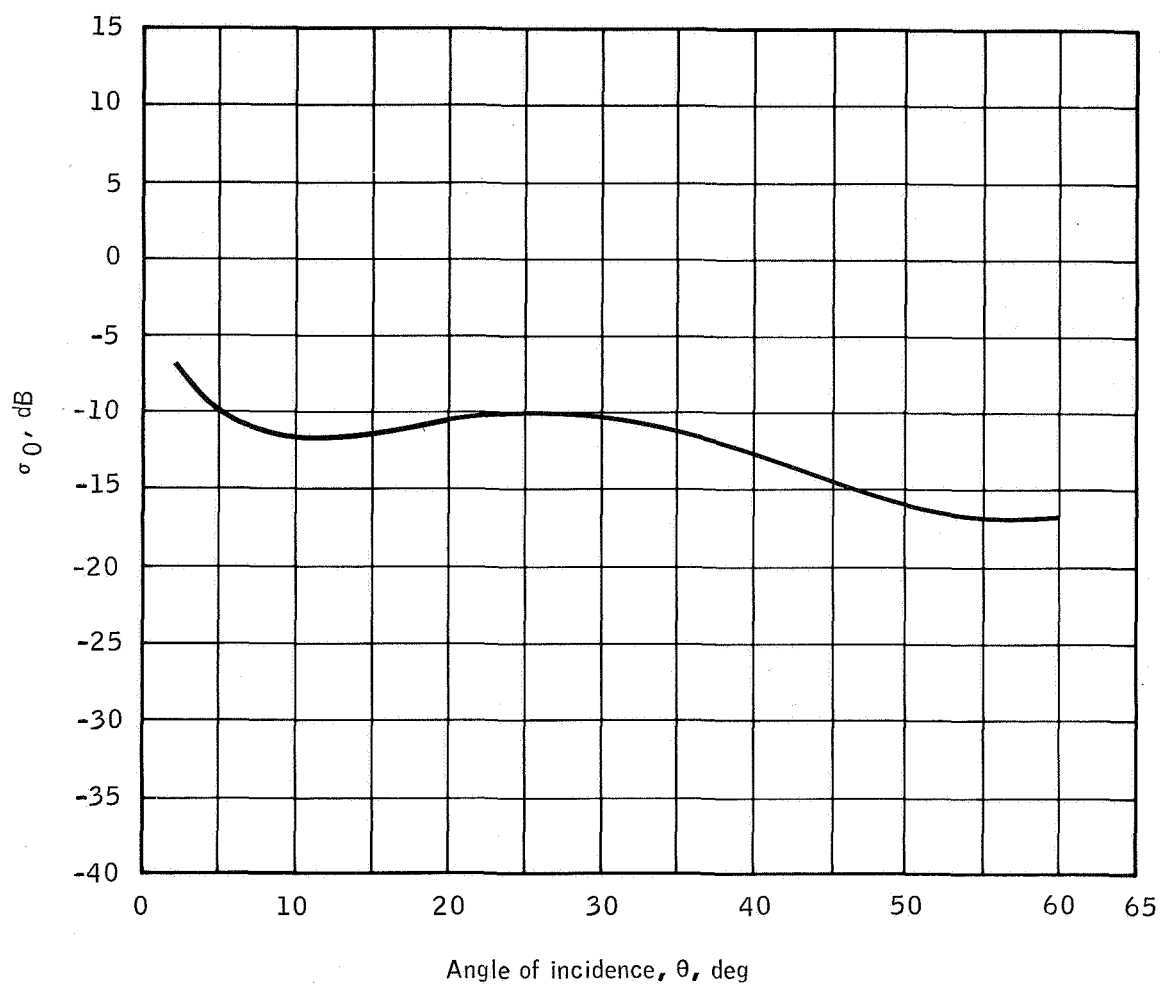
Site 76, Garden City, Kansas

Altitude: 3000 feet

Time: 1430 c.s.t.

Ektachrome color film

The $\sigma_0(\theta)$ curve shown in this section is plotted from data obtained over Kansas grain fields near the northern end of line 4 and shows a marked increase in the signal level starting at 20° -incidence angle. This may be correlated with the change in crop type and height (shown in the accompanying photograph). The data points shown are comparable with reference data contained in references 14 and 17.



Site 76, Garden City

Tape 75 - 0079

Mission / flight / line / run

32 1 4 1

σ_0 sample time

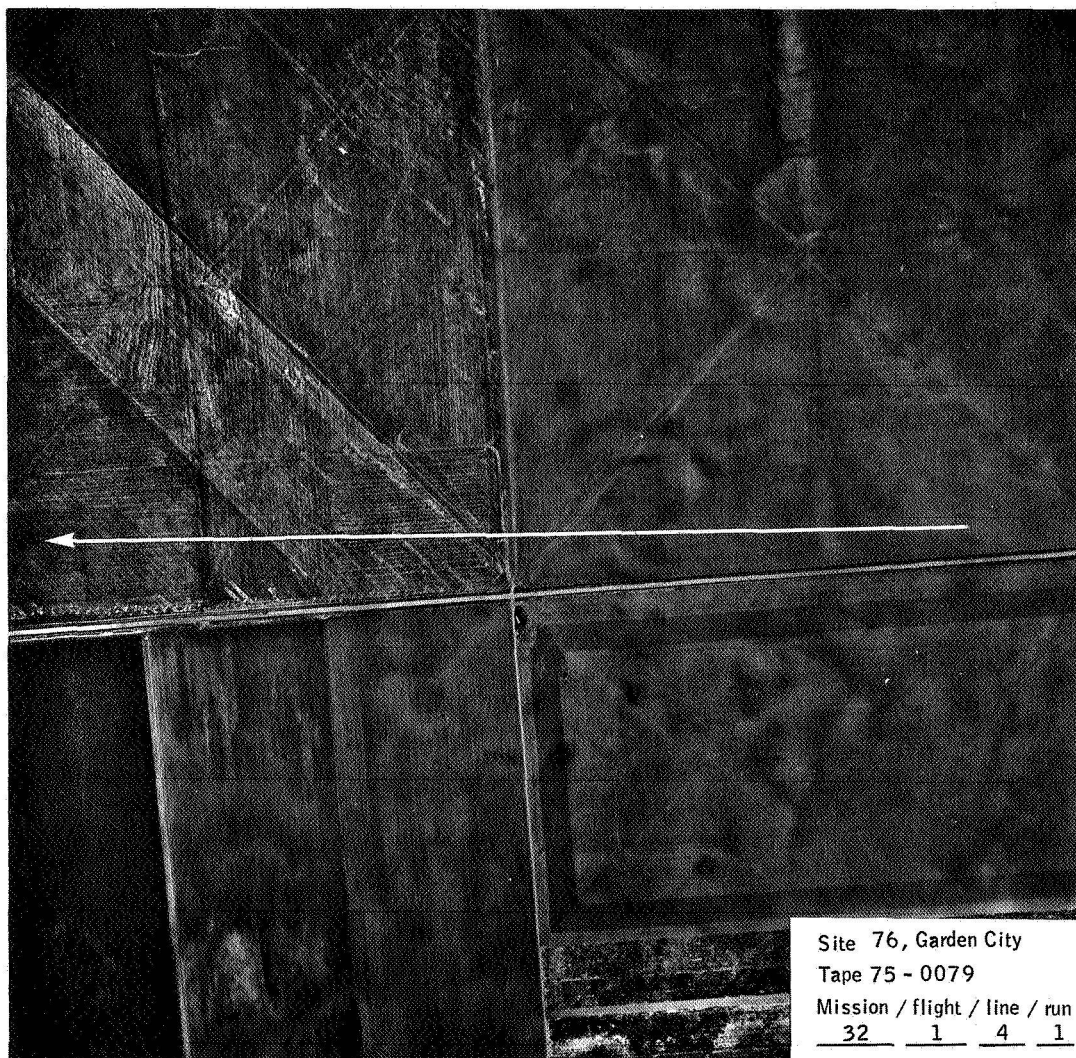
Hours / minutes / seconds

14 30 08

Through 14 30 23

(a) The $\sigma_0(\theta)$ curve.

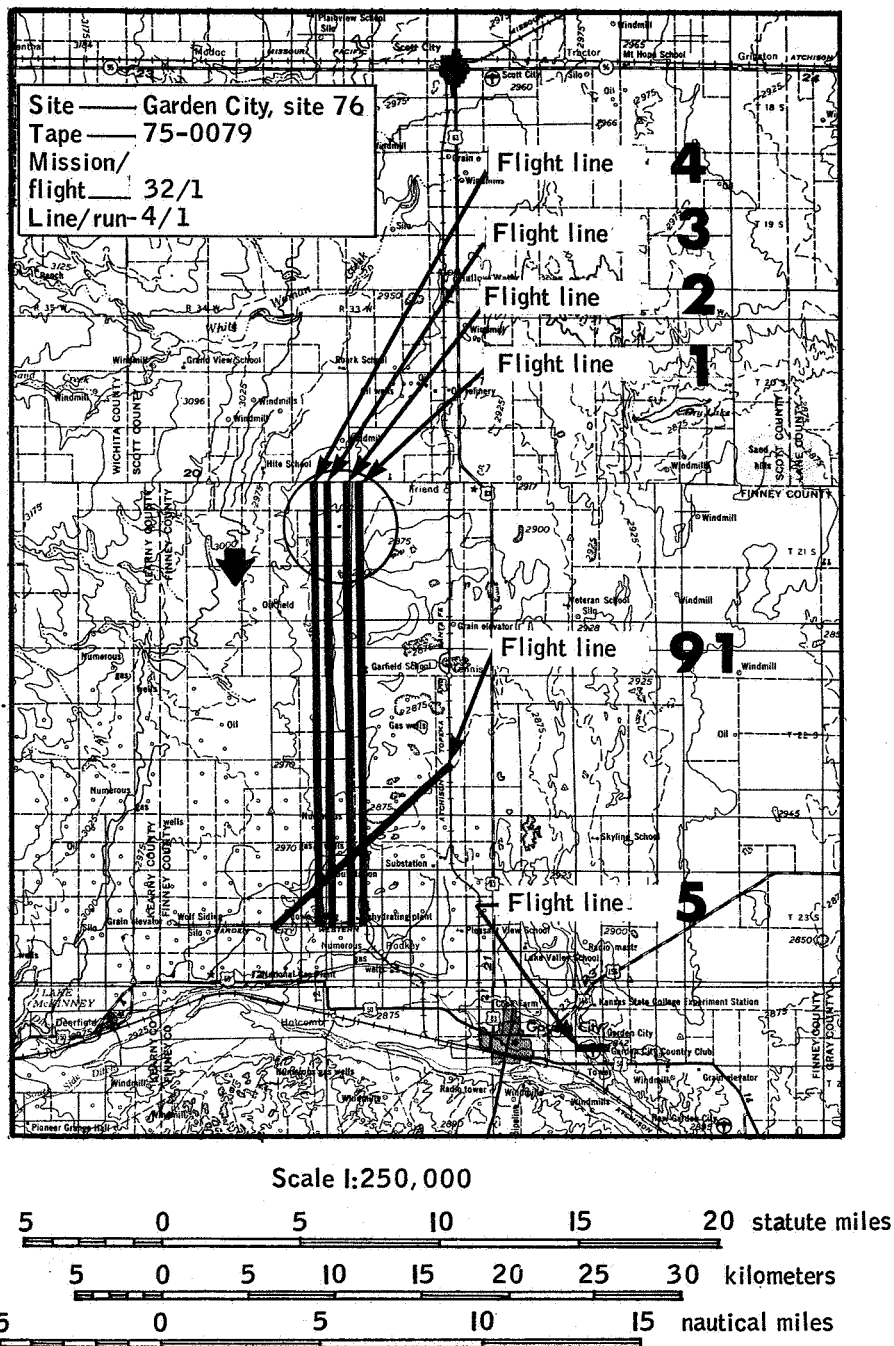
Figure B-8.- Set 8 data samples.



Site 76, Garden City
Tape 75 - 0079
Mission / flight / line / run
32 1 4 1

(b) Flight line.

Figure B-8.- Continued.

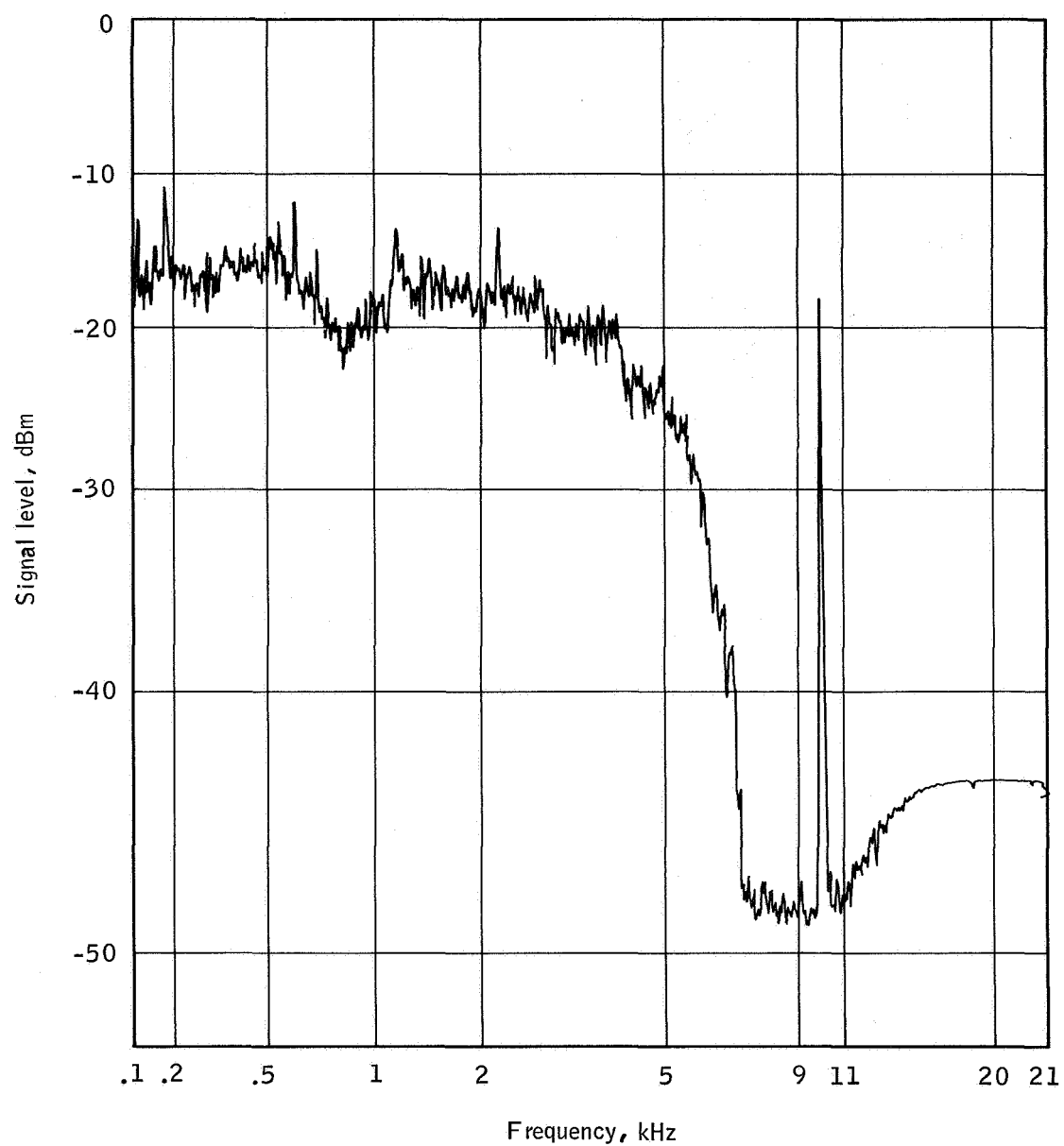


Contour interval 50 feet with supplementary contours at 25 foot intervals

Transverse mercator projection

(c) Flight map.

Figure B-8.— Continued.



Site 76, Garden City

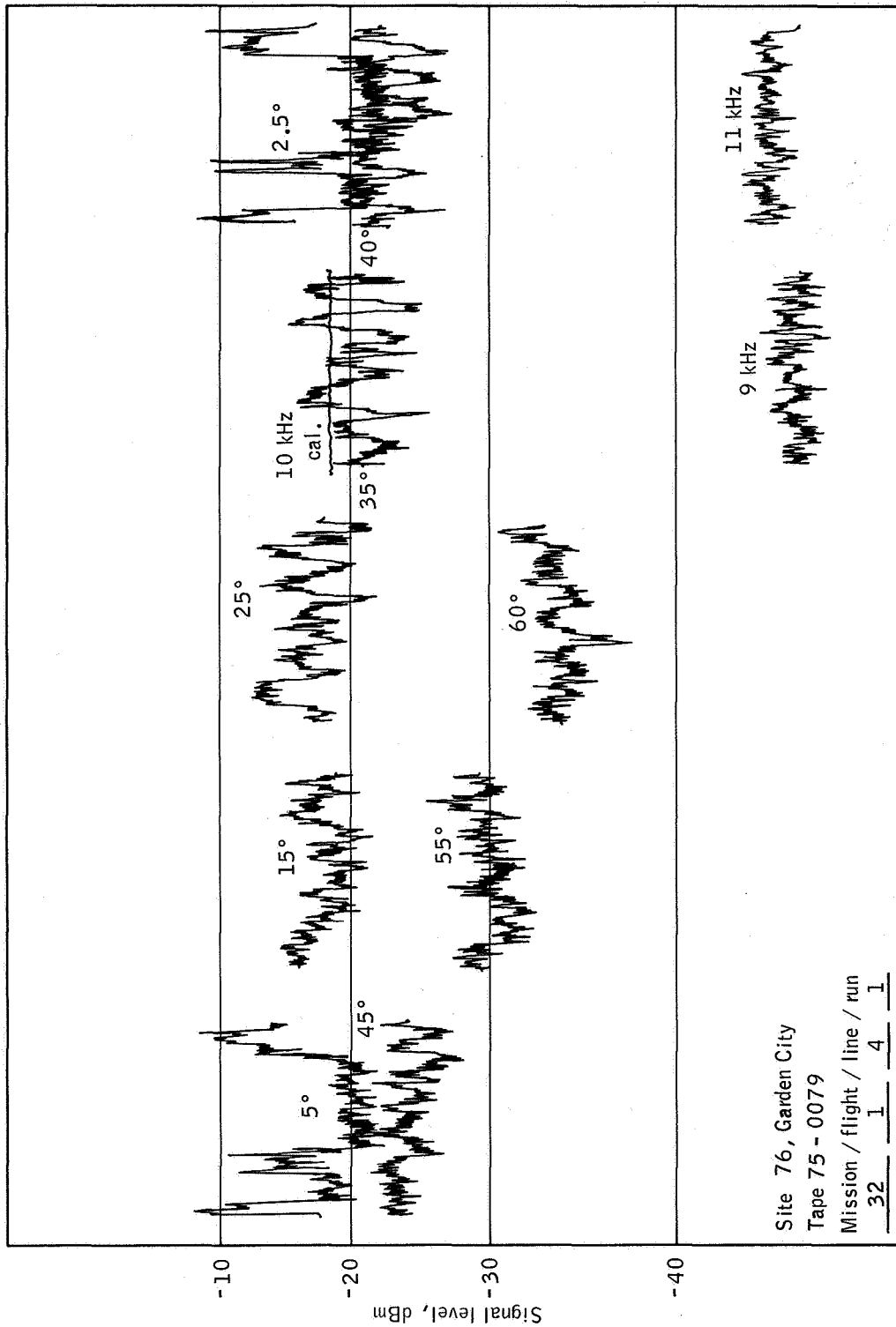
Tape 75 - 0079

Mission / flight / line / run

32 1 4 1

(d) The PSD curve.

Figure B-8.- Continued.



(e) Time history.

Figure B-8.- Concluded.

SET 9 — MISSION DATA

Mission/flight/line/run

32 1 3 1

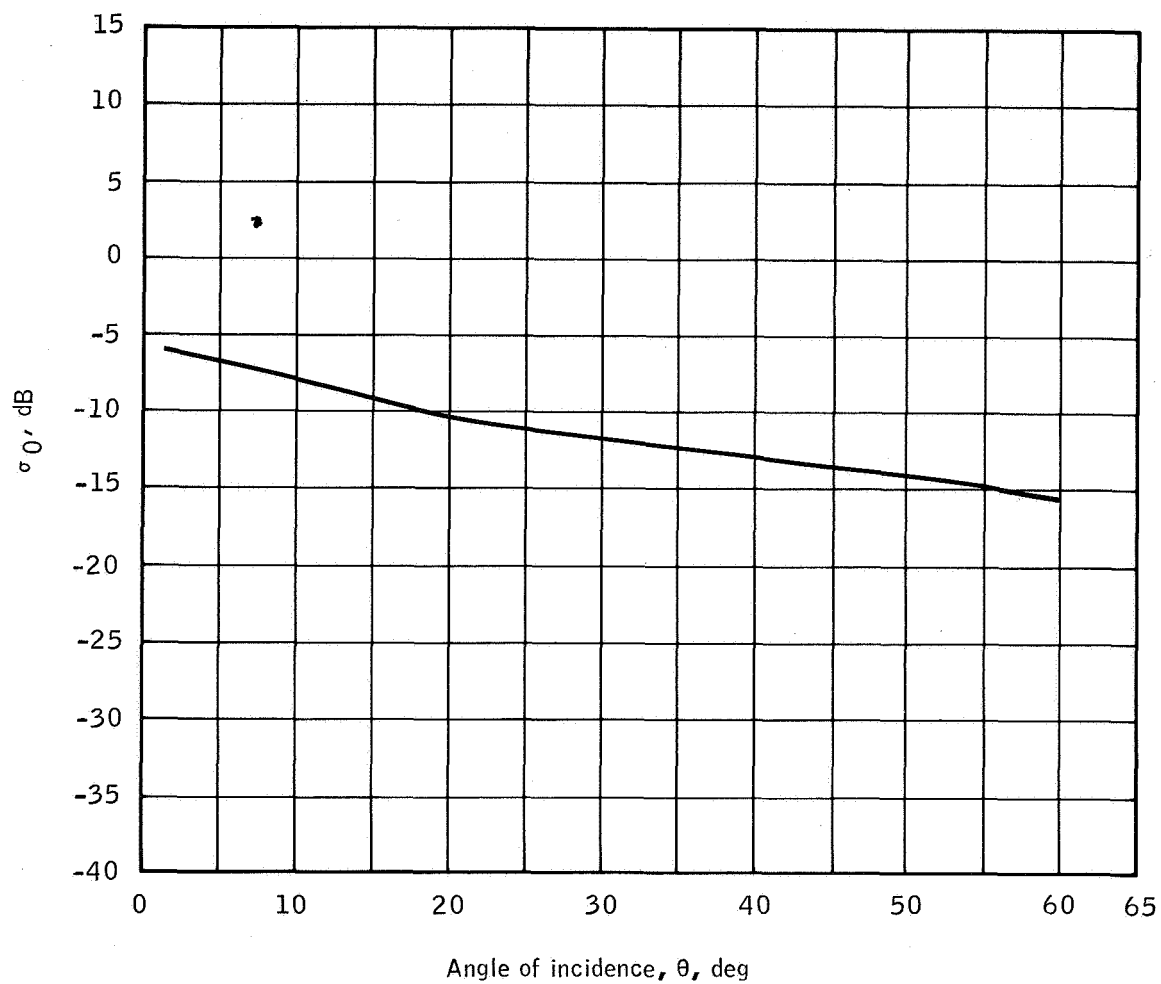
Site 76, Garden City, Kansas

Altitude: 3000 feet

Time: 1453 c.s.t.

Ektachrome color film

These samples were taken over the northern end of line 3 adjacent to line 4. The $\sigma_0(\theta)$ curve is characteristic of this type of cropland and compares well with signal level values shown in the line 4 sample in the region of 25° to 60° . Crop type in the radar-illuminated area is more homogeneous, thus yielding a substantially smoother curve.



Site 76, Garden City	σ_0 sample time
Tape 75 - 0080	Hours / minutes / seconds
Mission / flight / line / run	<u>14</u> <u>52</u> <u>55</u>
<u>32</u> <u>1</u> <u>3</u> <u>1</u>	Through <u>14</u> <u>53</u> <u>10</u>

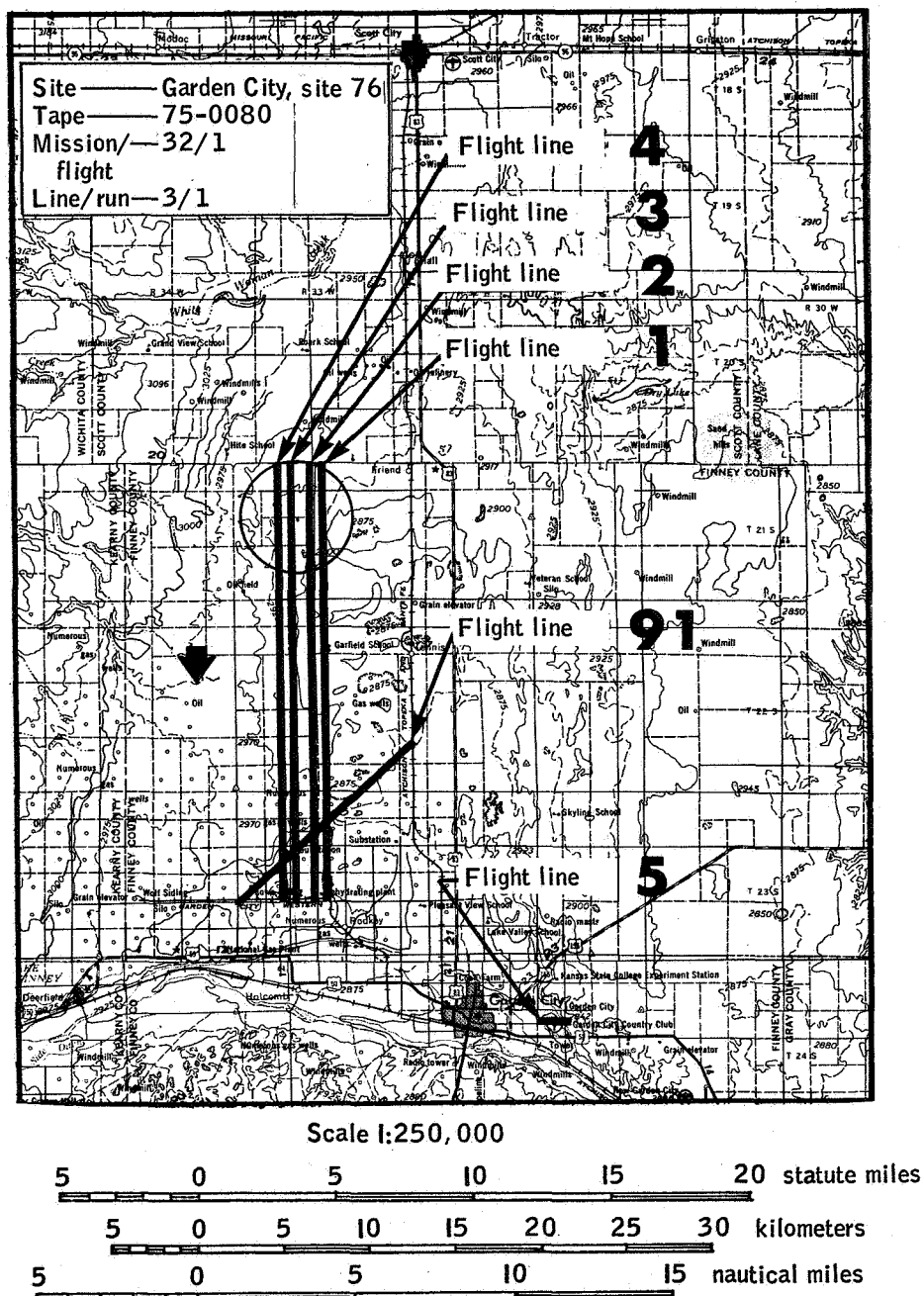
(a) The $\sigma_0(\theta)$ curve.

Figure B-9.- Set 9 data samples.



(b) Flight line.

Figure B-9.- Continued.

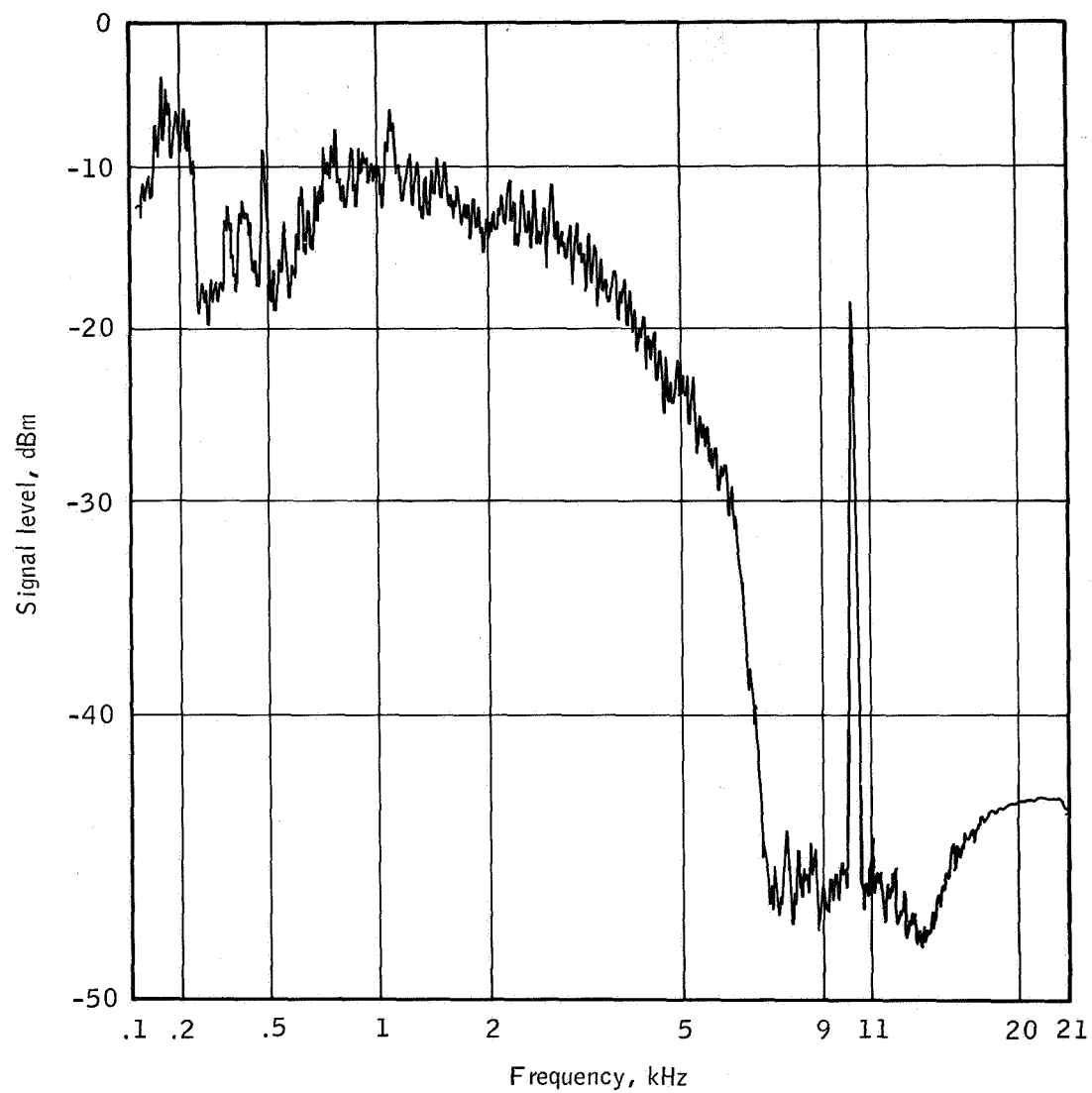


Contour interval 50 feet with supplementary contours at 25 foot intervals

Transverse mercator projection

(c) Flight map.

Figure B-9.- Continued.



Site 76, Garden City

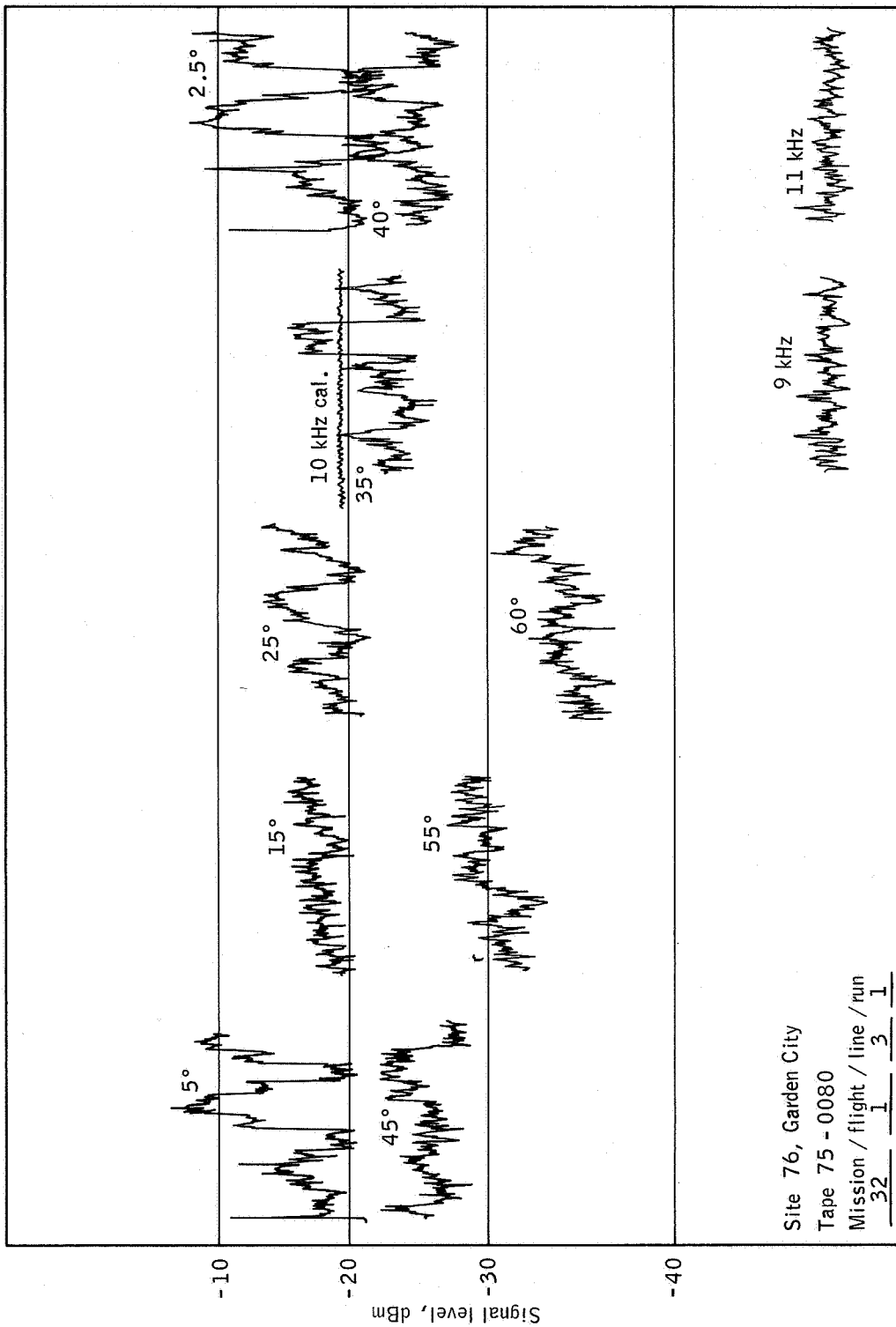
Tape 75 - 0080

Mission / flight / line / run

32 1 3 1

(d) The PSD curve.

Figure B-9.- Continued.



(e) Time history.

Figure B-9.- Concluded.

SET 10 — MISSION DATA

Mission/flight/line/run

32 2 5 1

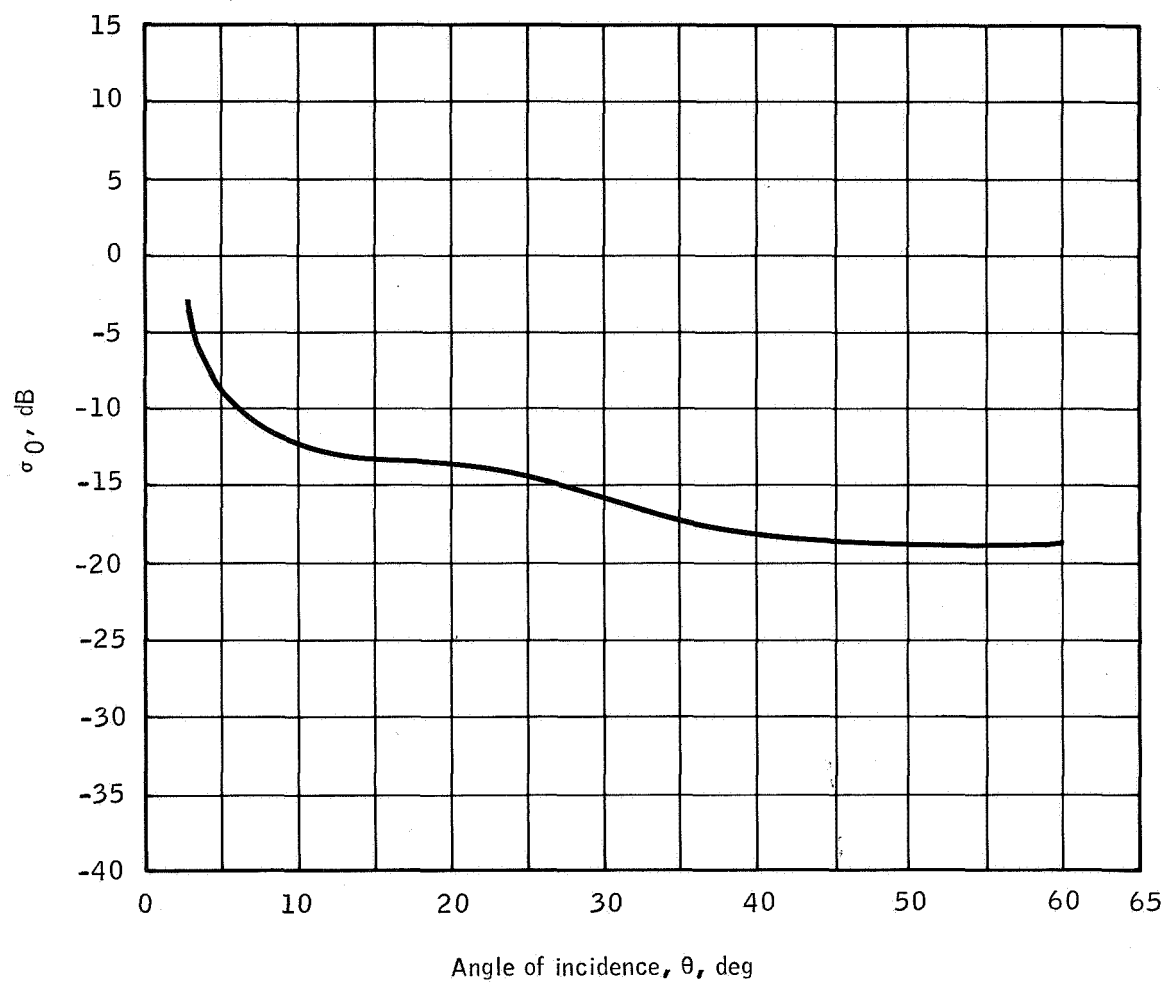
Site 11, Yellowstone National Park

Altitude: 7500 feet

Time: 1105 m.s.t.

Ektachrome color film

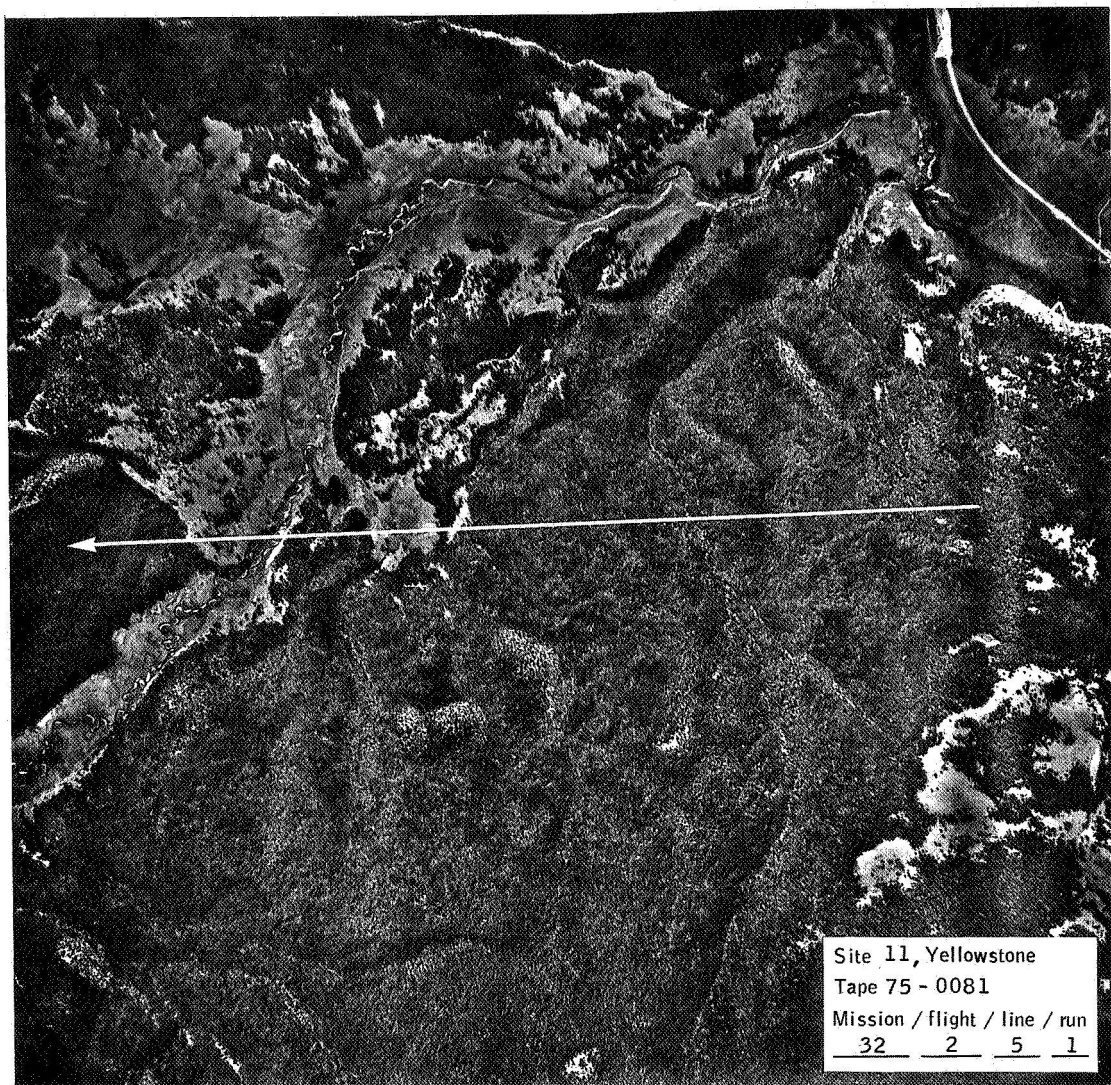
The terrain shown in the photograph in this section is located near the Gallatin River area at the western end of line 5. The area is partially forested with a change in tree type as shown in the upper half of the photograph. The $\sigma_0(\theta)$ curve is substantially lower in signal level as compared to reference values for forested terrain (refs. 14 and 17) and approximately 5 dB higher than values given for brushland (ref. 17).



Site 11, Yellowstone	σ_0 sample time
Tape 75 - 0081	Hours / minutes / seconds
Mission / flight / line / run	<u>11</u> <u>05</u> <u>20</u>
<u>32</u> <u>2</u> <u>5</u> <u>1</u>	Through <u>11</u> <u>05</u> <u>50</u>

(a) The $\sigma_0(\theta)$ curve.

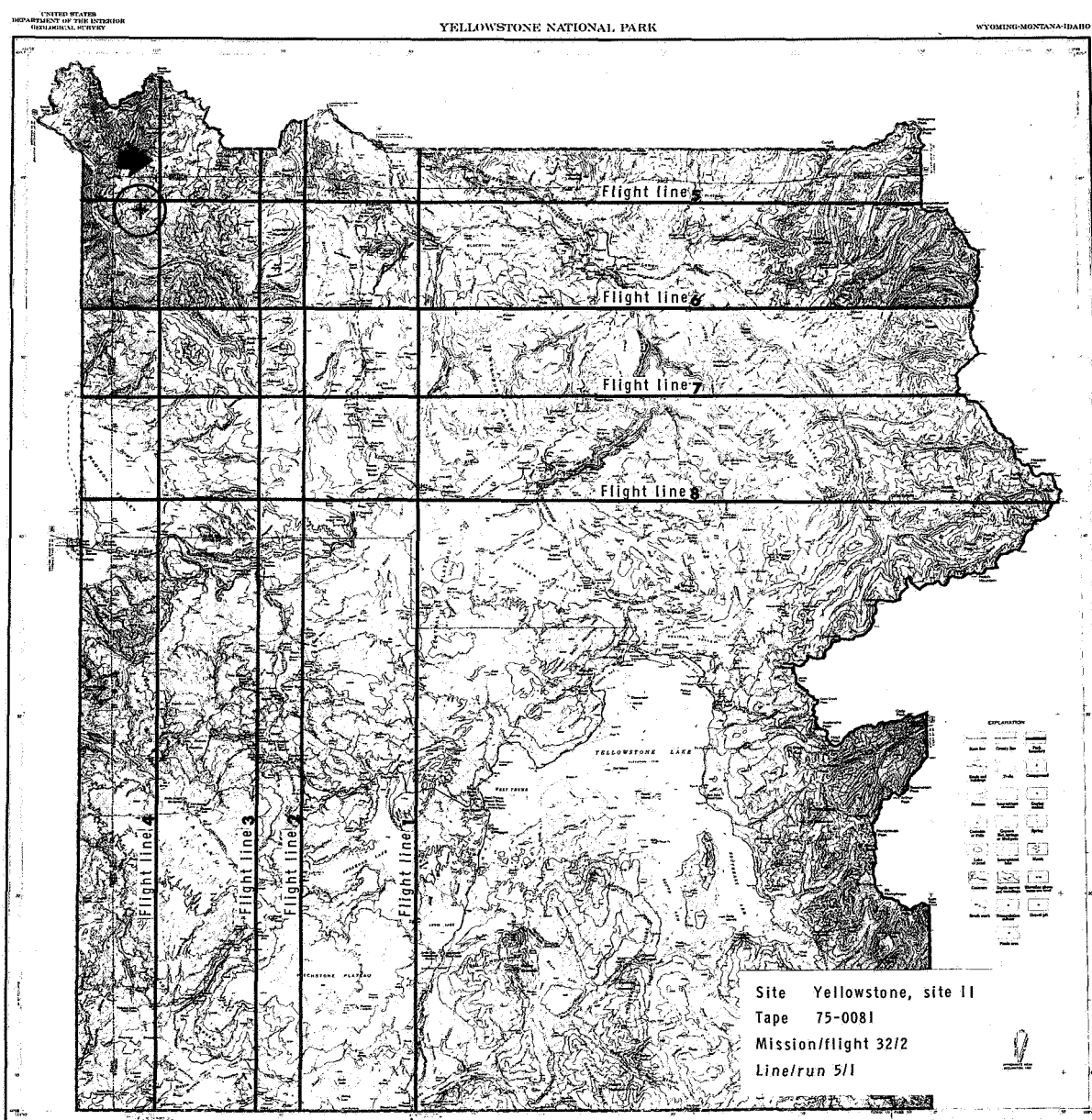
Figure B-10.- Set 10 data samples.



Site 11, Yellowstone
Tape 75 - 0081
Mission / flight / line / run
32 2 5 1

(b) Flight line.

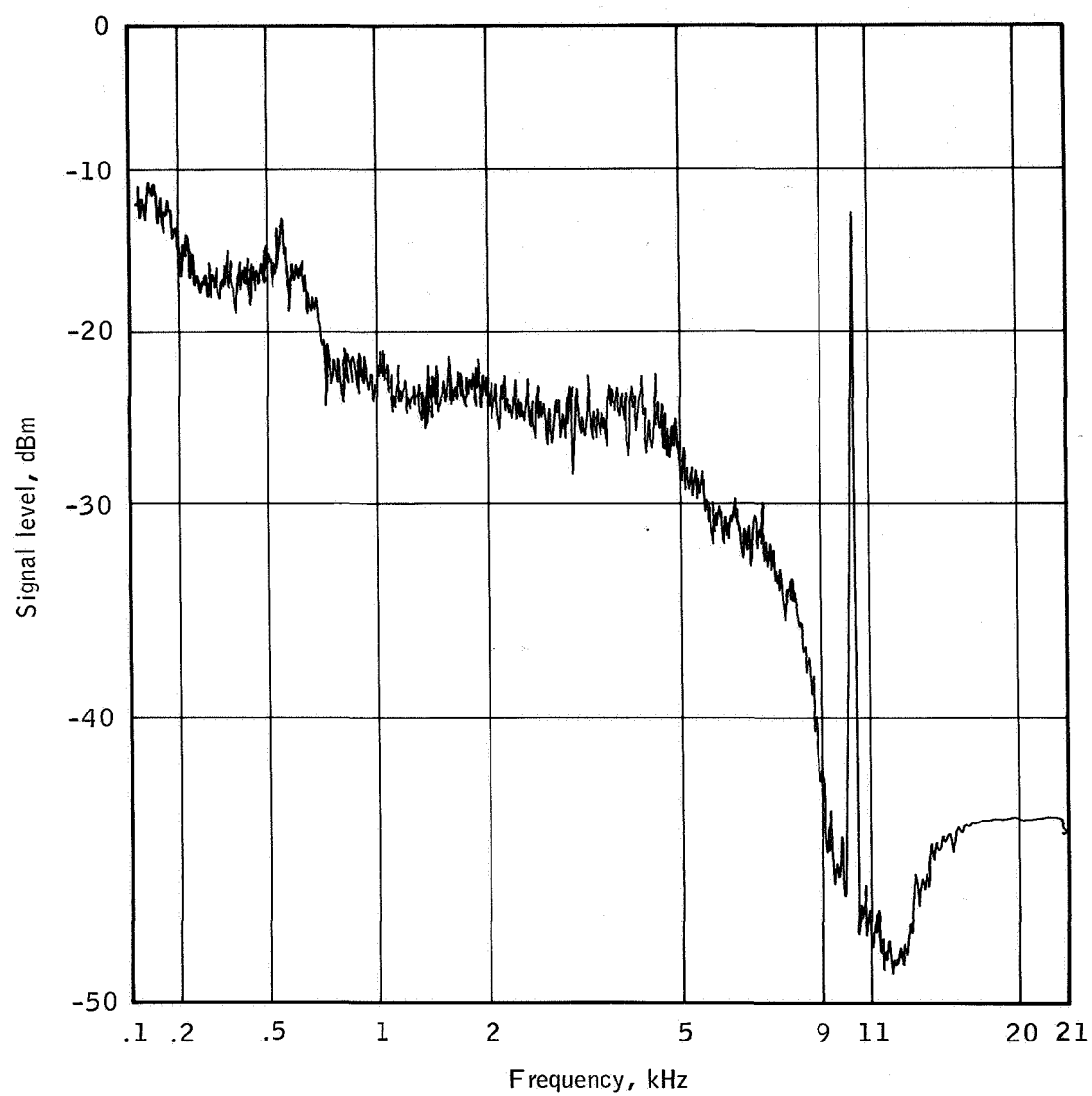
Figure B-10.- Continued.



Scale 1:25 000
1 0 1 2 3 4 5 6 7 8 9 miles
0 10,000 20,000 30,000 feet
5,000 10,000 15,000 20,000 25,000 30,000
1 0 1 2 3 4 5 6 7 8 9 kilometers
Contour interval 80 feet
Datum is mean sea level

(c) Flight map.

Figure B-10.- Continued.



Site 11, Yellowstone

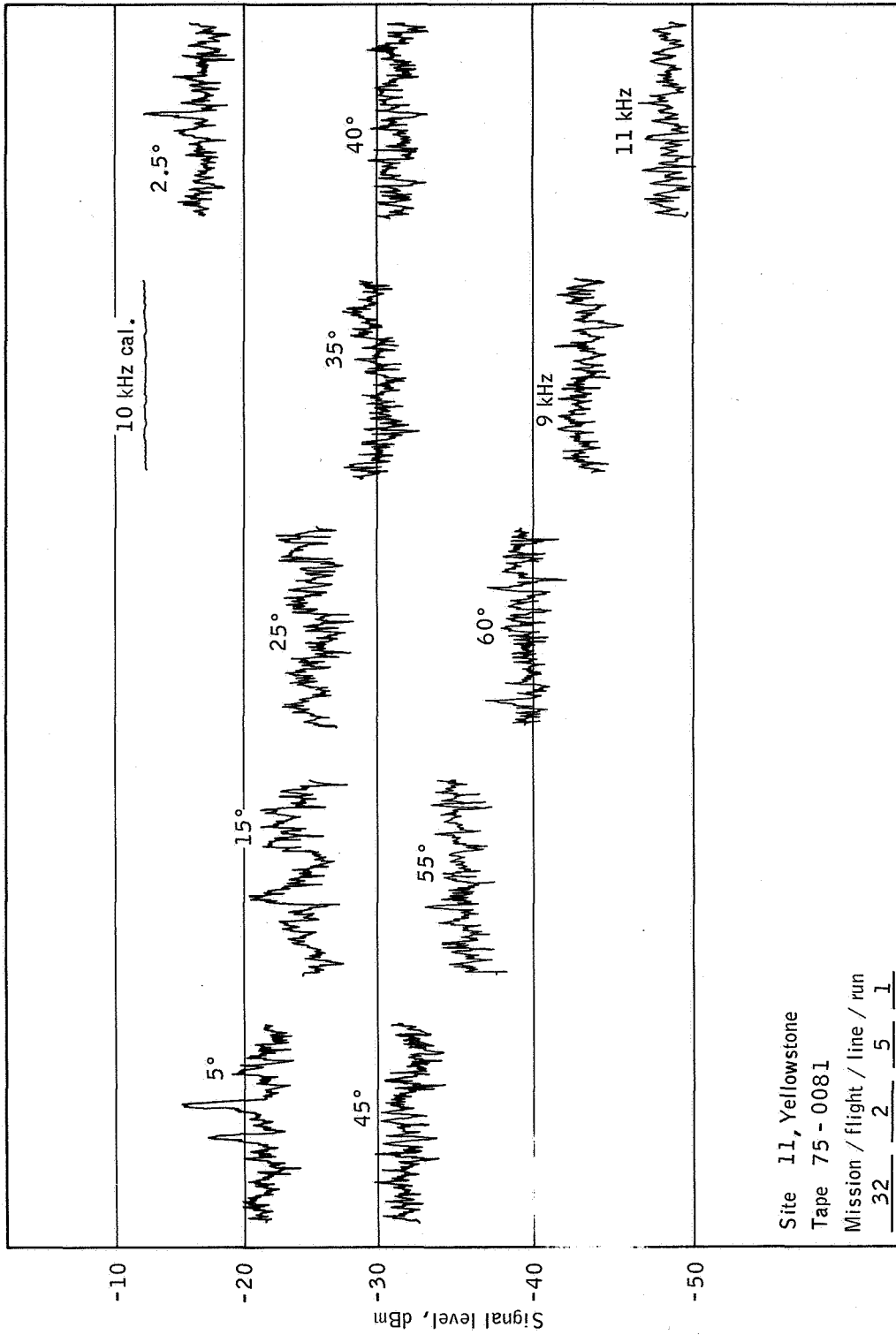
Tape 75 - 0081

Mission / flight / line / run

32 2 5 1

(d) The PSD curve.

Figure B-10.- Continued.



(e) Time history.

Figure B-10.- Concluded.

SET 11 — MISSION DATA

Mission/flight/line/run
32 2 7 1

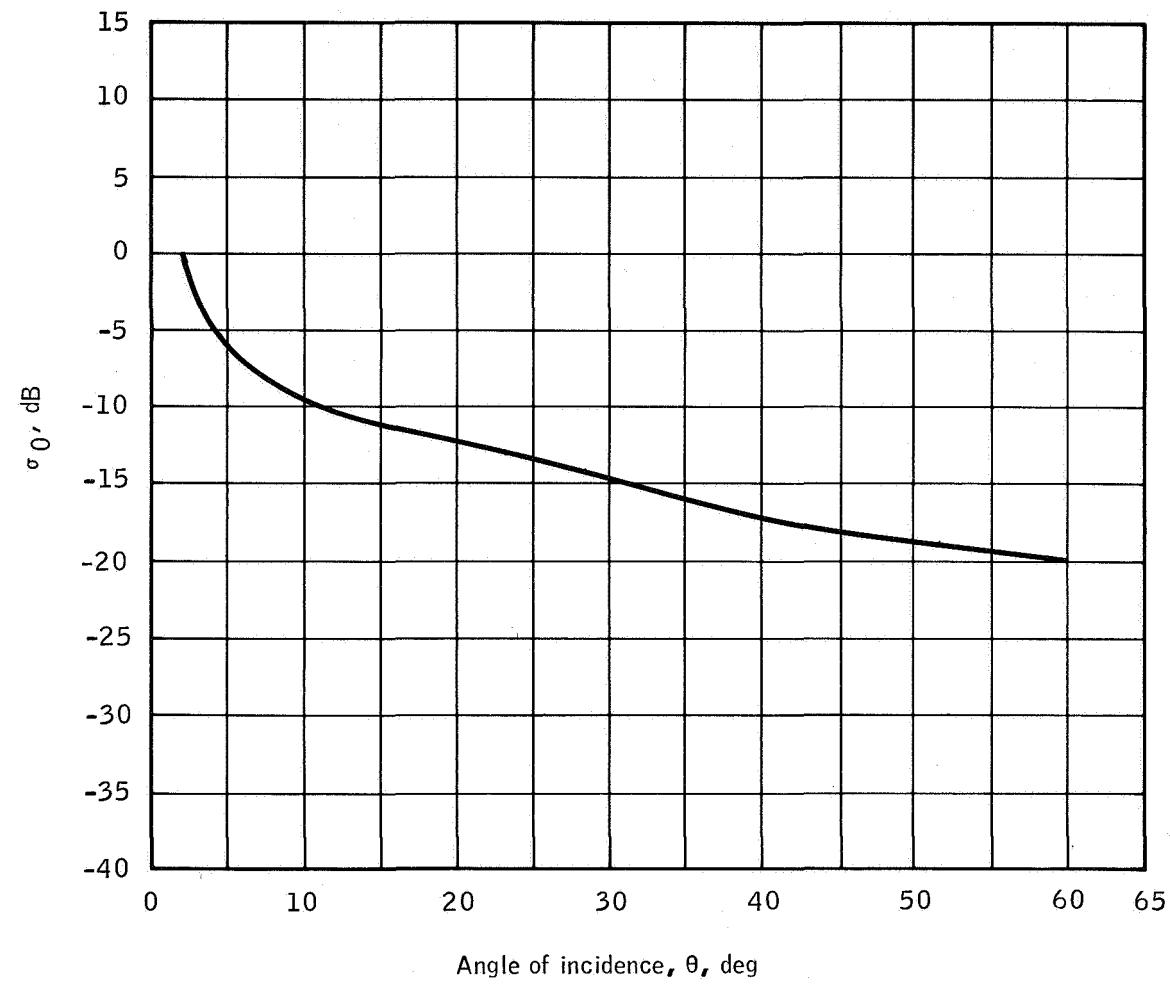
Site 11, Yellowstone National Park

Altitude: 7500 feet

Time: 1151 m.s.t.

Ektachrome color film

The overflown terrain shown in this section is located north of the Madison Valley area and is similar to the sample given for line 5. The percentage of forest cover is reduced and the terrain is somewhat smoother which accounts for the slightly higher returns recorded for angles approaching nadir. Otherwise, the $\sigma_0(\theta)$ curve follows data presented for line 5.



Site 11, Yellowstone	σ_0 sample time		
Tape 75 - 0082	Hours / minutes / seconds		
Mission / flight / line / run	<u>11</u>	<u>51</u>	<u>20</u>
<u>32</u> <u>2</u> <u>7</u> <u>1</u>	Through <u>11</u>	<u>51</u>	<u>30</u>

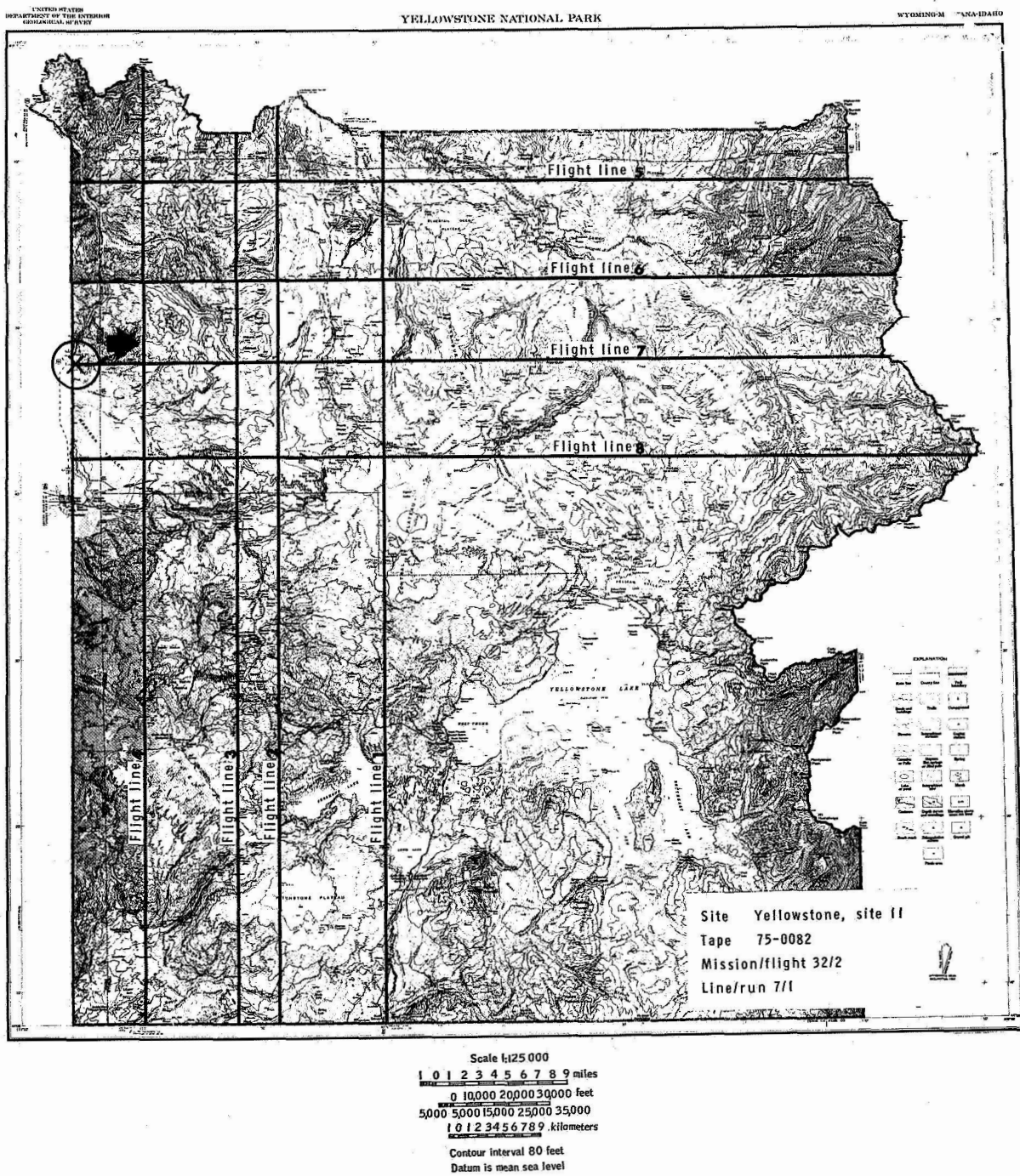
(a) The $\sigma_0(\theta)$ curve.

Figure B-11.- Set 11 data samples.



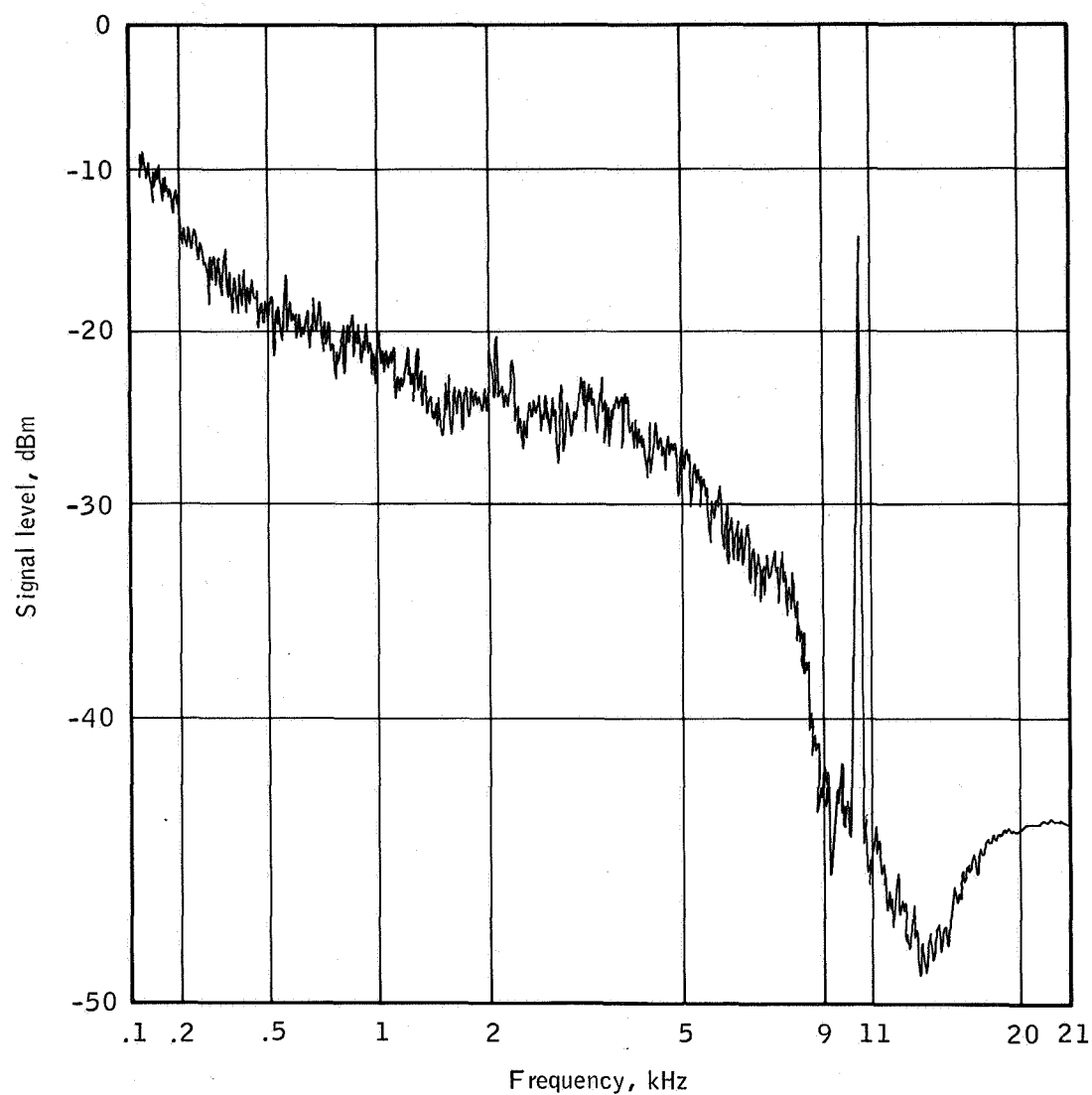
(b) Flight line.

Figure B-11.- Continued.



(c) Flight map.

Figure B-11.- Continued.



Site 11, Yellowstone

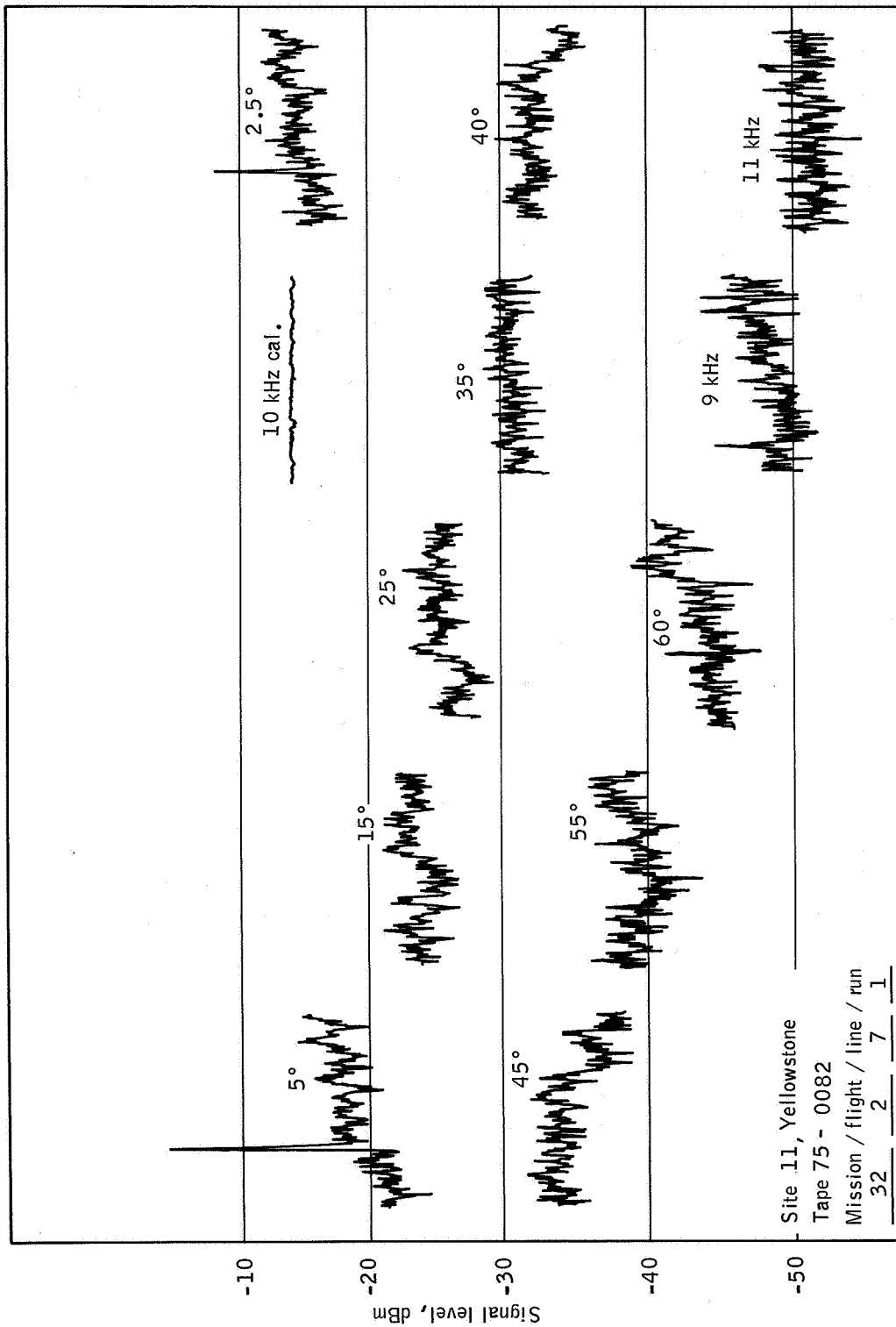
Tape 75 - 0082

Mission / flight / line / run

32 2 7 1

(d) The PSD curve.

Figure B-11.- Continued.



(e) Time history.

Figure B-11.- Concluded.

SET 12 — MISSION DATA

Mission/flight/line/run

32 2 7 1

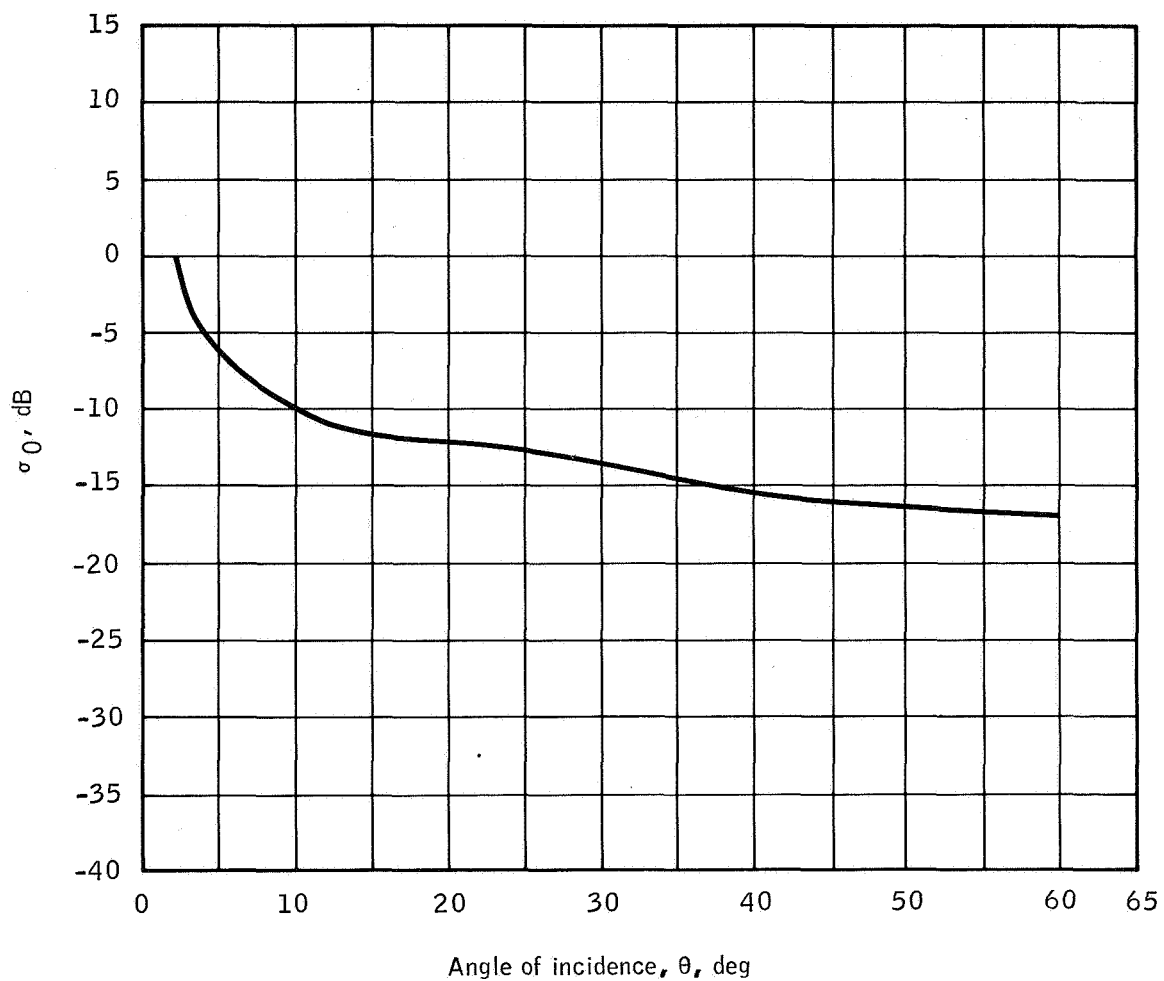
Site 11, Yellowstone National Park

Altitude: 7500 feet

Time: 1204 m.s.t.

Ektachrome color film

These data samples were taken near the eastern end of line 7 in the Deep Creek, Mirror Plateau area. The terrain is very similar to that shown for the western end of line 7. An increased tree density is seen at the larger radar incidence angles. Reflectivity values obtained are almost identical to those recorded for the previous sample. The increasing signal level in the 45° to 60° range correlates with the higher percentage of forest cover and with the scattering theory.



Site 11, Yellowstone

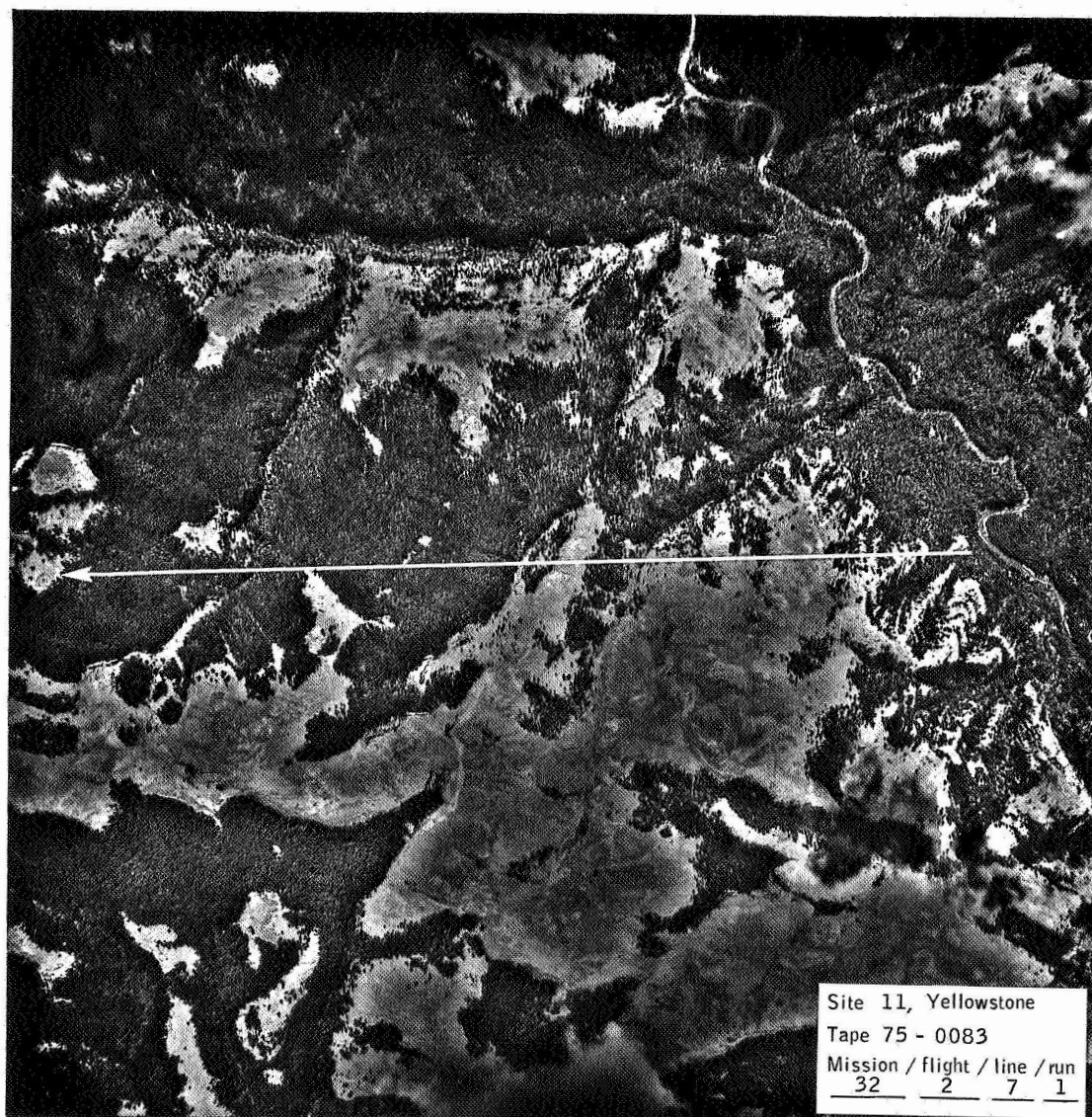
Tape 75 - 0083

Mission / flight / line / run
32 2 7 1 σ_0 sample time

Hours / minutes / seconds

12 03 35Through 12 04 00(a) The $\sigma_0(\theta)$ curve.

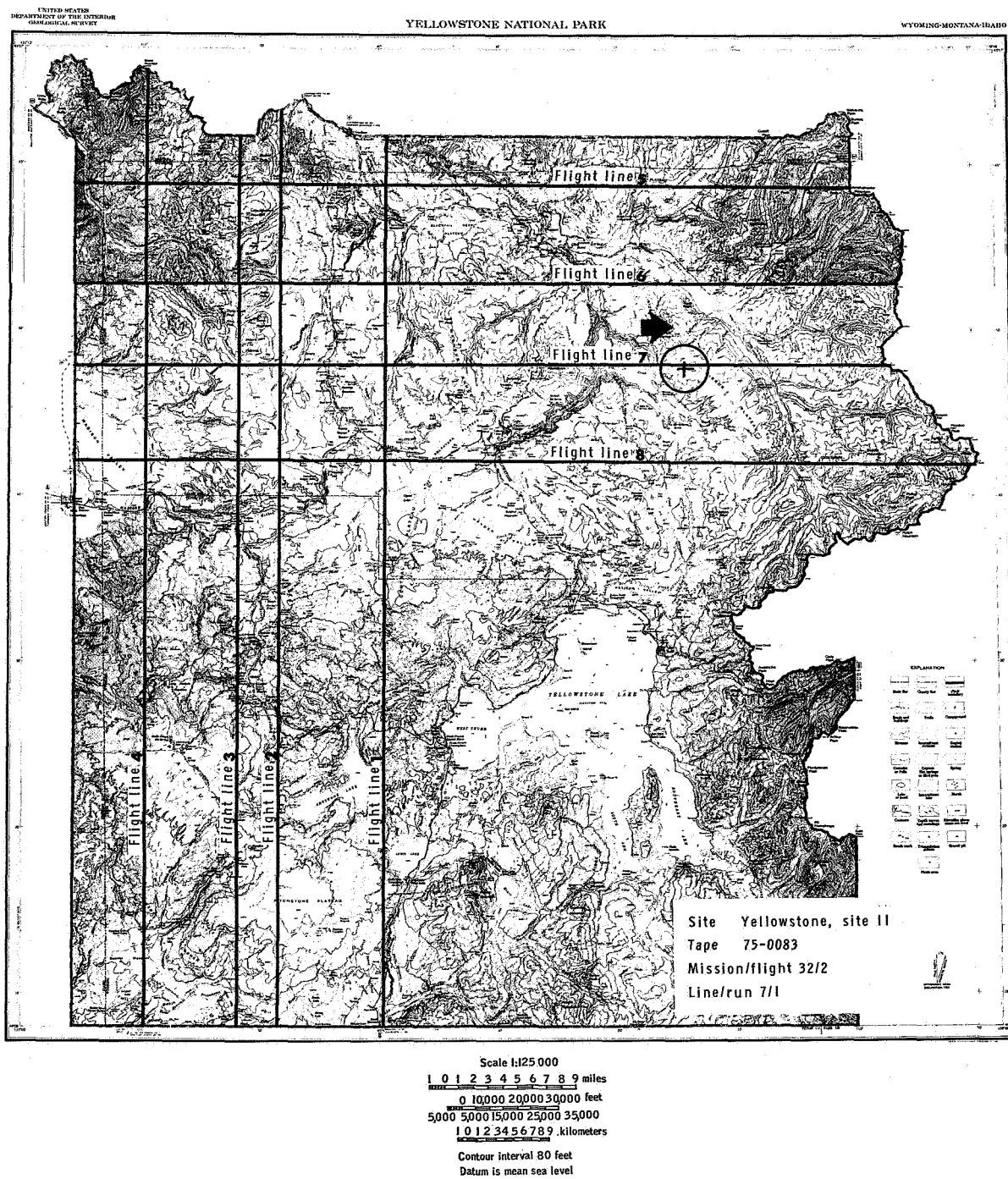
Figure B-12.- Set 12 data samples.



Site 11, Yellowstone
Tape 75 - 0083
Mission / flight / line / run
32 2 7 1

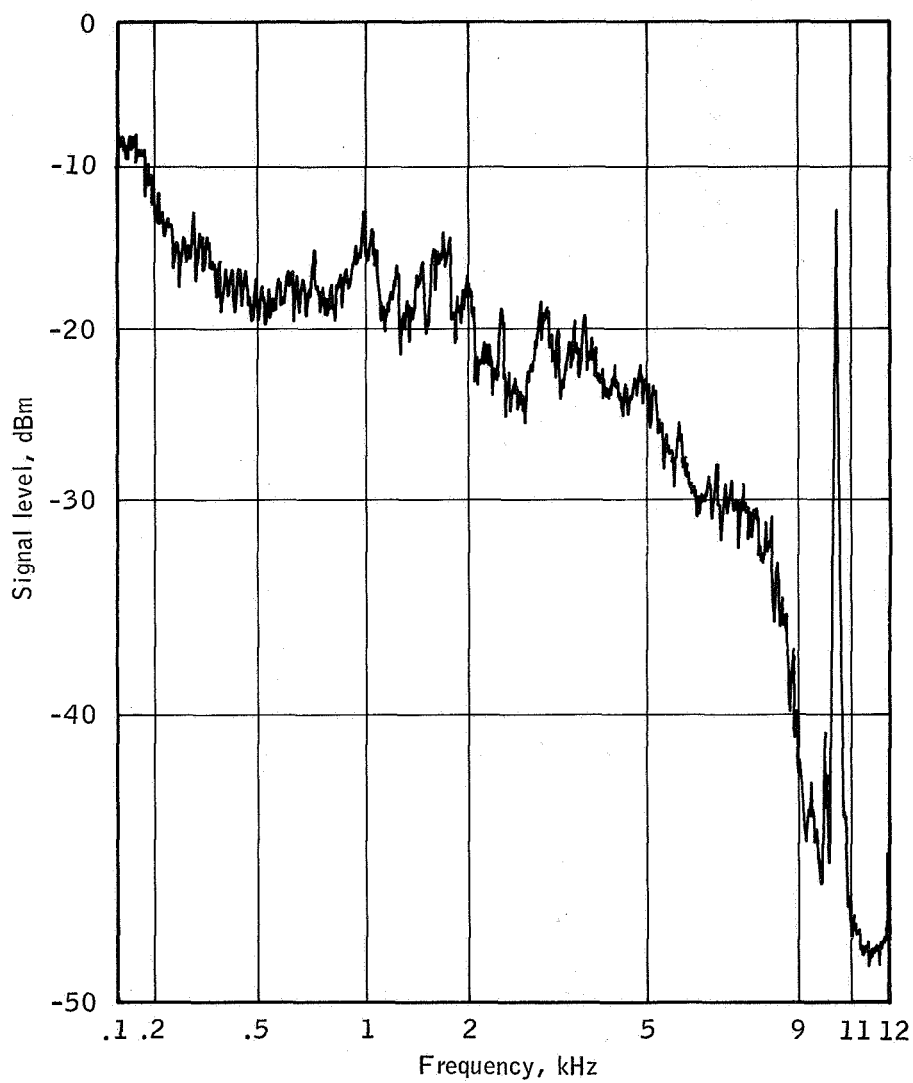
(b) Flight line.

Figure B-12.- Continued.



(c) Flight map.

Figure B-12.- Continued.



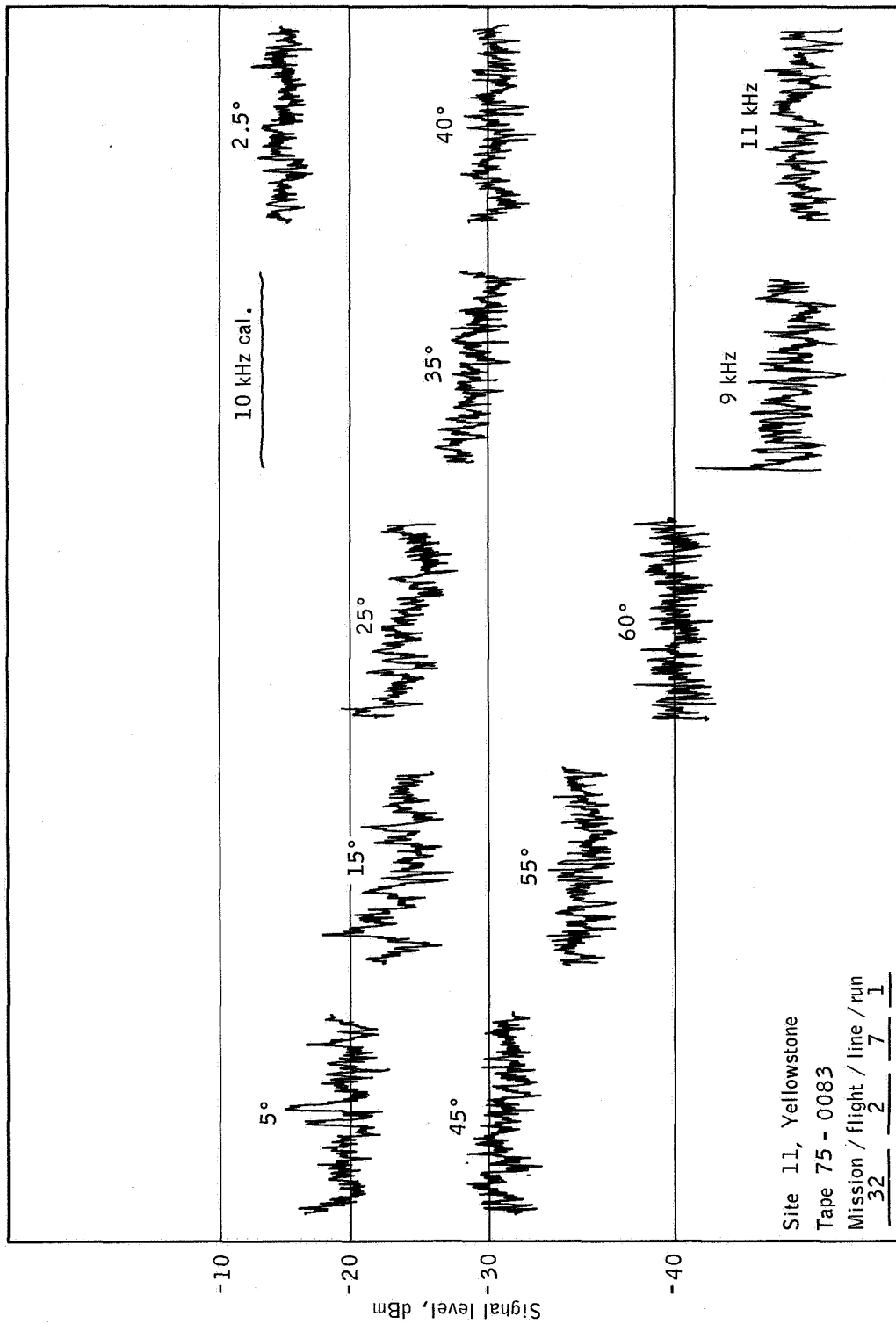
Site 11, Yellowstone

Tape 75 - 0083

Mission / flight / line / run
32 2 7 1

(d) The PSD curve.

Figure B-12.- Continued.



(e) Time history.

Figure B-12.- Concluded.

SET 13 — MISSION DATA

Mission/flight/line/run

35 1 1 1

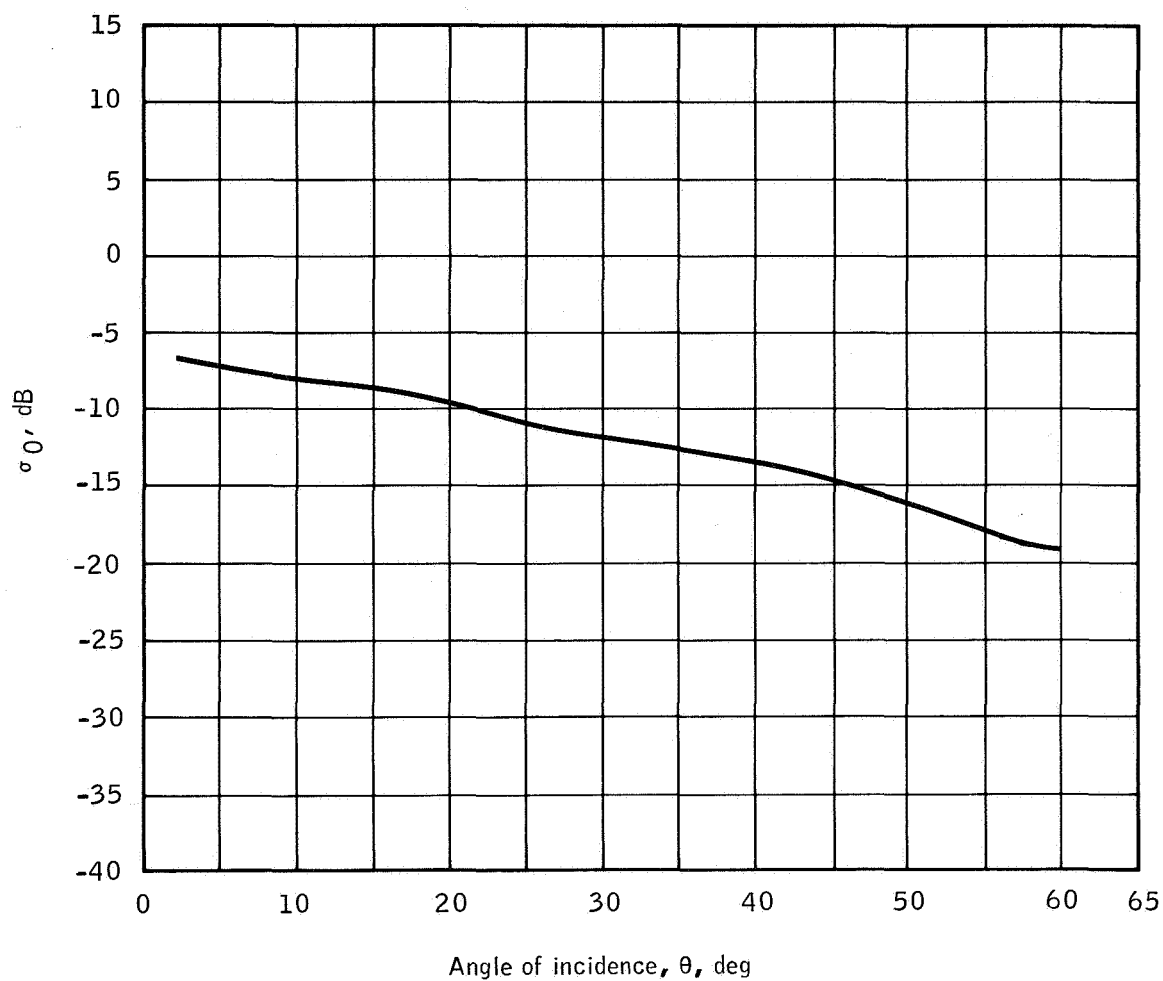
Site 32, Weslaco, Texas

Altitude: 3000 feet

Time: 1304 c.s.t.

Infrared color film

These data samples were taken over the northern end of line 1 on the U.S. Department of Agriculture (USDA) Research Farm, south of Elsa, Texas. The area shown is a combination of low vegetable crops, plowed fields, and grazing land with some low bushes scattered along the flight track. The resultant $\sigma_0(\theta)$ curve compares well with values presented in reference 17 for plowed fields and grazing land.



Site 32, Weslaco	σ_0 sample time
Tape 75 - 0172	Hours / minutes / seconds
Mission / flight / line / run	<u>13</u> <u>04</u> <u>30</u>
<u>35</u> <u>1</u> <u>1</u> <u>1</u>	Through <u>13</u> <u>04</u> <u>40</u>

(a) The $\sigma_0(\theta)$ curve.

Figure B-13.- Set 13 data samples.



(b) Flight line.

Figure B-13.- Continued.

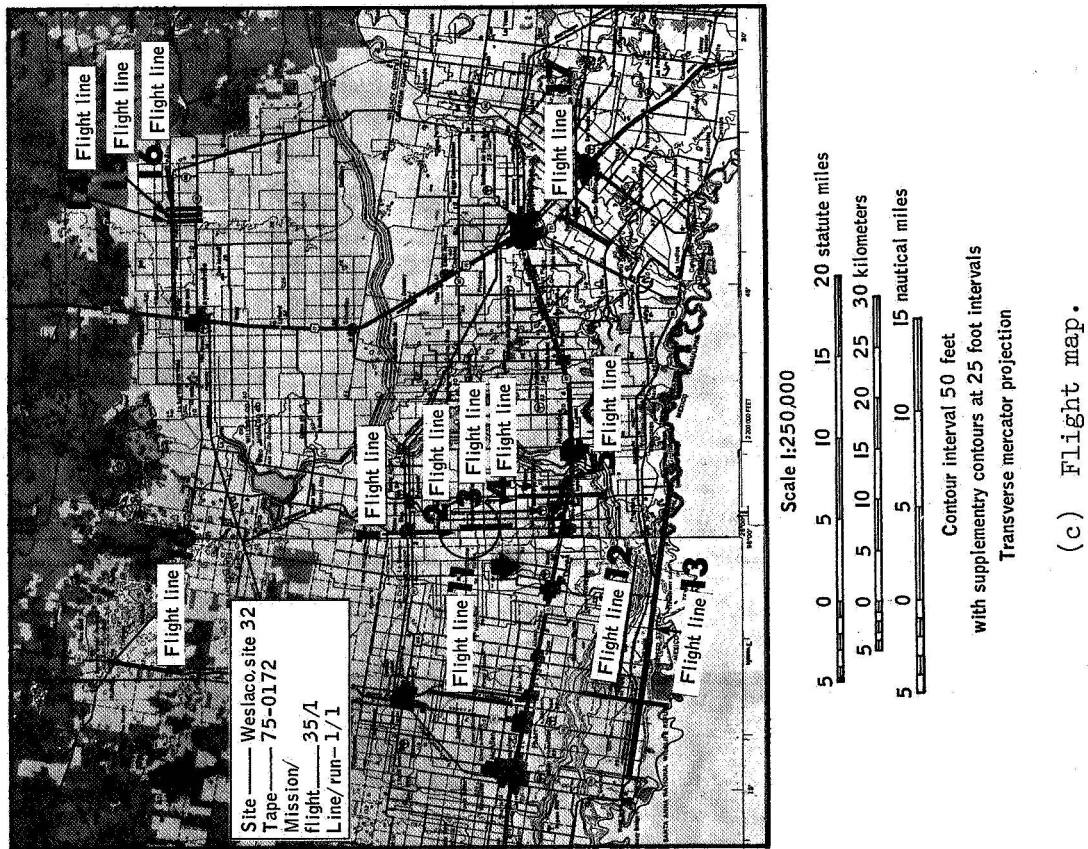
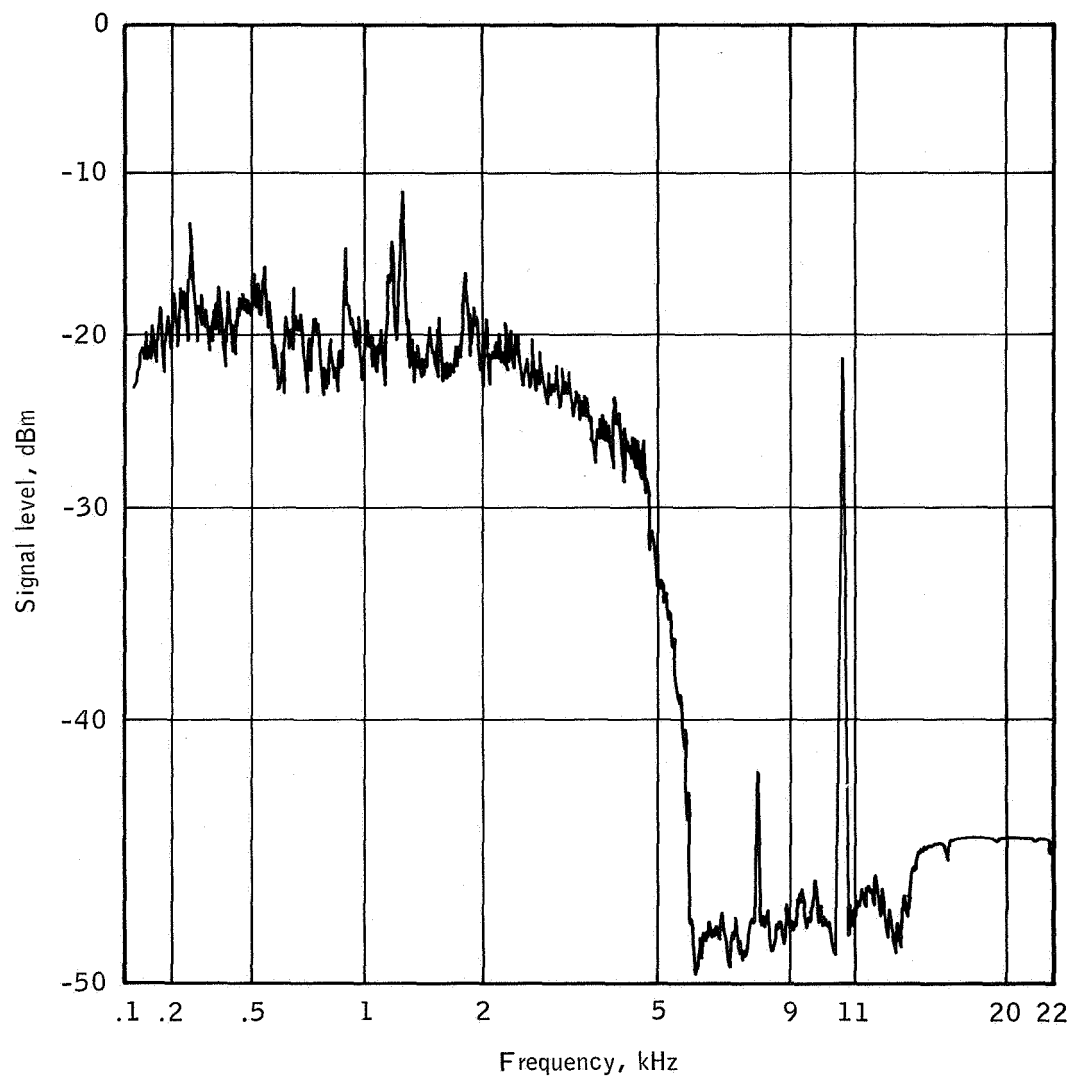


Figure B-13.- Continued.



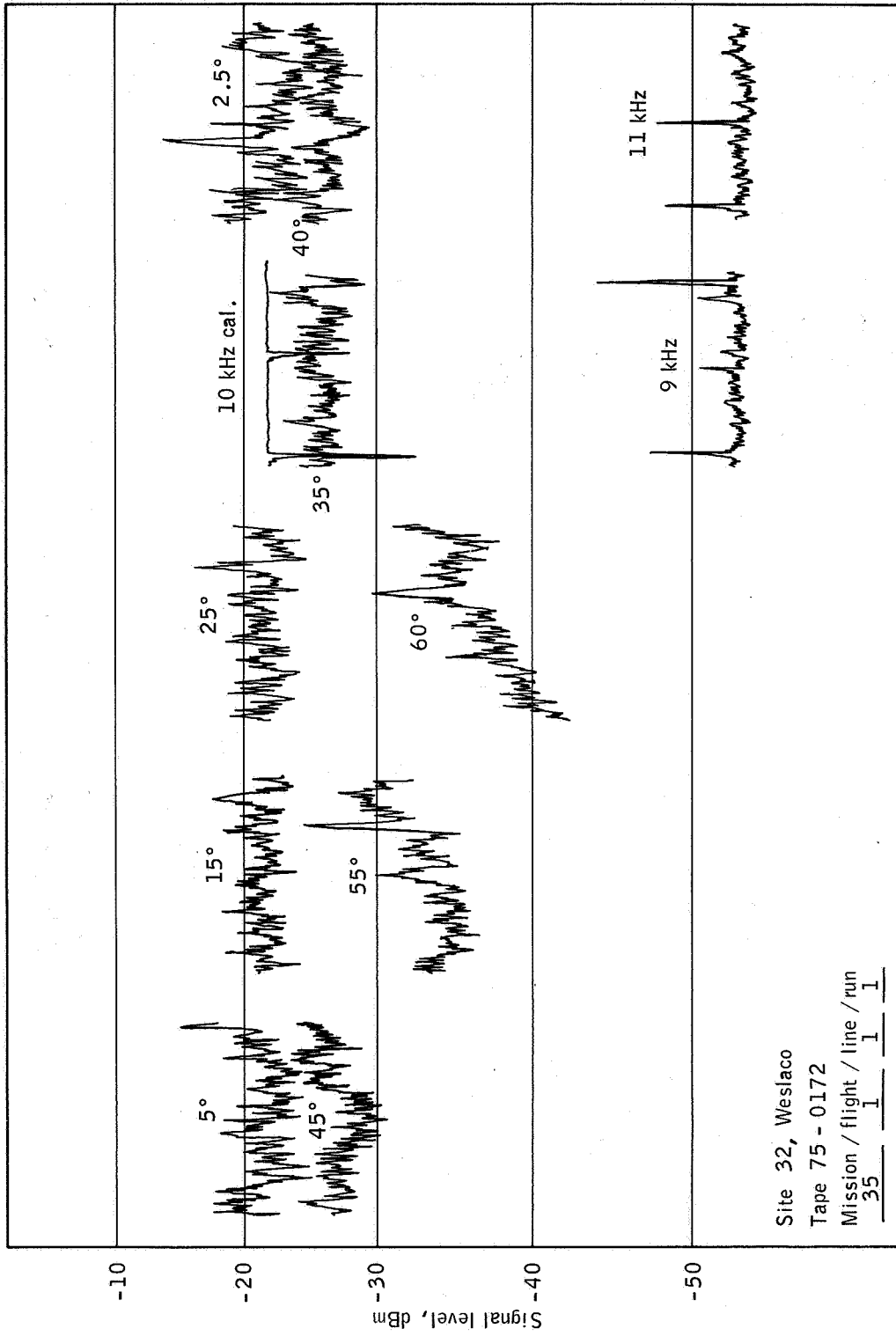
Site 32, Weslaco

Tape 75 - 0172

Mission	flight	line	run
35	1	1	1

(d) The PSD curve.

Figure B-13.- Continued.



(e) Time history.

Figure B-13.- Concluded.

SET 14 — MISSION DATA

Mission/flight/line/run

35 1 12 1

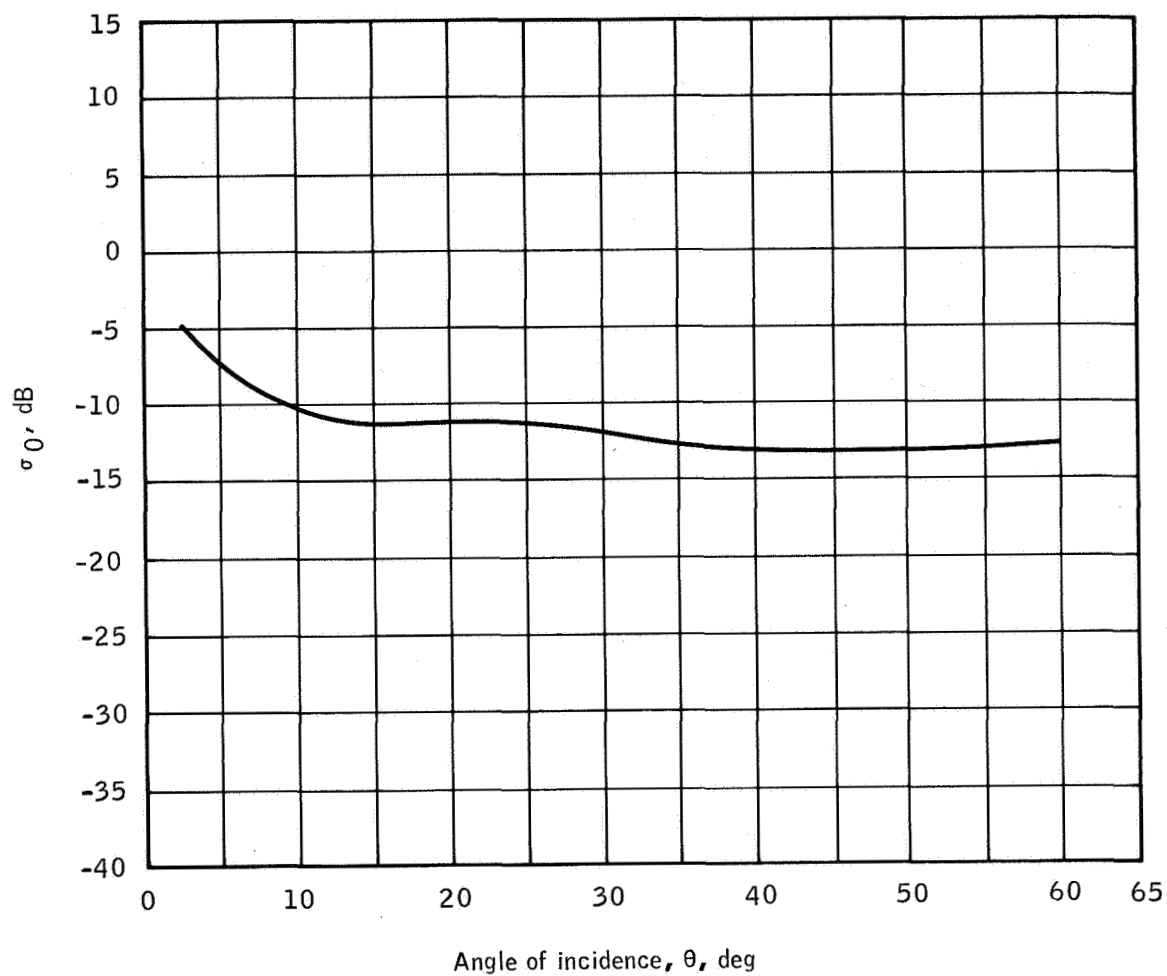
Site 32, Weslaco, Texas

Altitude: 3000 feet

Time: 1352 c.s.t.

Infrared color film

The terrain shown in the photograph in this section is located at the southern end of line 12, on the USDA Military Highway site. Crop height near the center of the targeted area is quite low, and $\sigma_0(\theta)$ values in the angular region of 0° to 35° compare well with data previously published for plowed fields (ref. 17). To the south of Highway 281, vegetation height increases substantially. Also, crops seen at the northern end of this area are more mature than crops nearest the center. This is reflected in the $\sigma_0(\theta)$ data as an increase in signal level at 40° - to 60° -incidence angle.



Site 32, Weslaco

Tape 75 - 0173

Mission / flight / line / run

35 1 12 1 σ_0 sample time

Hours / minutes / seconds

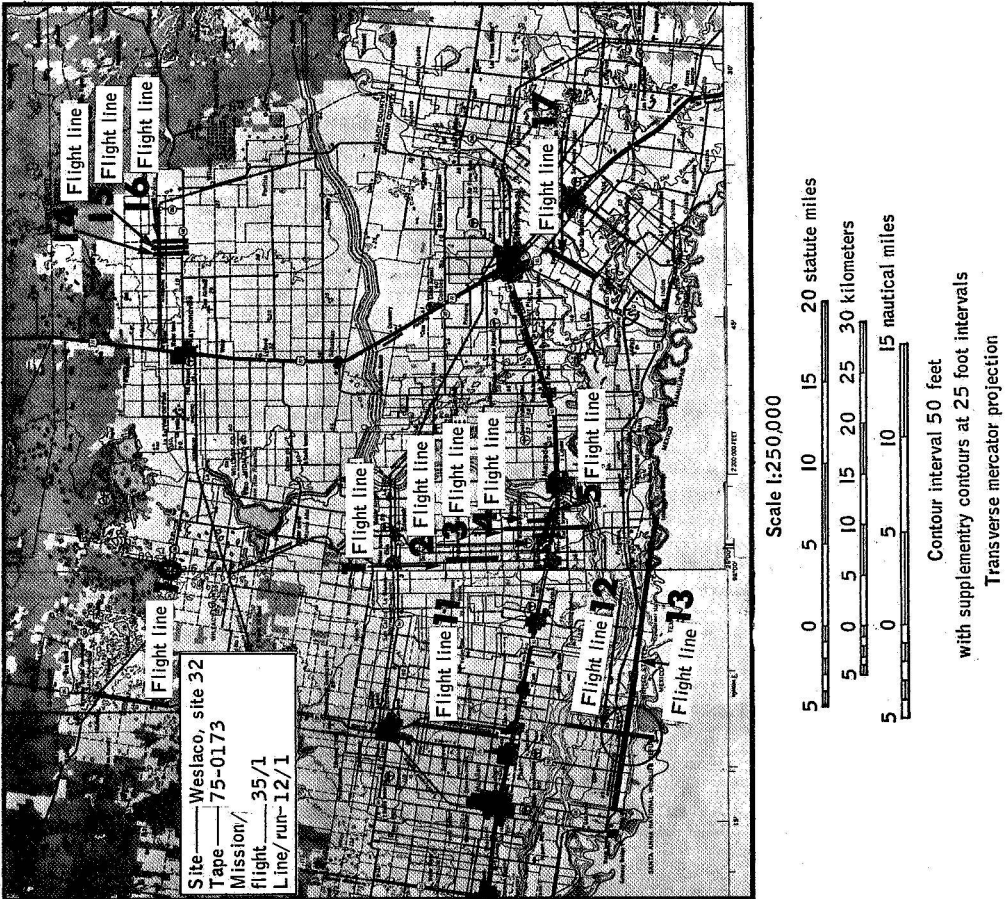
12 52 35Through 12 52 55(a) The $\sigma_0(\theta)$ curve.

Figure B-14.- Set 14 data samples.



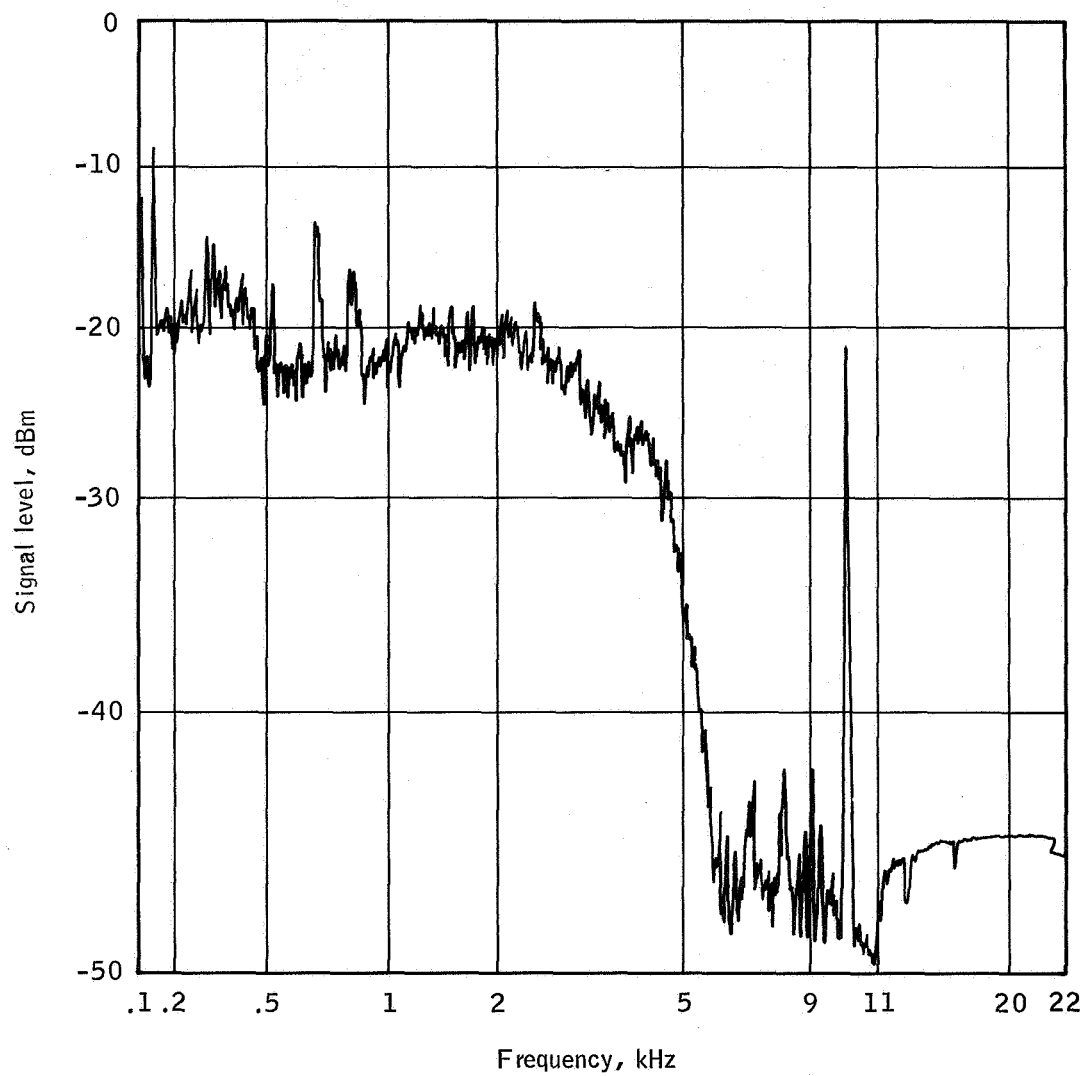
(b) Flight line.

Figure B-14.- Continued.



(c) Flight map.

Figure B-14.- Continued.



Site 32, Weslaco

Tape 75 - 0173

Mission / flight / line / run
35 1 12 1

(d) The PSD curve.

Figure B-14.- Continued.

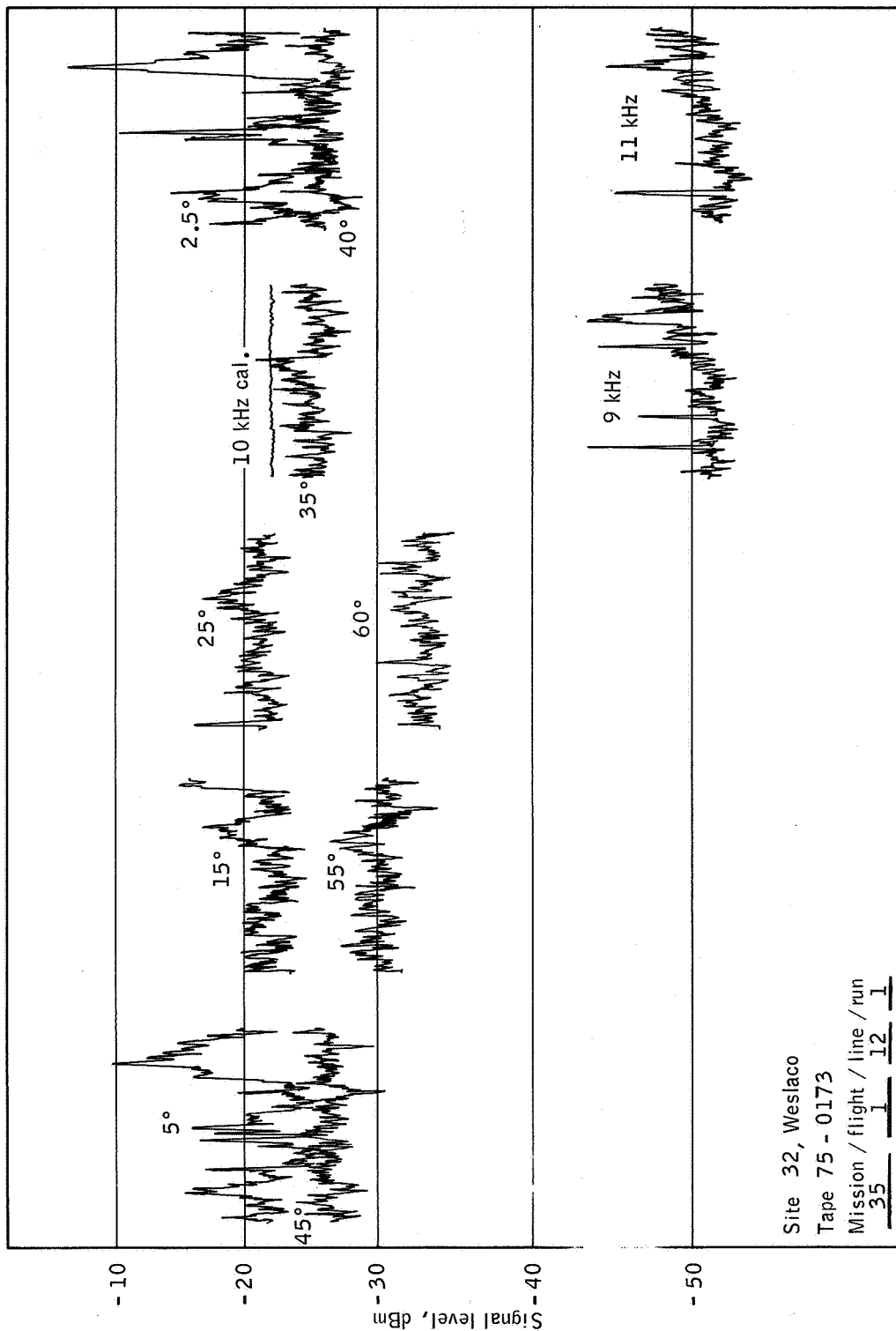


Figure B-14.- Concluded.

SET 15 — MISSION DATA

Mission/flight/line/run

36 1 1 1

Site 102, Lake City, Florida

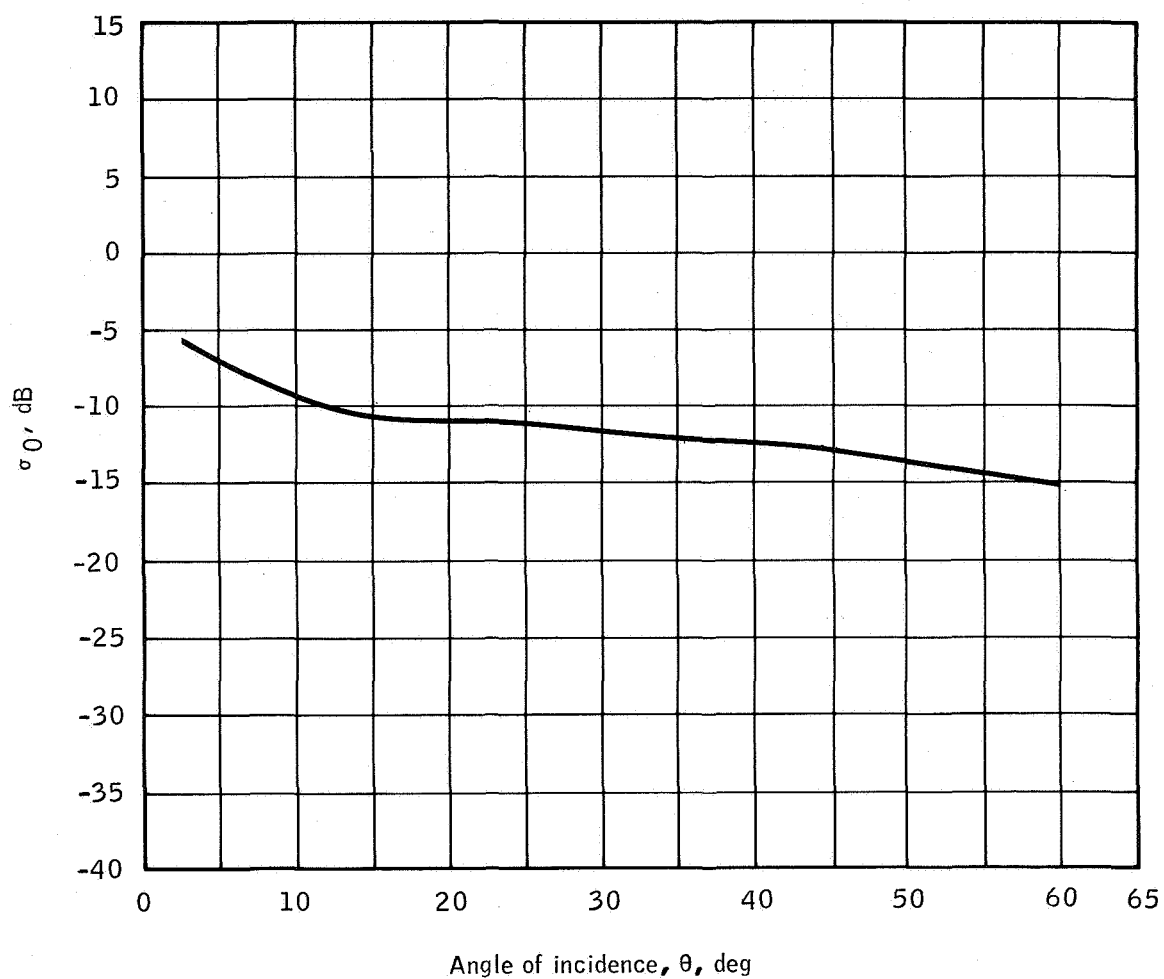
Altitude: 5000 feet

Time: 1308 e.s.t.

Ektachrome color film

These data samples were taken over the northwestern end of line 1, near Jasper, Florida. The area shown is predominantly covered with second growth slash pine, averaging approximately 50 feet in height, with very little underbrush. The terrain is low lying, generally flat, and poorly drained in most places. The soil is mainly red unconsolidated sand.

The $\sigma_0(\theta)$ curve shown follows the data given in reference 14 for the New Jersey trees to 40° and is 2 to 3 dB higher in the region of 40° - to 60° -incidence angle. This increase may be a function of the dense underbrush and tree cover seen by the scatterometer at these angles.



Site 102, Lake City

Tape 75 - 0175

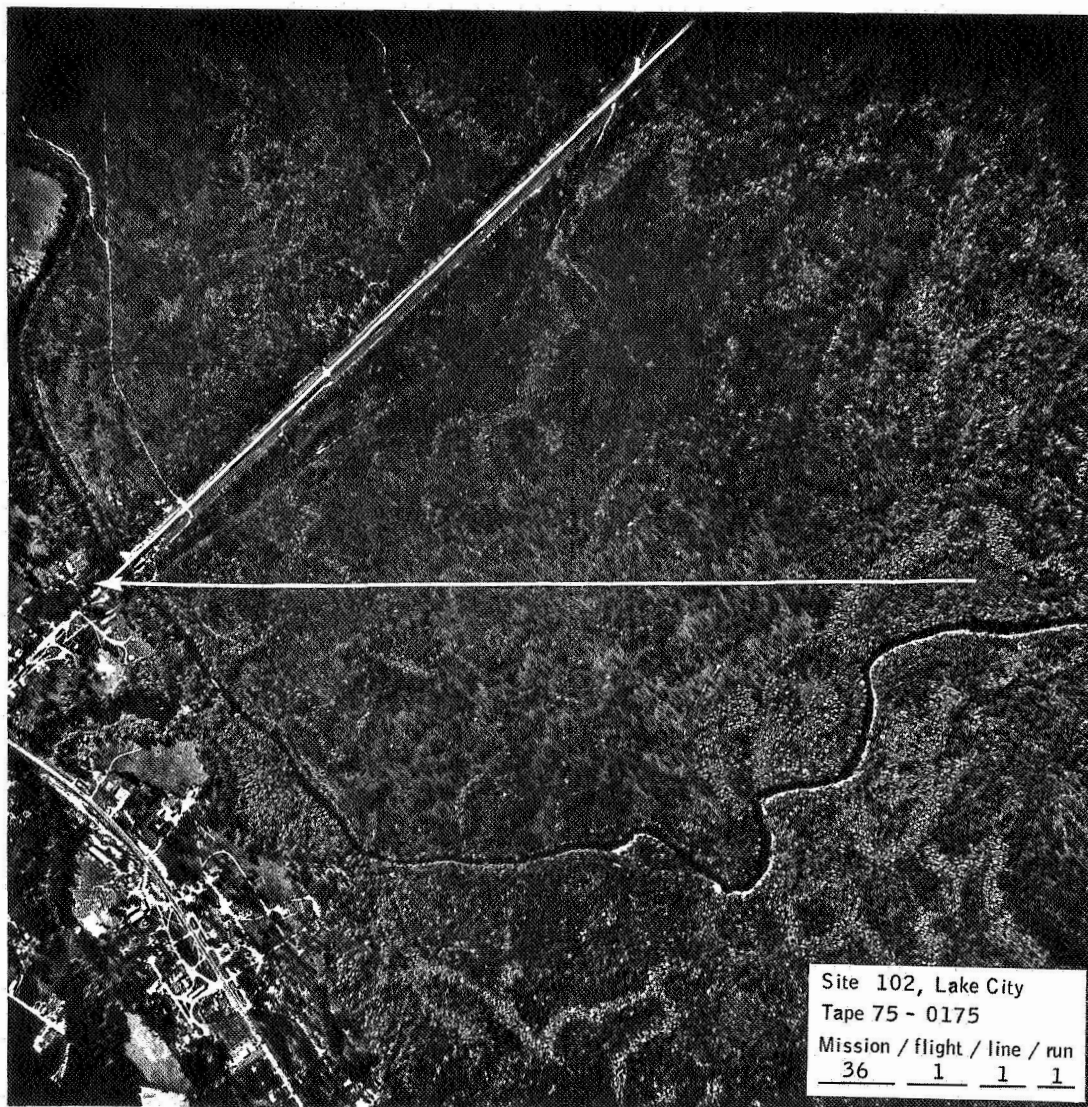
Mission / flight / line / run

36 1 1 1 σ_0 sample time

Hours / minutes / seconds

13 08 25Through 13 08 55(a) The $\sigma_0(\theta)$ curve.

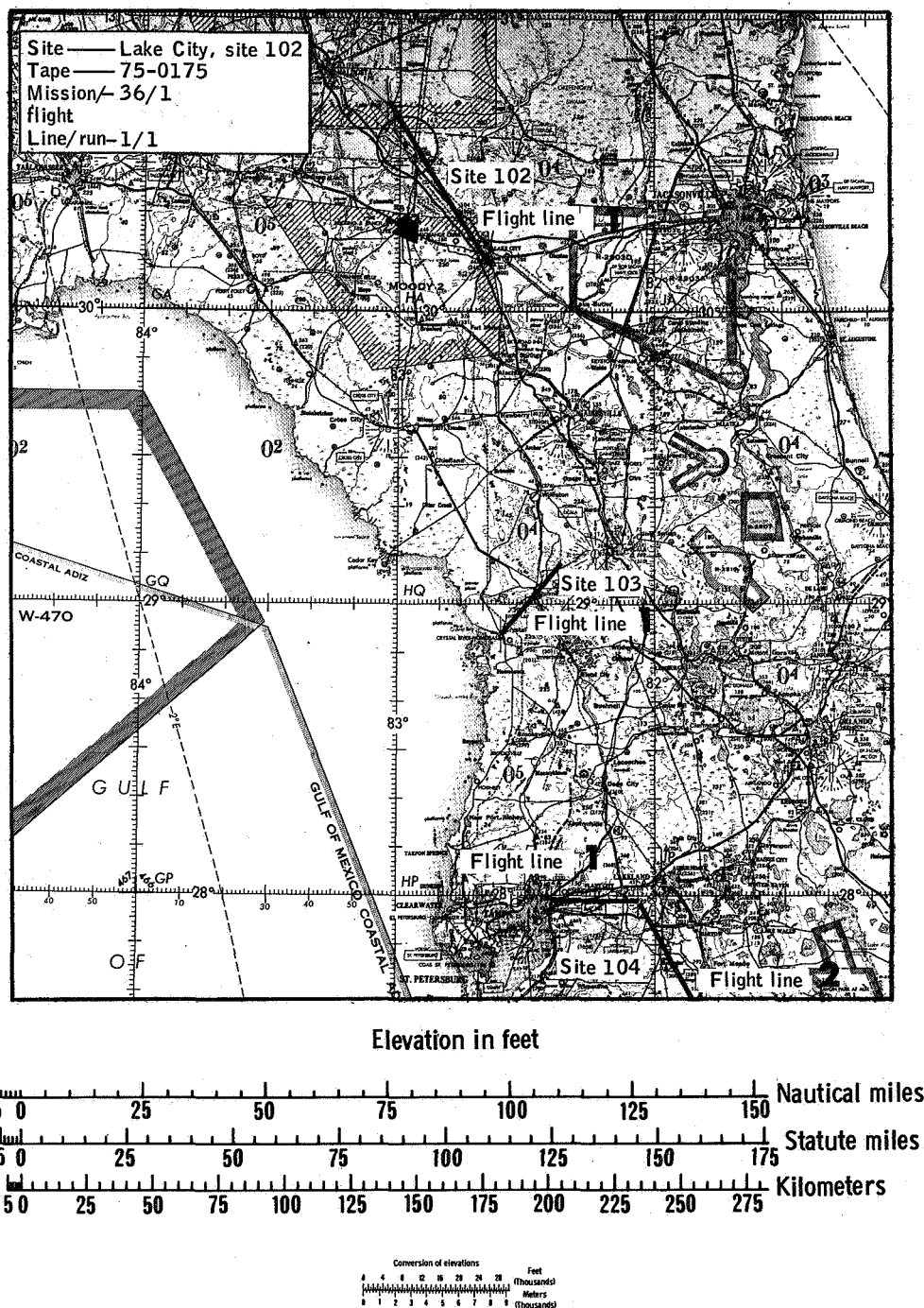
Figure B-15.- Set 15 data samples.



Site 102, Lake City
Tape 75 - 0175
Mission / flight / line / run
36 1 1 1

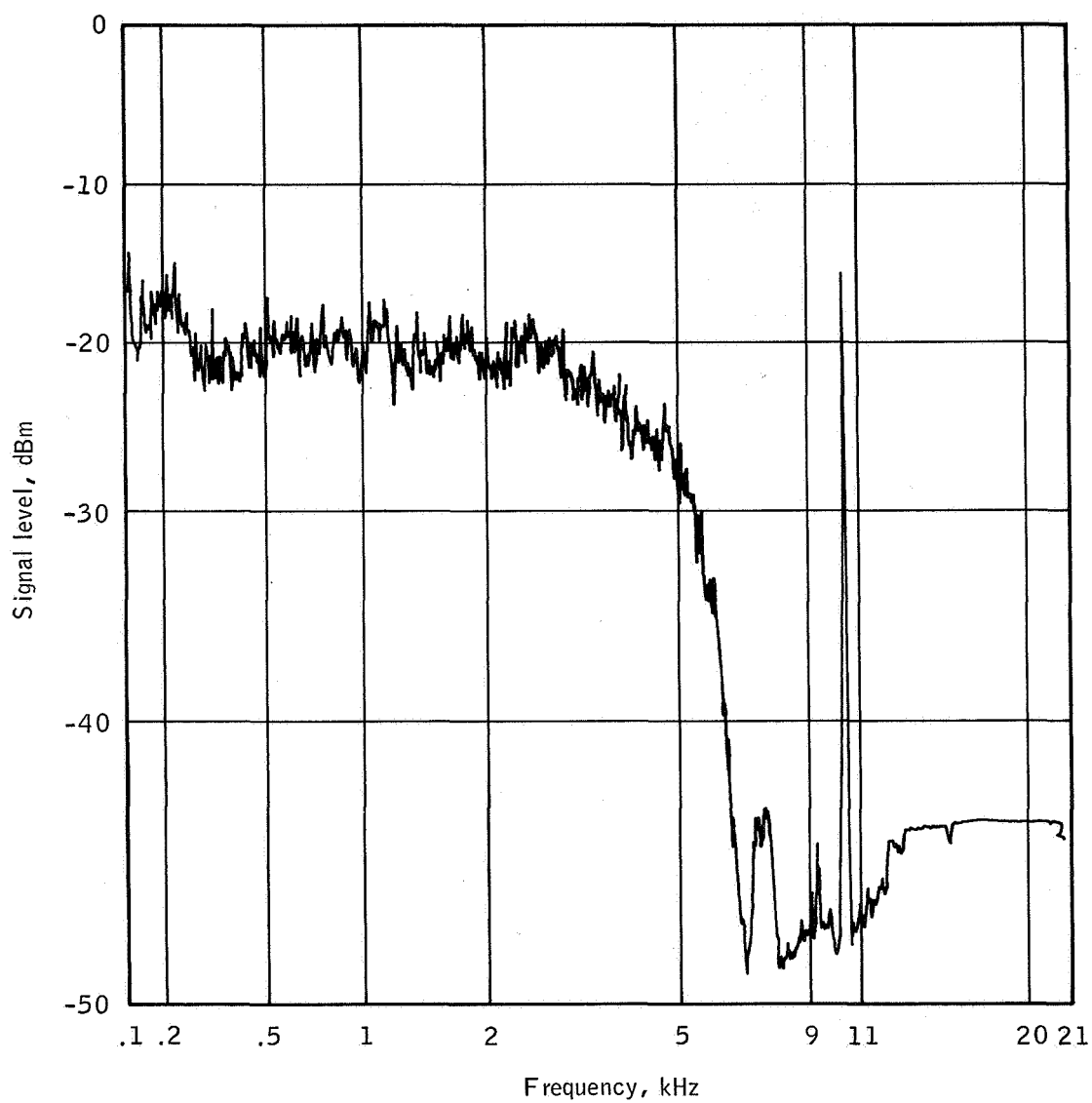
(b) Flight line.

Figure B-15.- Continued.



(c) Flight map.

Figure B-15.— Continued.



Site 102, Lake City

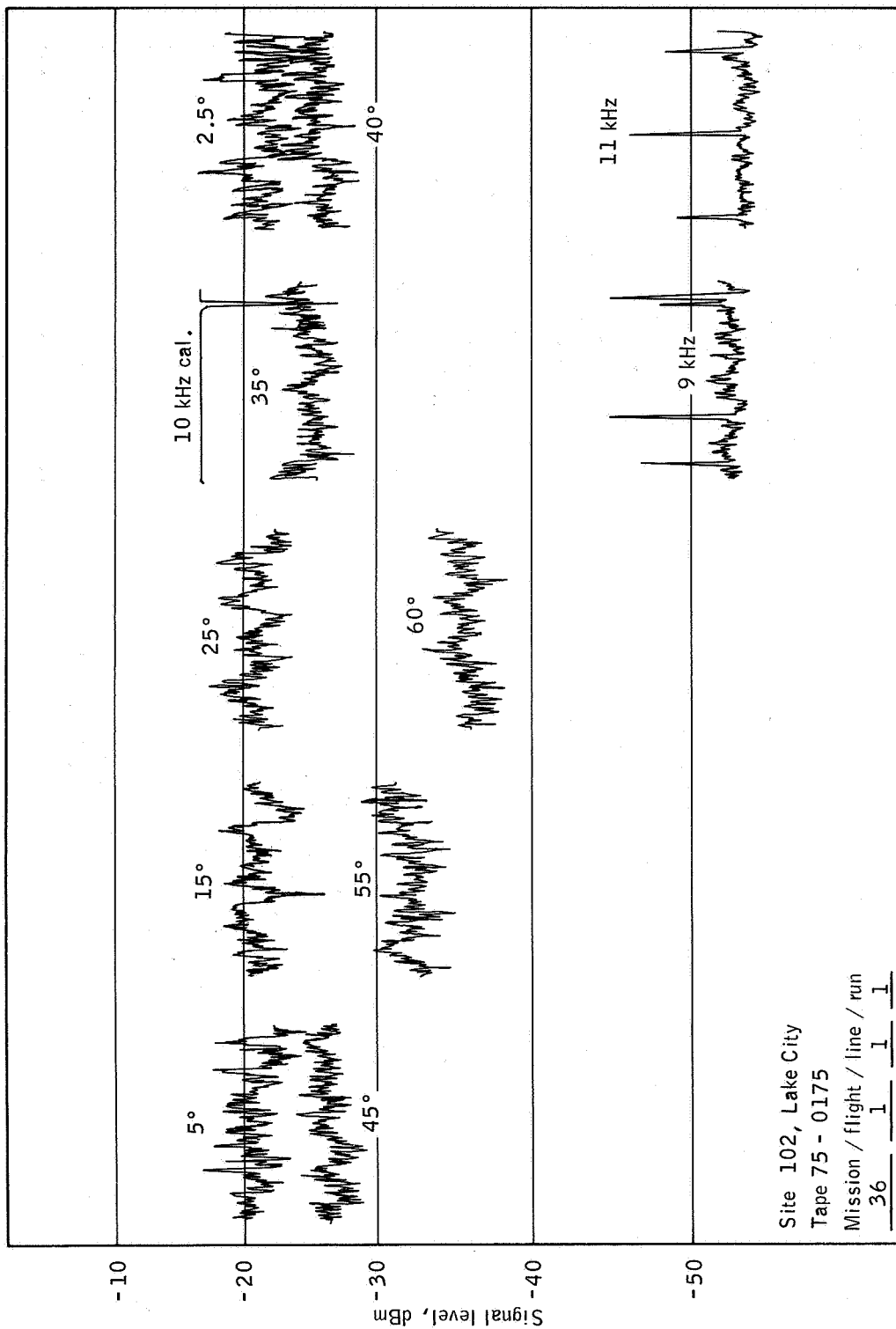
Tape 75 - 0175

Mission / flight / line / run

36 1 1 1

(d) The PSD curve.

Figure B-15.- Continued.



(e) Time history.

Figure B-15.- Concluded.

SET 16 — MISSION DATA

Mission/flight/line/run

36 2 3 2

Site 95, Everglades, Florida

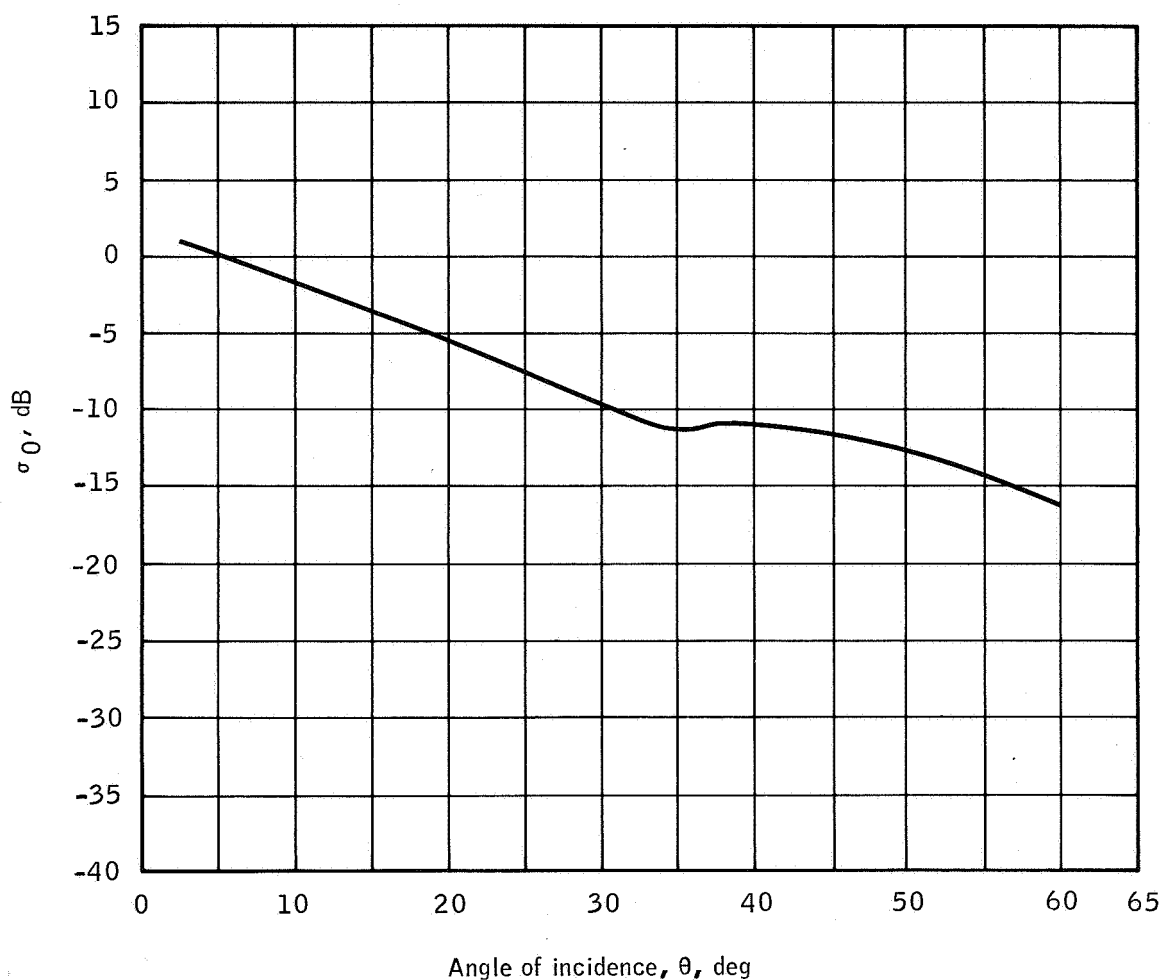
Altitude: 7000 feet

Time: 0922 e.s.t.

Infrared color film

These samples are representative of the Everglades area and were taken near the center of line 3. The area shown is mostly flat swampland with approximately 50-percent dense grass cover. The remaining surface is peat moss, water, and small tree-islands ranging from 20 to 1000 feet in diameter.

In the $\sigma_0(\theta)$ curve presented, agreement is found with reference data for wooded swamp (ref. 17) in the angular regions of 0° to 5° and 40° to 60° . The $\sigma_0(\theta)$ values for 15° and 25° are unusually high.



Site 95, Everglades

Tape 75 - 0178

Mission / flight / line / run

36 2 3 2

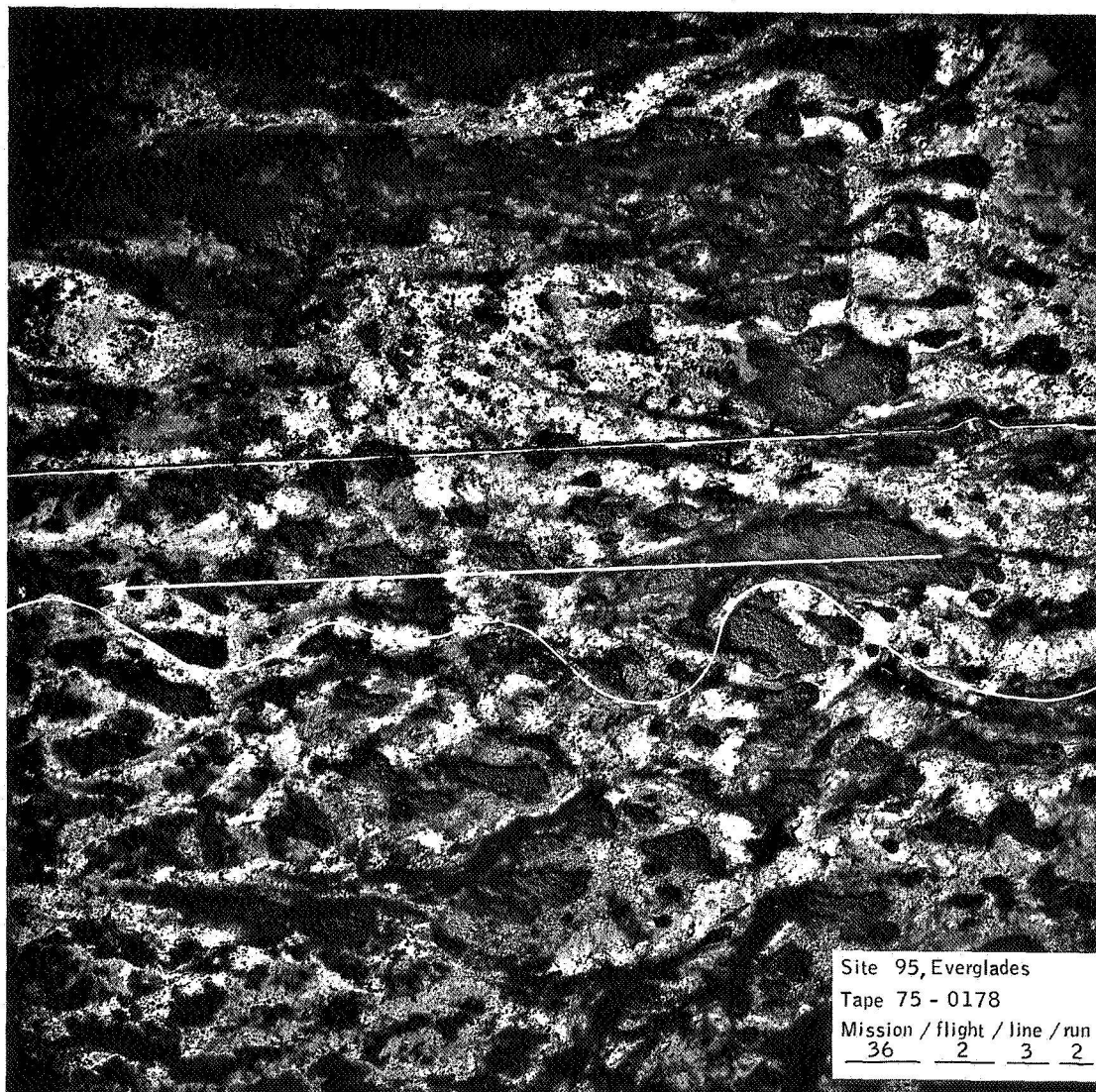
Through

 σ_0 sample time

Hours / minutes / seconds

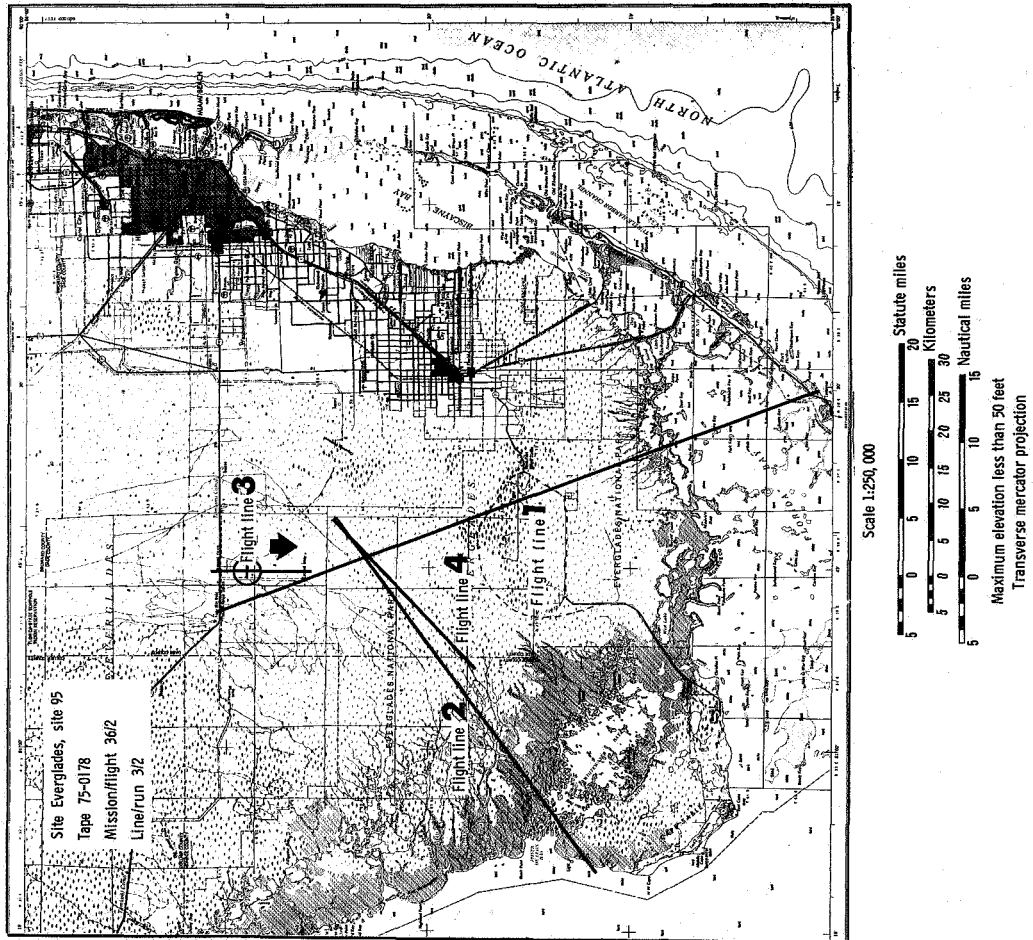
09 22 2509 22 35(a) The $\sigma_0(\theta)$ curve.

Figure B-16.- Set 16 data samples.



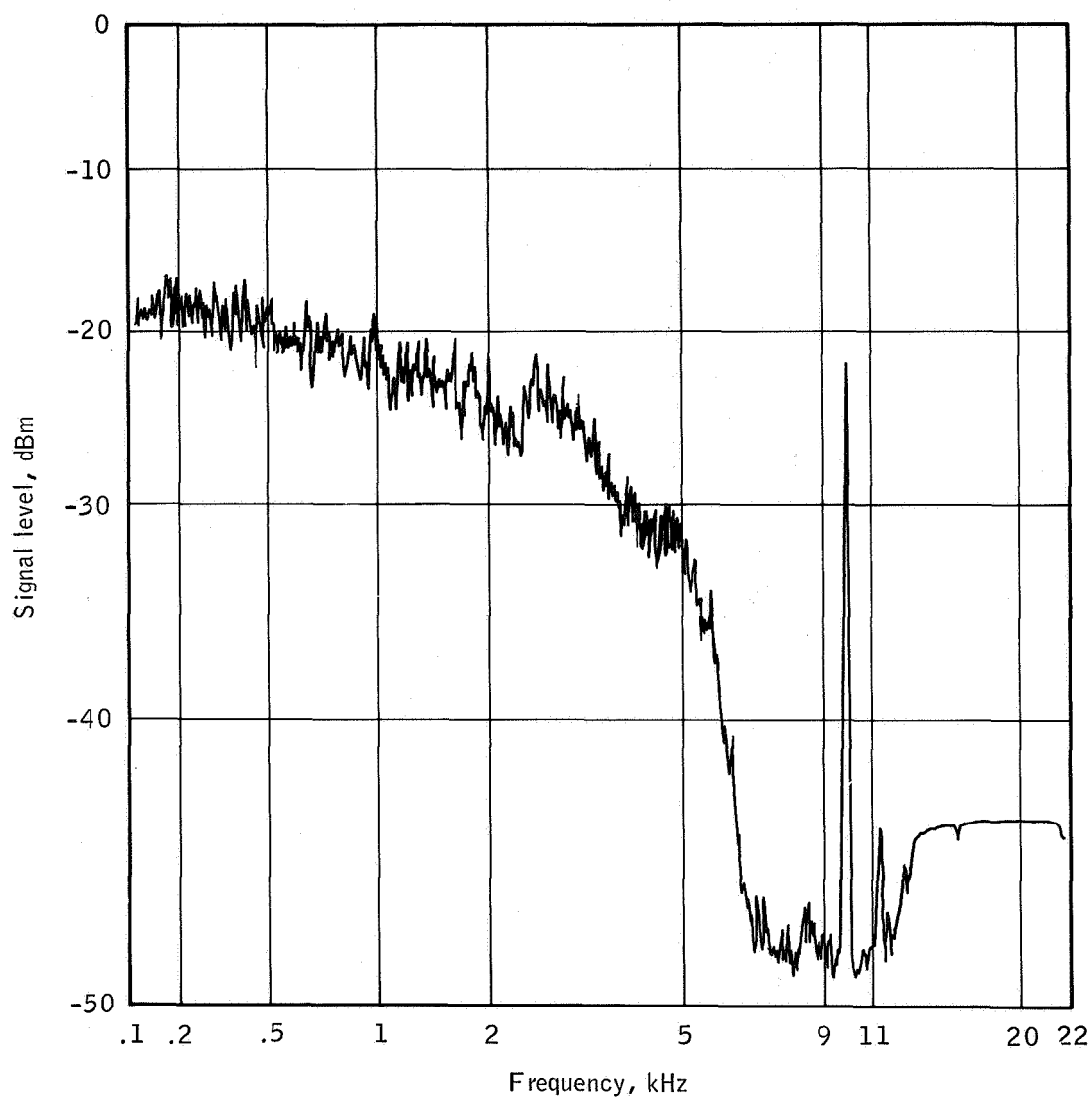
(b) Flight line.

Figure B-16.- Continued.



(c) Flight map.

Figure B-16.- Continued.



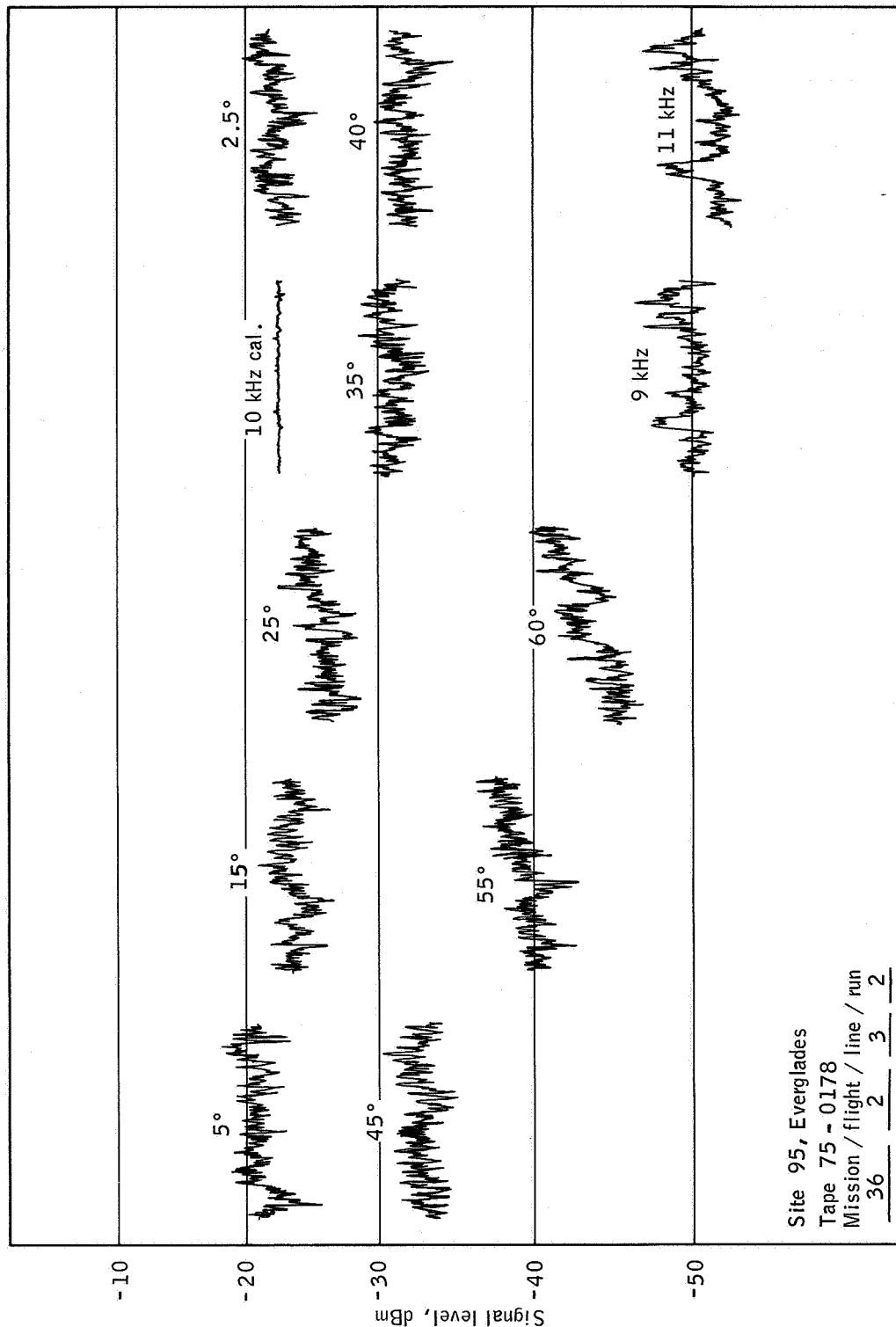
Site 95, Everglades

Tape 75 - 0178

Mission / flight / line / run
36 2 3 2

(d) The PSD curve.

Figure B-16.- Continued.



(e) Time history.

Figure B-16.- Concluded.

SET 17 — MISSION DATA

Mission/flight/line/run

36 4 1 1

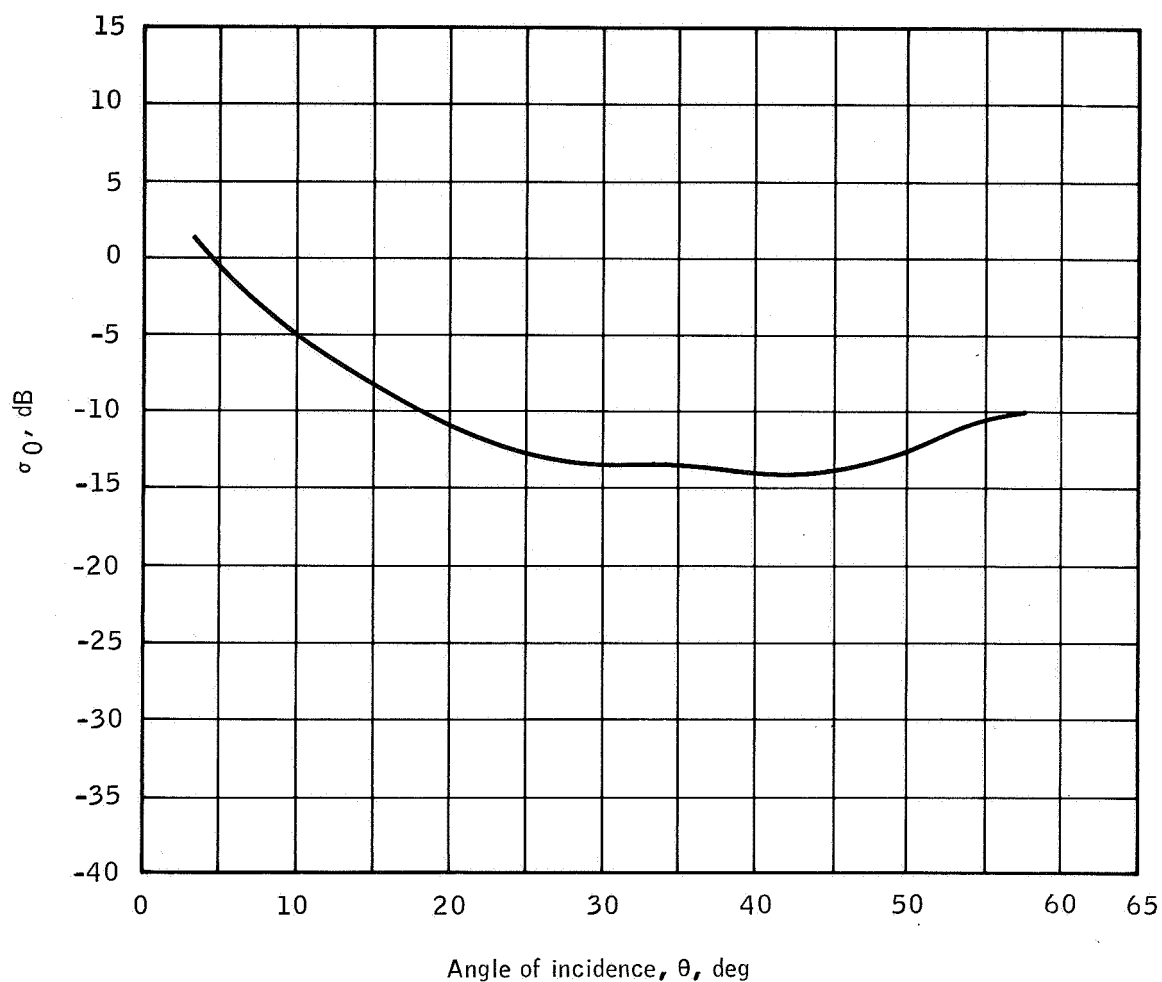
Site 95, Everglades, Florida

Altitude: 7000 feet

Time: 0848 e.s.t.

Infrared color film

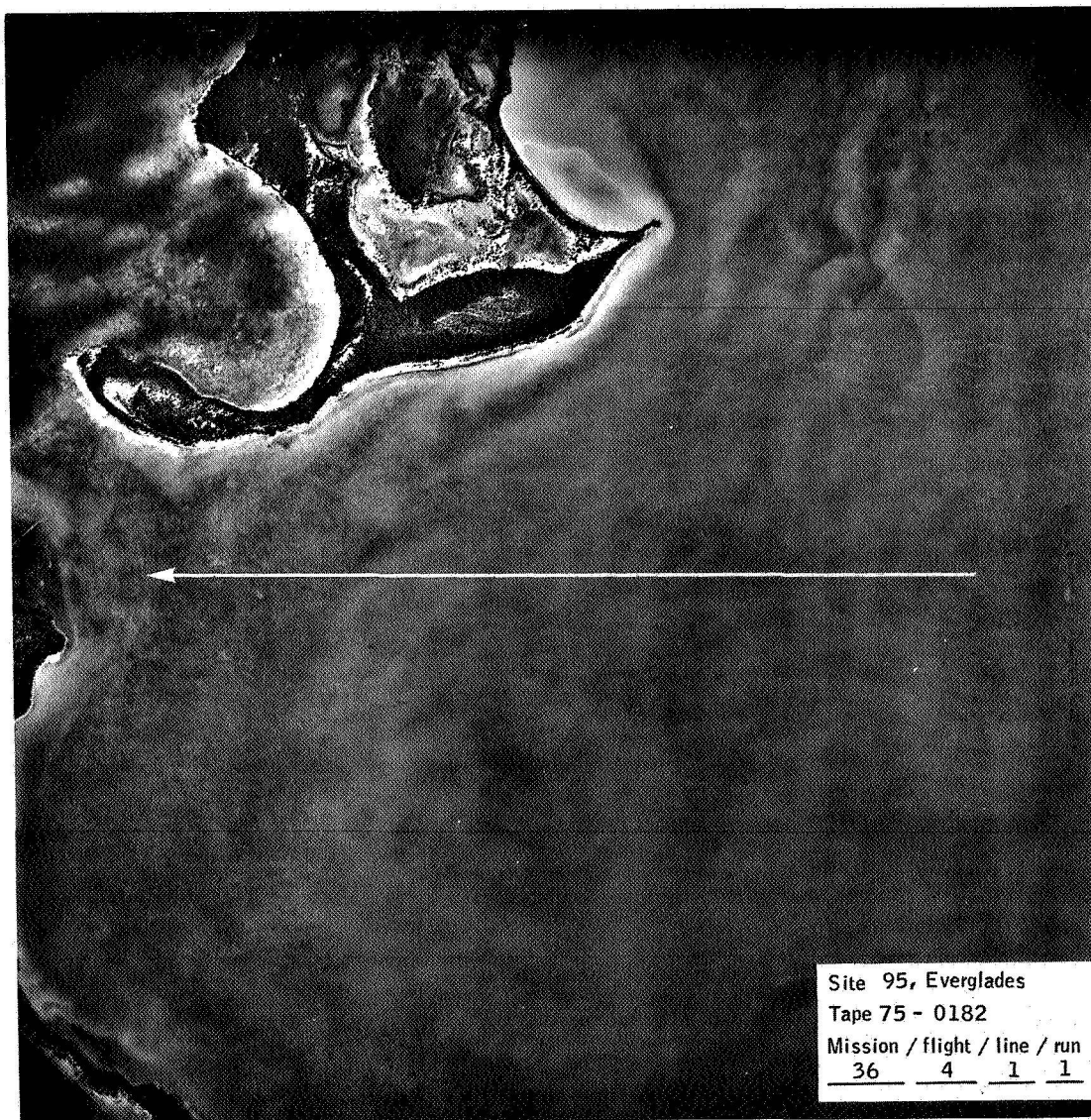
These data samples were taken near the southern end of line 1 over Florida Bay, north of Eagle Key. In the angular region of 0° to 25° , the $\sigma_0(\theta)$ curve reflects a sea condition approaching Beaufort 1. The increasing signal level beyond this point is a function of the return from the landmass (shown at the top of the accompanying photograph).



Site 95, Everglades	σ_0 sample time		
Tape 75 - 0182	Hours / minutes / seconds		
Mission / flight / line / run	<u>08</u>	<u>48</u>	<u>00</u>
<u>36</u> <u>4</u> <u>1</u> <u>1</u>	Through	<u>08</u>	<u>48</u> <u>05</u>

(a) The $\sigma_0(\theta)$ curve.

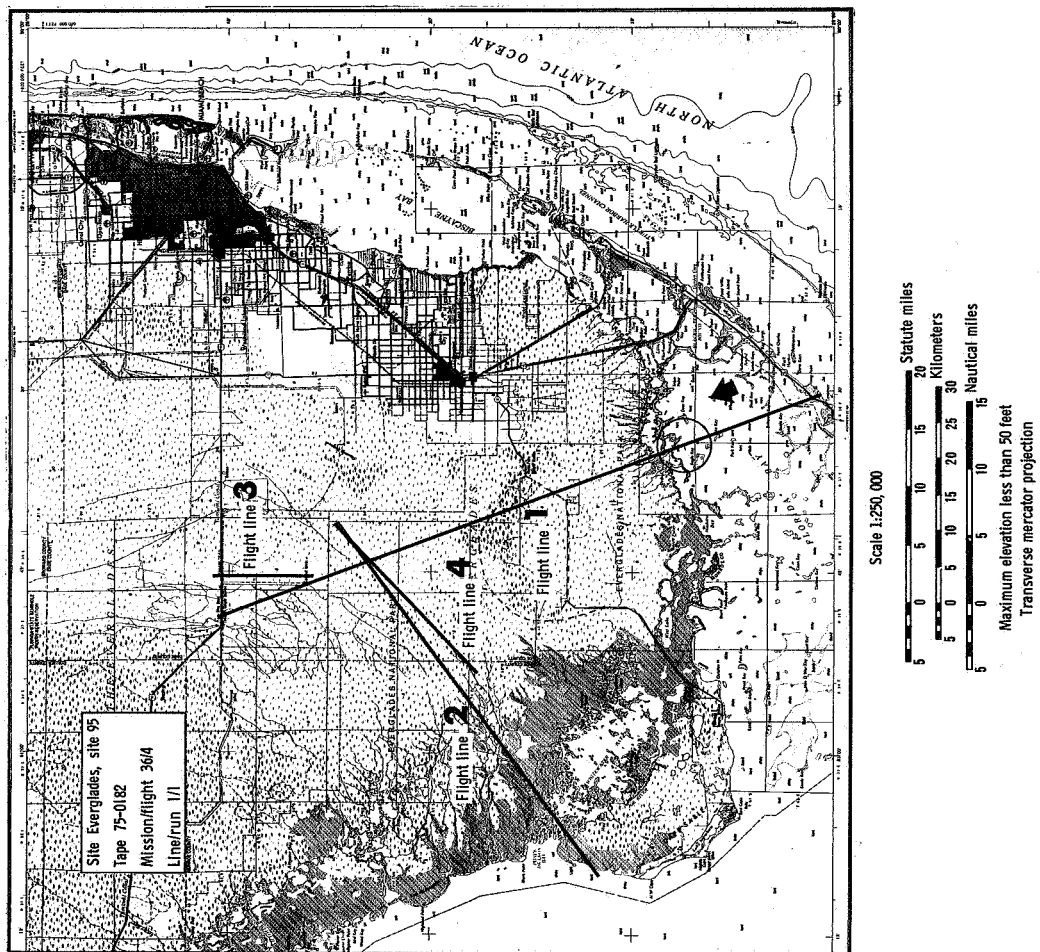
Figure B-17.- Set 17 data samples.



Site 95, Everglades
Tape 75 - 0182
Mission / flight / line / run
36 4 1 1

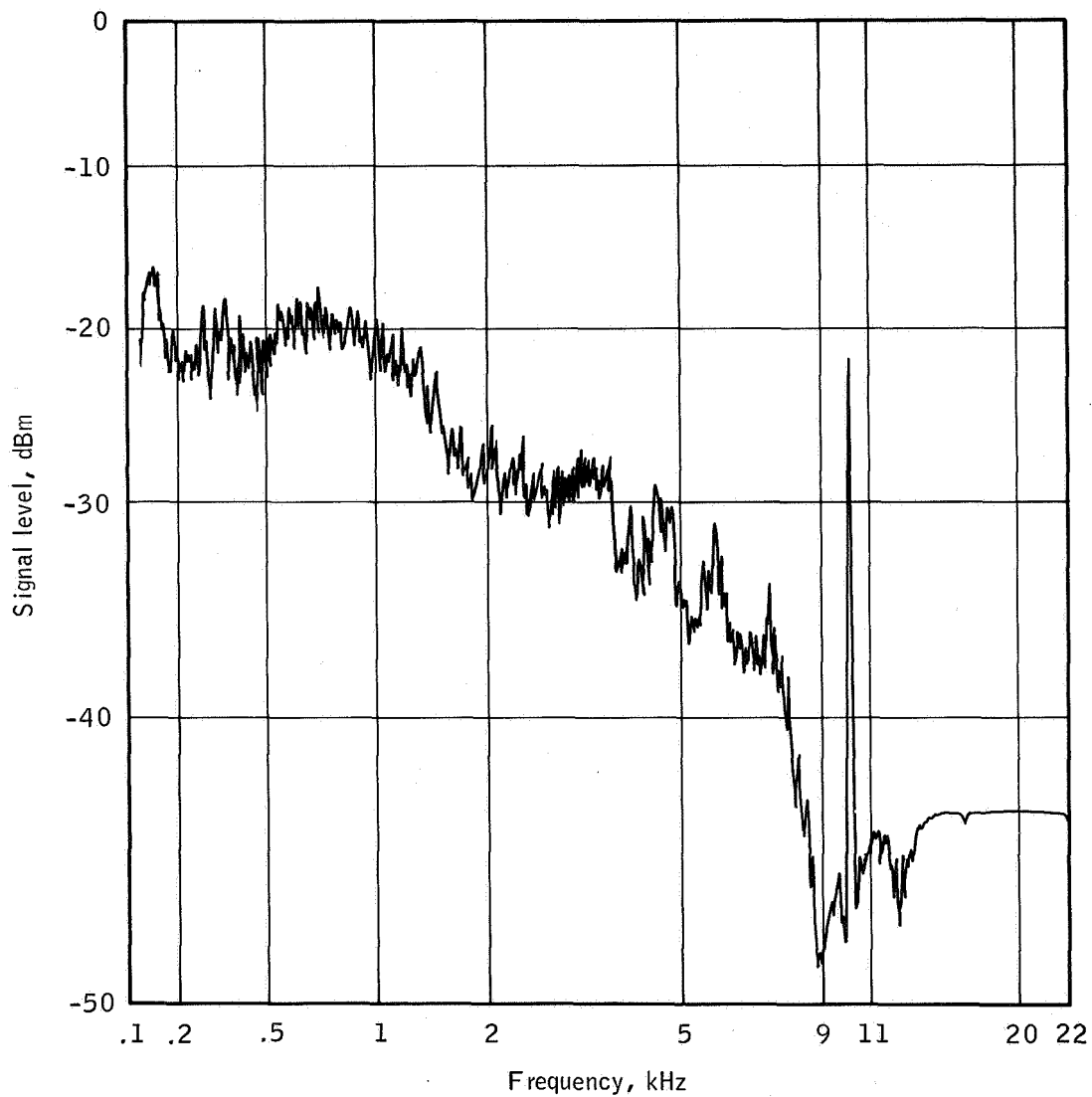
(b) Flight line.

Figure B-17.- Continued.



(c) Flight map.

Figure B-17.- Continued.



Site 95, Everglades

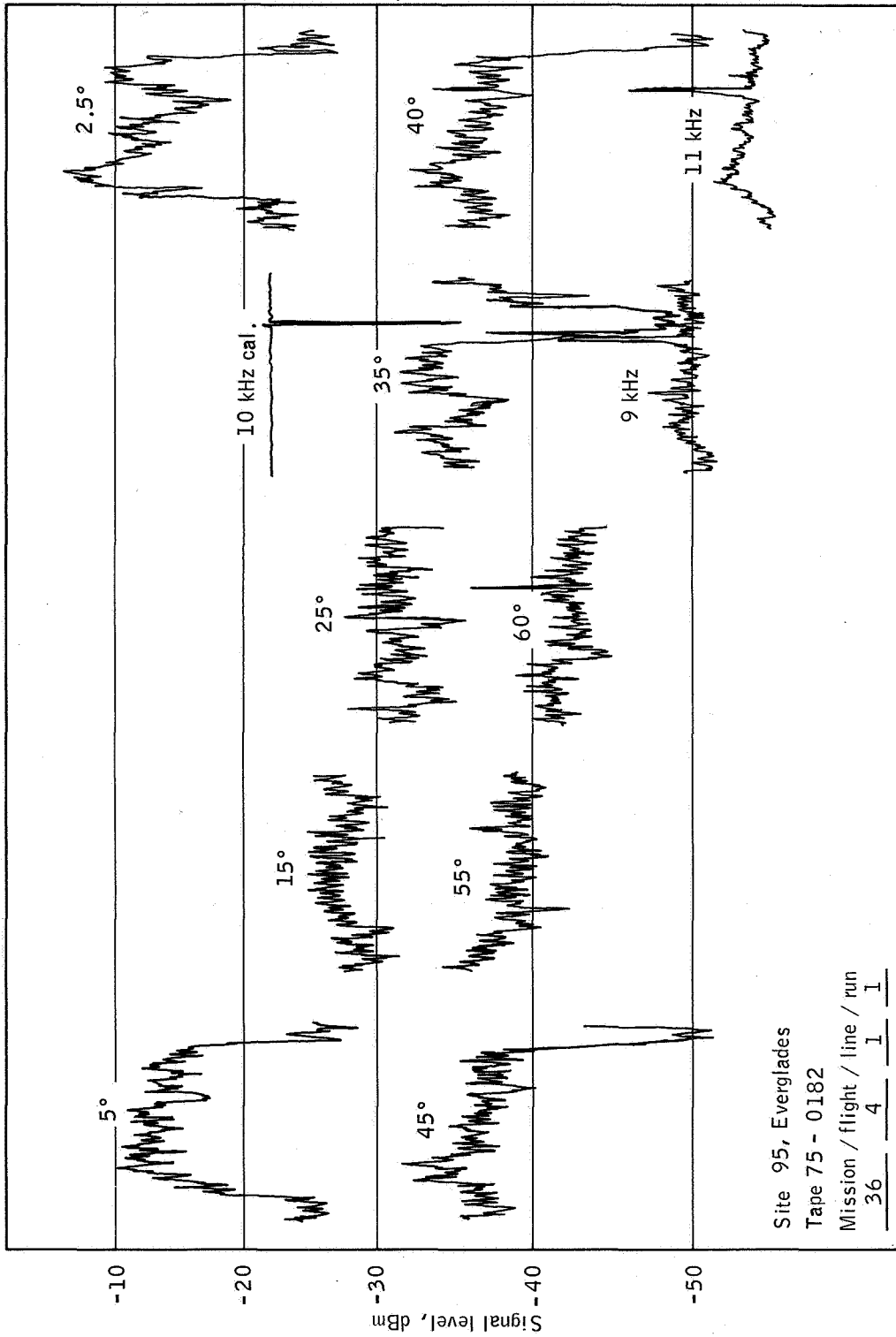
Tape 75 - 0182

Mission / flight / line / run

36 4 1 1

(d) The PSD curve.

Figure B-17.- Continued.



(e) Time history.

Figure B-17.- Concluded.

SET 18 — MISSION DATA

Mission/flight/line/run

36 4 4 2

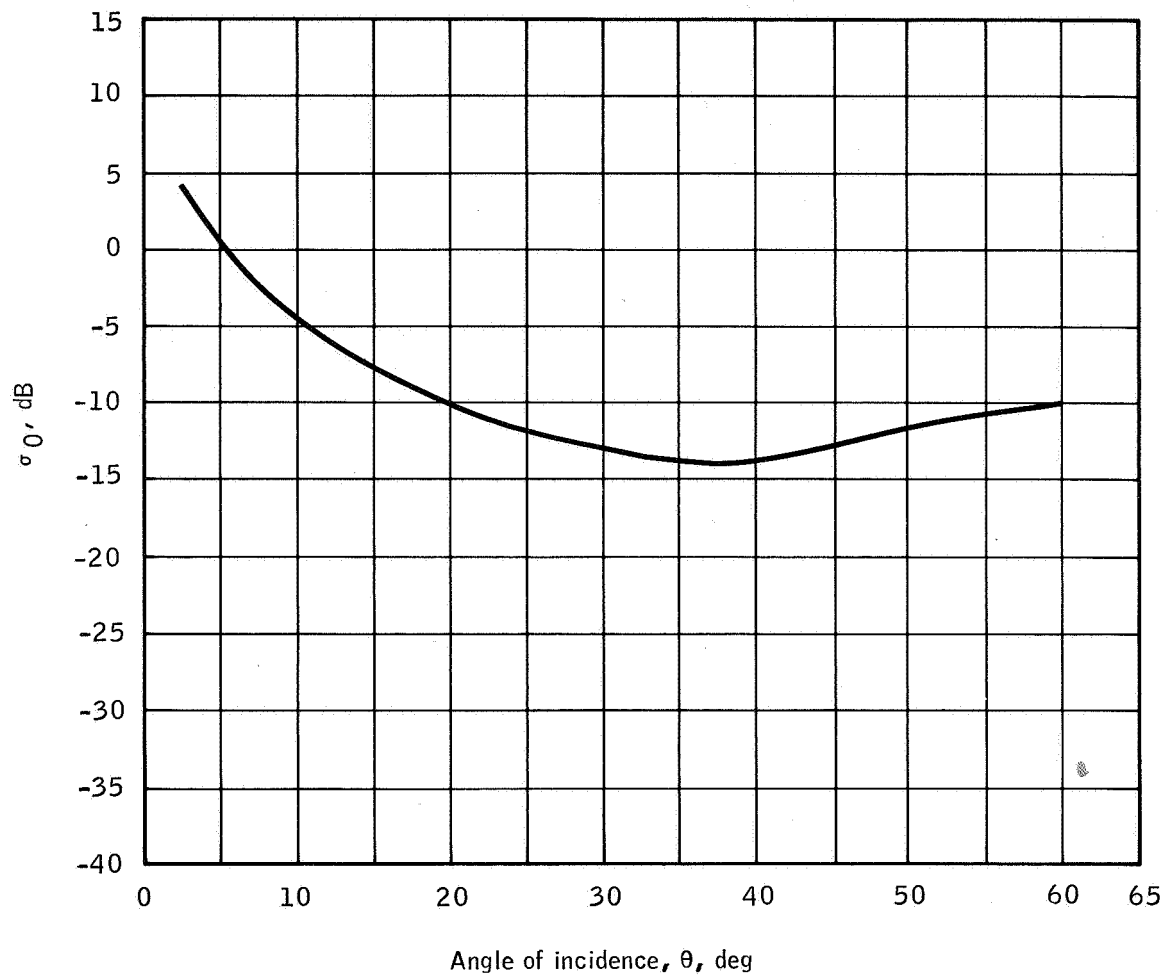
Site 95, Everglades, Florida

Altitude: 7000 feet

Time: 0911 e.s.t.

Infrared color film

These data samples were taken over the southwestern portion of line 4. The $\sigma_0(\theta)$ curve is almost identical to the one given for the land-sea interface near Eagle Key, is in the region of 10° to 40° , and is 3 dB lower than the data presented for flight 2, line 3, of mission 36. This may be a function of the increased percentage of water in this region.



Site 95, Everglades

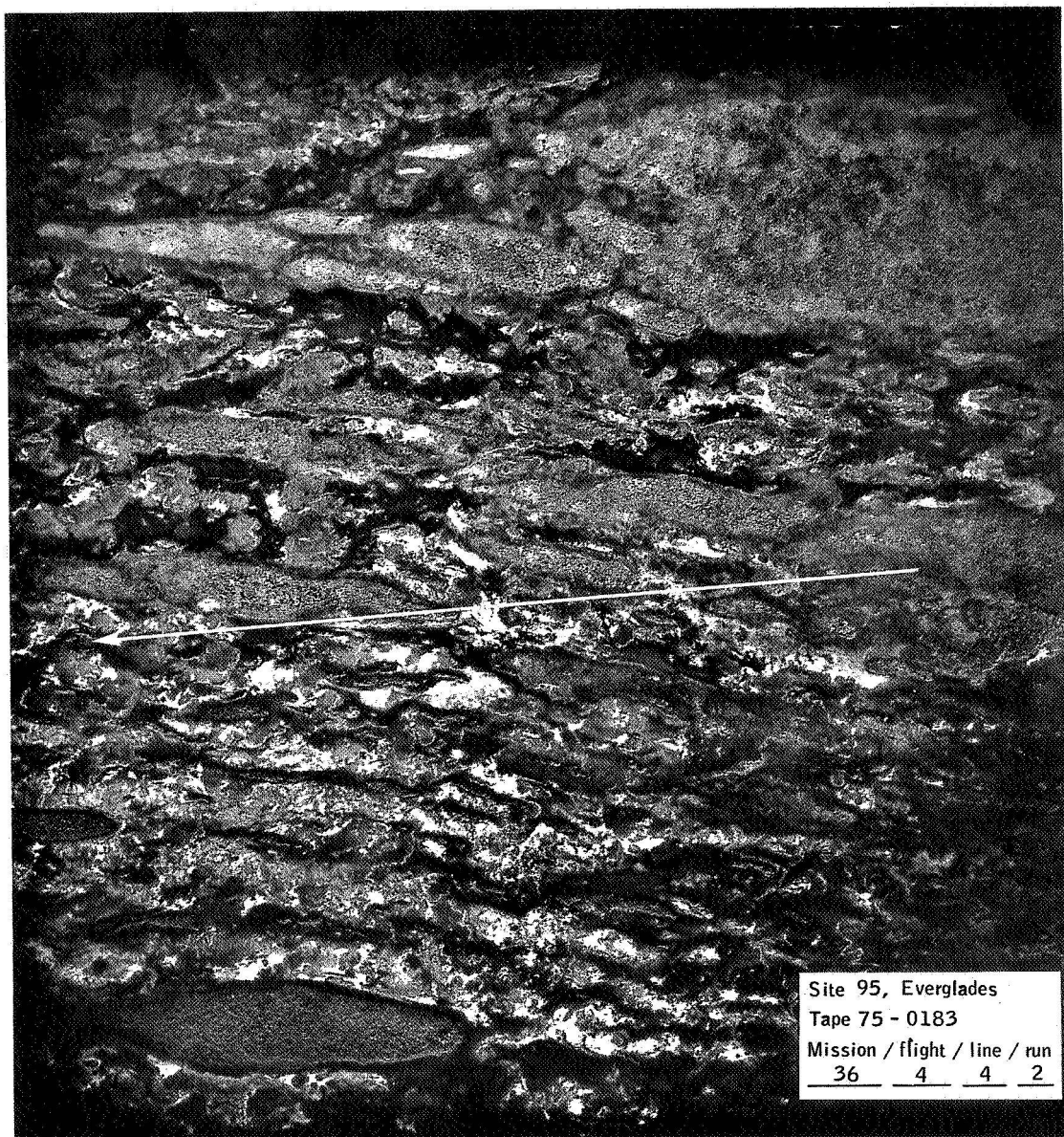
Tape 75 - 0183

Mission / flight / line / run
36 4 4 2

σ_0 sample time
 Hours / minutes / seconds
 09 11 30
 Through 09 11 40

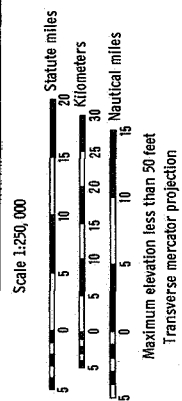
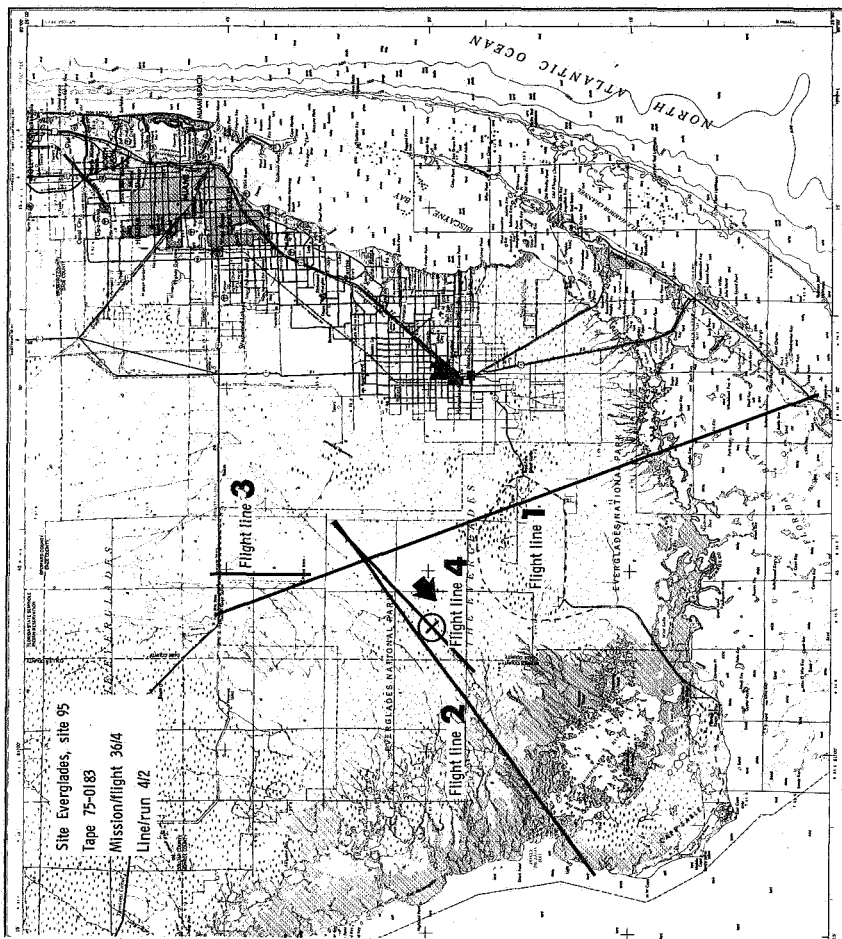
(a) The $\sigma_0(\theta)$ curve.

Figure B-18.- Set 18 data samples.



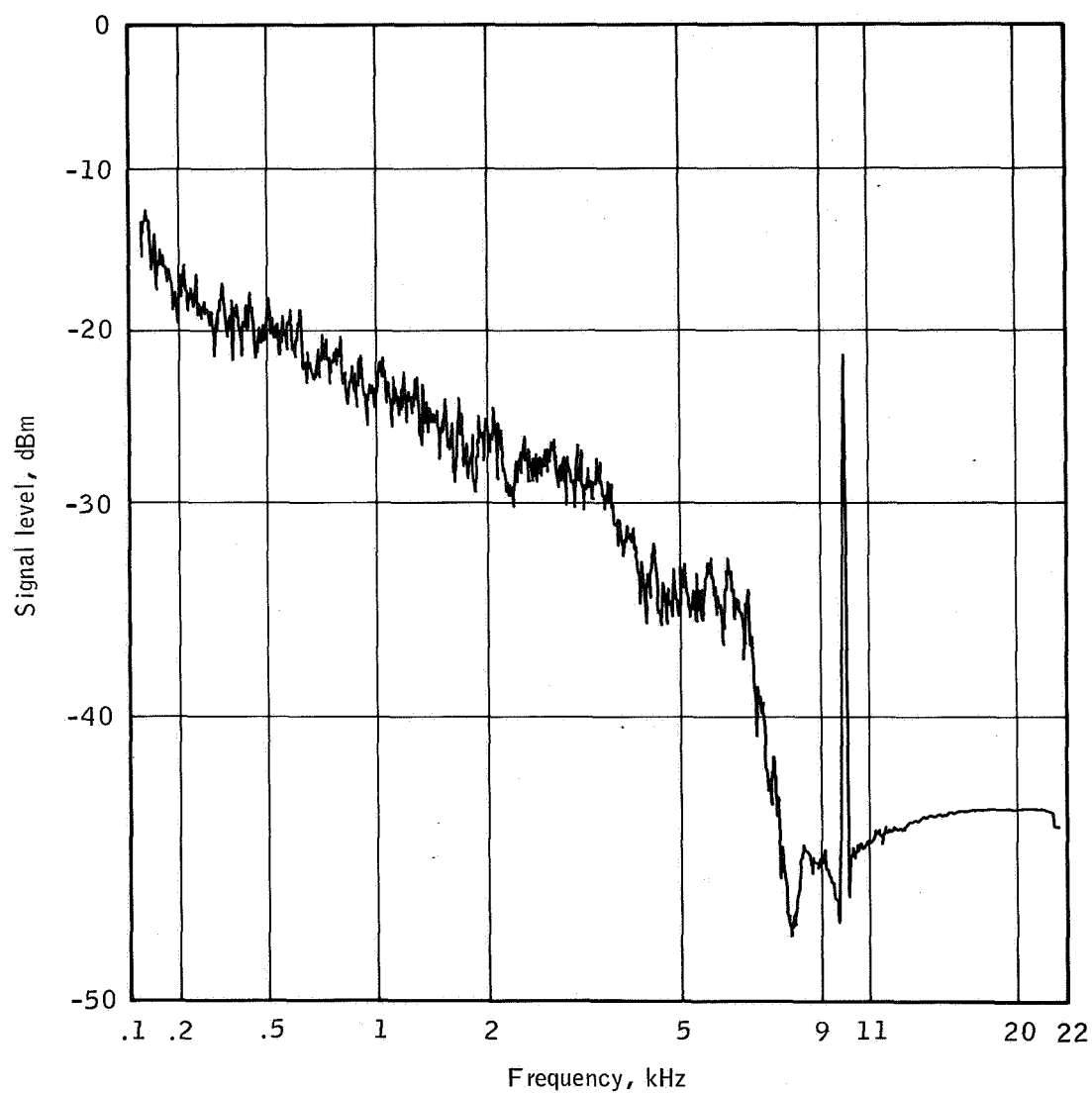
(b) Flight line.

Figure B-18.- Continued.



(c) Flight map.

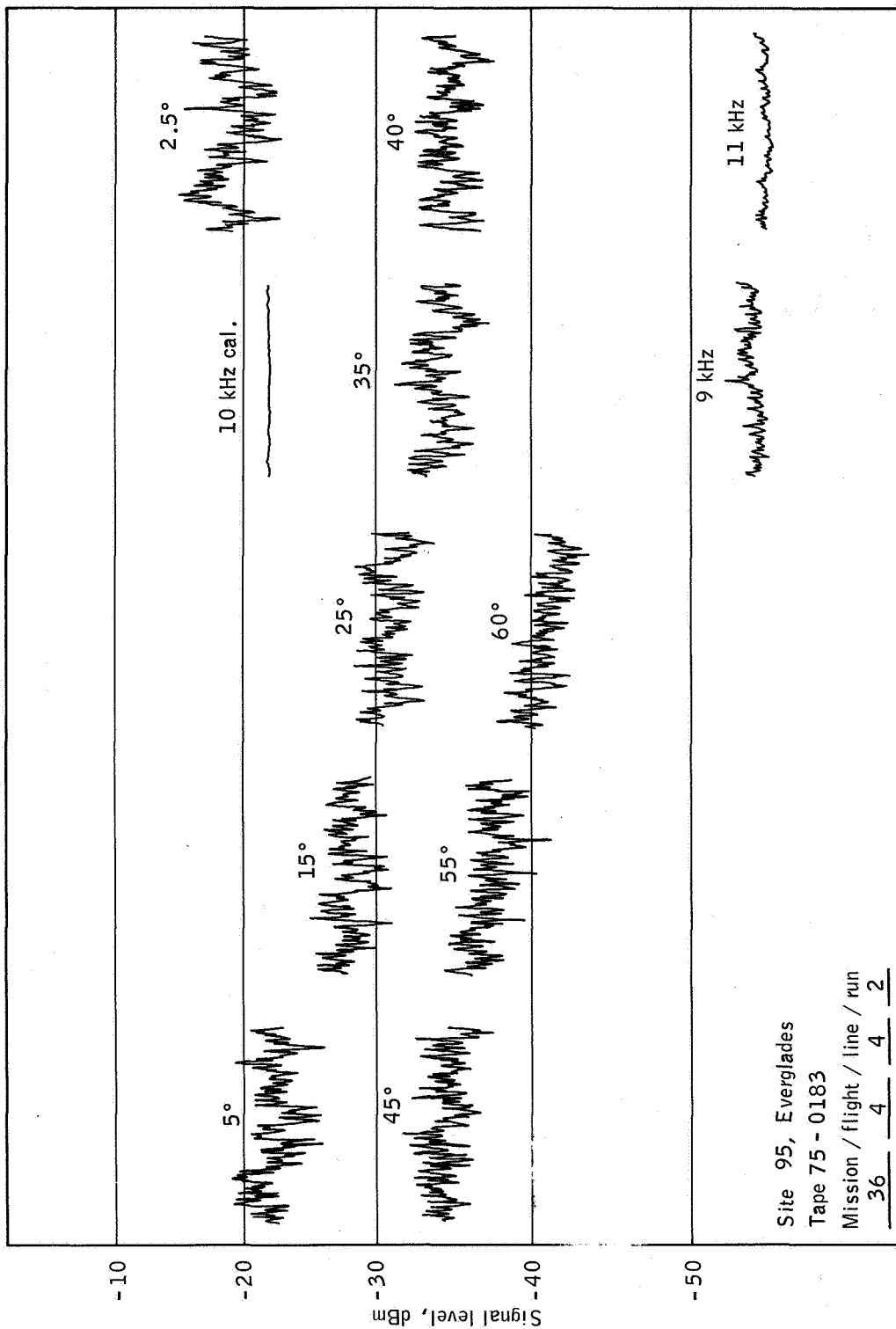
Figure B-18.- Continued.



Site 95, Everglades
Tape 75 - 0183
Mission / flight / line / run
36 4 4 2

(d) The PSD curve.

Figure B-18.- Continued.



(e) Time history.

Figure B-18.- Concluded.

REFERENCES

1. Toy, H. D.; Craib, K. B.; and Hughey, J. P.: Introduction to NASA 926 and NASA 927 Remote Sensor Aircraft as Applied to the Earth Resources Program. NR-04-00-999-0001, Mar. 1966.
2. Craib, Kenneth B.: Remote Sensing: A Survey Report. MSC-CA-R-67-2, Aug. 1967.
3. Senior, T. B. A.: A Survey of Analytical Techniques for Cross-Section Estimation. IRE Proceedings, vol. 53, no. 8, Aug. 1965, pp. 822-833.
4. Moore, R. K.: Radar Scatterometry — An Active Remote Sensing Tool. Proceedings of the Fourth Symposium on Remote Sensing of Environment, Apr. 1966; Willow Run Laboratories, Univ. of Michigan, CRES Report No. 61-11, June 1966, pp. 339-373.
5. Taylor, R. C.: Terrain Return Measurements at X, K_u , and K_a Band. IRE National Convention Record, vol. 7, part 1, Mar. 1959, pp. 19-26.
6. Rouse, J. W., Jr.; Waite, W. P.; and Walters, R. L.: Use of Orbital Radars for Geoscience Investigations. CRES Report No. 61-8, Eng. Sci., Jan. 1966.
7. Hayre, H. S.: Roughness and Radar Return. IRE Proceedings, vol. 50, no. 2, 1962, pp. 223-224.
8. Fung, A. K.: Theory of Radar Scatter from Rough Surfaces, Bistatic and Monostatic, with Application to Lunar Radar Return. J. of Geophys. Res., vol. 69, 1964, pp. 1063-1074.
9. Kuhl, F.; and Covelli, R.: Object Identification by Multiple Observations of the Scattering Matrix. IEEE Proceedings, Aug. 1965, pp. 1110-1115.
10. Moore, R. K.: Satellite Radar and Oceanography, An Introduction. Oceanography From Space, Woods Hole Oceanographic Institution, Ref. No. 65-10, 1965, pp. 355-376.
11. Dalke, G. W.: Identification of Remote Objects by Means of Scatterometry Data and Application to Pisgah Crater. CRES Report No. 61-17, Feb. 1967.

12. Cosgriff, R. L.; Peake, W. H.; and Taylor, R. C.: Electromagnetic Reflection Properties of Natural Surfaces With Application to Design of Radar and Other Sensors. Report No. 694-1, Ohio State University Research Foundation, Feb. 1959.
13. Katz, I.: Radar Reflectivity of the Earth's Surface. Appl. Phys. Lab. Tech. Digest, Feb. 1963, pp. 10-17.
14. Newbry, L. E.: Terrain Radar Reflectance Study. Photogrammetric Engineering, vol. 26, no. 4, 1960, pp. 630-637.
15. Staff of Ryan Aeronautical Company: Reflectivity Measurement Program. Report No. 29069-1, Mar. 1964.
16. Pierson, W. J., Jr.; Scheps, Benard B.; and Simonett, David S.: Some Applications of Radar Return Data to the Study of Terrestrial and Oceanic Phenomena. Proceedings of the Third Goddard Memorial Symposium on Scientific Experiments for Manned Orbital Flight, CRES Technical Report No. 61-8, Mar. 1965, pp. 87-137.
17. Floyd, W. L.; and Lund, T. J.: Scatterometer Program. Supplement to IEEE Transactions on Aerospace and Electronic Systems, no. 2, part 6, Nov. 1966, pp. 323-328.
18. Floyd, W. L.: Scatterometer Data Analysis Program Final Report. Report No. 57667-2, Sept. 21, 1967.
19. Beckmann, Peter: Scattering by Composite Rough Surfaces. IEEE Proceedings, Aug. 1965, pp. 1012-1015.
20. Fung, A. K.; and Moore, R. K.: Effects of Structure Size on Moon and Earth Radar Returns at Various Angles. J. of Geophys. Res., vol. 69, Mar. 1964, pp. 1075-1081.
21. Marks, W.: The Application of Airborne Radar Backscatter to Measurement of the State of the Sea. Oceanography From Space, Woods Hole Oceanographic Institution Ref. No. 65-10, 1965, pp. 377-391.
22. Evans, J. V.; and Pettengill, G. H.: The Scattering Behavior of the Moon at Wavelengths of 3.6, 68, and 784 Centimeters. J. of Geophys. Res., vol. 68, Jan. 1963, pp. 423-447.
23. Godbey, Thomas W.: Oceanographic Satellite Radar Altimeter and Wind Sea Sensor. Oceanography From Space, Woods Hole Oceanographic Institution, Ref. No. 65-10, 1965, pp. 21-26.

24. Schooley, Allen H.: Upwind-Downwind Ratio of Radar Return Calculated from Facet Size Statistics of a Wind-Disturbed Water Surface. IRE Proceedings, Apr. 1962, pp. 456-461.
25. Katz, I.: Radar Backscattering From the Sea. Oceanography From Space, Woods Hole Oceanographic Institution, Ref. No. 65-10, 1965, pp. 367-376.

BIBLIOGRAPHY

Craib, K. B.: Radar Scatterometer Data Validation: Phase One.
MSC-CA-R-67-3, Nov. 1967.